Theory and Experiment of Chalcogenide Materials

A dissertation presented to

the faculty of

the College of Arts and Sciences of Ohio University

In partial fulfillment

of the requirements for the degree

Doctor of Philosophy

Binay K. Prasai

August 2013

This dissertation titled

Theory and Experiment of Chalcogenide Materials

by

BINAY K. PRASAI

has been approved for

the Department of Physics and Astronomy

and the College of Arts and Sciences by

David A. Drabold

Distinguished Professor of Phyiscs

Gang Chen

Associate Professor of Physics

Robert Frank

Dean, College of Arts and Sciences

ABSTRACT

PRASAI, BINAY K., Ph.D., August 2013, Physics

Theory and Experiment of Chalcogenide Materials (156 pp.)

Directors of Dissertation: David A. Drabold and Gang Chen

In this dissertation, we present the experimental and theoretical investigation of extensive properties of chalcogenide materials and their potential application in solid electrolytes and phase change memory materials. Extended X-ray absorption fine structure (EXAFS) spectroscopy was employed to study the structural properties and the results were validated from the computer simulated models through *ab-initio* molecular dynamic (AIMD) simulations. EXAFS analysis on Ge-Sb-Te (GST) alloys, synthesized using electrodeposition and radio frequency sputtering methods confirmed the structural similarities in Ge-Te and Sb-Te bond pairs suggesting the possibility of utilizing the electrodeposition method to grow GST alloys in nanoporous materials and thus enabling miniaturizing the phase change memory devices. The analyses of structural, electronic and optical properties of computer generated amorphous and crystalline TiO_2 confirmed the structural similarities of amorphous TiO_2 with the anatase phase of crystalline TiO_2 and hence recommending the possibilities of replacing the crystalline TiO_2 by less processed thus cheaper form of amorphous TiO_2. Moreover, the AIMD simulations of the ionic conductivity of transitions metals like Ag and Cu in Ge-Se glasses confirmed the superiority of Ag over Cu in terms of conductivity. Ag was found to be easily hopping around while Cu was often trapped. In addition, an experimental and computational investigation on Ag-doped Ge-Sb-Te alloys predicted an enhanced crystallization of Ge-Sb-Te alloys. The enhanced crystallization was related to the reduction of fraction of tetrahedral Ge relative to octahedral Ge as also reflected as the increased Ge-Te bond lengths on adding Ag. Finally, further investigation of dopant-induced modification of GST alloys with transition metals (Cu, Ag and Au) demonstrated the superiority of Ag

over Cu and Au regarding crystalline speed while at ~ 2% dopant level no significant structural modification was observed.

To my BABU

ACKNOWLEDGMENTS

My dissertation will not be complete without thanking and appreciating the people and the organizations for their support throughout my career. I would like to thank my advisors Distinguished Prof. David A. Drabold and Associate Prof. Gang Chen for their four years of guidance and support. I should express my appreciation to my advisors for giving me the freedom of following my own research path and giving me valuable suggestions whenever I need them. I would also like to acknowledge Prof. Martin E. Kordesch for providing the useful samples and giving me helpful suggestions. I also wish to thank Dr. Qing Ma, Chandrashri and Ramana for their assistance during the experiments.

I would like to thank Ohio University for giving an opportunity for pursuing my education and for giving me financial support and a very supportive environment to proceed my research. My token of appreciation especially goes to Department of physics and Astronomy where I obtained the prerequisite education so that I could proceed to my research. Everyone from faculty, staff, and peers was always encouraging to me.

I further extend my acknowledgments to NSF for providing a financial support. I also wish to thank Ohio supercomputer center (OSC) for providing me a computing time and Argonne National Laboratory for providing an access to conduct my experiments.

Finally, I would also like to thank my parents for educating me to become a responsible and an honest person. Support from my family in pursuit of science was always encouraging to me.

TABLE OF CONTENTS

LIST OF TABLES

LIST OF FIGURES

1 INTRODUCTION

1.1 Background

The scientific study of amorphous materials is becoming increasingly important since these materials have vast applications in modern technology. In principle, almost all material compounds can be prepared as amorphous solids depending on how fast they are cooled from molten states. The loss of the long-range translational periodicity in the amorphous materials makes the task of understanding the structural and physical properties of these materials challenging. However, the absence of long-range order in these materials does not mean entire randomness in the materials since there exists a high degree of local order on a shorter length-scale (0-5Å). Besides this short range order (SRO) there may exists an intermediate range order (IRO) or medium range order (MRO) at the length scale of (5-20Å) depending on material systems.

1.2 Chalcogenide materials

Also known as the oxygen family, chemical elements in group 16 of the modern periodic table are called chalcogens. It consists of elements oxygen (O), sulfur (S), selenium (Se), tellurium (Te) and a radioactive element polonium (Po). These elements are two electrons short of a full outer shell with most common oxidation states of ±2, 4 and 6. Chalcogenide materials (materials containing one or more of the chalcogen elements, mainly, S, Se, or Te) are extensively studied for their potential applications in technological uses such as optical recording devices[1] and non volatile memory devices [2, 3].

1.3 Investigation of properties of chalcogenide materials

Structural information can be obtained by a number of experimental techniques like neutron diffraction and X-ray diffraction but, unlike crystals, they can provide this

information only in a statistical way. In other words, these techniques can only provide distributions of bond lengths, angles and an average coordination number. Considering the uncertainty in the experimental determination and its associated fundamental limitations (averaging over macroscopic numbers of atoms), computer simulation has become a very helpful aid to the experiment, in order to understand the structure of the amorphous materials more thoroughly. To get theoretically and experimentally credible models, two modeling techniques are used; one based on the preexisting experimental evidence (biased modeling) and the other not requiring a priori information (direct modeling). In this research, the experimental technique used is X-ray absorption spectroscopy (XAS) and the theoretical technique used is a direct modeling, in order to obtain the structural information. As soon as the credible models are available, the properties of these materials could readily be studied by using various techniques.

1.3.1 Structural Analysis

1.3.1.1 Extended X-ray Absorption fine structure (EXAFS) analysis

EXAFS spectroscopy has been widely used to probe local structures, particulary, in amorphous materials. EXAFS spectroscopy is based on the absorption of x-ray photons of sufficiently high energy that can eject a core electron from an absorbing atom. The absorption edge corresponds to an x-ray photon that has enough energy to free an electron in the atom[4]. The edge corresponding to innermost electron i.e. n=1 shell, is known as K-edge. Similarly the higher shells correspond to L-edge, M-edge and so on. When an x-ray photon with sufficiently large energy $h\nu$ is absorbed by a core electron, the electron will have a kinetic energy equal to the difference between the photon energy and the binding energy as given.

$$\frac{p^2}{2m} = h\nu - E_b \tag{1.1}$$

This outgoing photoelectron which can also be represented as an outgoing wave is scattered by the surrounding atoms and hence giving the final state as the superposition of the outgoing and the scattered waves. The modification of the absorption spectrum of photoelectron by the surrounding atoms at the center of the absorbing atom modifies the X-ray absorption and leads to EXAFS. The peaks in the EXAFS correspond to the backscattered wave being in phase with the outgoing wave whereas the valleys correspond to these being out of phase. Since atoms have different scattering strength, the variation of EXAFS depends on the type of atom doing the backscattering. Hence EXAFS contains information of the atomic surroundings of the center atom, and with a more quantitative description of EXAFS it is possible to obtain this information[4].

Analysis of the data starts with a reduction of measured raw absorption spectra into EXAFS spectra. This data reduction involves the normalization and conversion into k spectra from the raw absorption spectra using equations[4]:

$$k = \sqrt{\frac{2m_e(E - E_o)}{\hbar^2}} \tag{1.2}$$

$$\chi(k) = \frac{\mu - \mu_o}{\mu_o} \tag{1.3}$$

where, E_o is the threshold energy or the binding energy of the photoelectron, μ is the observed absorption coefficient and μ_o is the absorption that would be observed in the absence of EXAFS effects. It is based on the assumption that μ_0 is represented by the smooth part of μ and hence $\mu - \mu_o$ gives the required oscillatory part[5]. Here the division by μ_o is to normalize the EXAFS oscillations. EXAFS represents the average structure around absorbing atoms. Since μ_o cannot be directly measured, it has to be approximated by fitting μ with some polynomial splines or using a least square procedure. In this work we used a package called ATHENA[6] for this purpose. ATHENA approximates the background via linear approximation (to the pre-edge) and via spline function (to the atomic background). The next step is to analyze the $\chi(k)$ data to obtain structural

parameters such as bond length(R), coordination number (N) and mean squared relative displacement (σ^2) which are obtained by optimizing the parameters in an equation:

$$\chi(k) = \sum_s \frac{NA(k)S_0^2}{kR^2} e^{-\frac{2R}{\lambda(k)}} e^{-2k^2\sigma^2} sin(2kR + \phi(k)) \qquad (1.4)$$

The parameters A(k), S_0^2, $\phi(k)$ and $\lambda(k)$ that define scattering are determined using model compounds of known structure. Here, $\phi(k)$ is the total phase shift experienced by the photoelectron and includes the central and the backscattering atom phase shifts. Equation 3.14 is however based on the assumption that the X-ray excited photoelectron undergoes a single scattering before returning to the absorbing atom. In fact, the photoelectron can undergo multiple scattering (scattered by more than one atom). This multiple scattering is more effective at low k while less effective at high k and is important while dealing with XANES. Analysis of EXAFS data in this work is based on single scattering of the X-ray excited photoelectron. The scattering paths and phase shift information are calculated by using FEFF[7] using a computer generated model, and the structural parameters in the expression of $\chi(k)$ are optimized by using ARTEMIS[6].

1.3.1.2   Correlation functions: computational approach

Pair correlation functions (PCF) The atomic structure of an amorphous material is studied through a set of pair correlation functions. A pair correlation function is a position distribution function based on the probability of finding atoms at some distance $\vec{r}$ from a central atom. A general expression for the pair distribution function can be written as[8]:

$$g(\vec{r}) = \frac{1}{\rho^2 V} N(N-1)\langle\delta(\vec{r} - \vec{r_{ij}})\rangle \qquad (1.5)$$

Here, ρ and V are the number density and volume respectively of the model, N the number of neighboring atoms of the central atom and r_{ij} is the distance of any atom from the central atom. The term $\langle..\rangle$ can be expressed as

$$\langle\delta(\vec{r} - \vec{r_{ij}})\rangle = \frac{1}{N(N-1)} \sum_{i,i\neq j} \delta(\vec{r} - \vec{r_{ij}}) \qquad (1.6)$$

and is the average over all possible configurations. The radial pair correlation function can be obtained as

$$g(r) = \int \frac{d\Omega}{4\pi} g(\vec{r}) \tag{1.7}$$

or,

$$g(r) = \frac{1}{\rho^2 V} \sum_{i,i \neq j} \int \int \frac{sin\theta}{4\pi} d\theta d\phi \frac{1}{r^2 sin\theta} \delta(r - r_{ij}) \delta(\theta - \theta_{ij}) \delta(\phi - \phi_{ij}) \tag{1.8}$$

or,

$$g(r) = \frac{1}{4\pi\rho^2 V r^2} \sum_{i,i \neq j} \delta(r - r_{ij}) \tag{1.9}$$

The pair correlation functions gives the local structural information in amorphous materials. The peaks in these distribution functions describe the average distance of the neighboring atoms from a central atom. Since amorphous materials do not possess long range order $g(r) \rightarrow 1$ as $r \rightarrow \infty$. For a crystalline structures, $g(r)$ is a sum of delta functions, with each term representing a coordination shell. The pair function which can provide results of diffraction experiments via fourier transformation, yield crucial information about the short-range order and the nature of chemical bonding.

For systems with more than one species, the structural correlations are usually investigated through partial pair correlation functions $g_{\alpha\beta}(r)$, which are expressed as

$$\langle n_{\alpha\beta}(r) \rangle \Delta r = 4\pi r^2 \Delta r \rho c_\alpha g_{\alpha\beta}(r) \tag{1.10}$$

where $n_{\alpha\beta}(r)\Delta r$ is number of particles of species β in a shell between r and r+Δr around a central atom α, $c_\alpha = N_\alpha/N$ is the concentration of species α. The total pair correlation function is then defined as the sum of all partial contributions as

$$g(r) = \sum_{\alpha\beta} c_\alpha c_\beta g_{\alpha\beta}(r) \tag{1.11}$$

Although the set of PCFs provides some basic information, we require multipoint functions (more than two points) to thoroughly characterize a structural models. However, these multipoint functions are not readily measured by the current experimental resources.

This situation is somehow improved with theoretical models. In addition to local bonding provided by pair correlation functions, coordination statistics provide insights to a local topology for an atom. Beside this, other distribution functions like angle distribution and ring statistics would also be useful tools particular for theoretical models in order to study the local environment of each atom.

1.3.2 Electronic Structure

The electronic structure is usually described by analyzing the electronic density of states (EDOS), projected density of states (PDOS), and inverse participation ratio (IPR) of each individual site. EDOS is defined as:

$$g(E) = \sum_{i=1}^{N_{states}} \delta(E - E_i) \tag{1.12}$$

The EDOS provides the information about the electronic gap which plays an important role for electronic properties of the materials. PDOS on the other hand puts light on the defects or irregularities in the topology. A common expression for PDOS is:

$$g_n(E) = \sum_{i=1} \delta(E - E_i)|\langle \phi_n|\Psi_i \rangle|^2 \tag{1.13}$$

where $g_n(E)$ is site projected DOS for the site n, ϕ_n is the local orbital and Ψ_i is the ith eigenvector with eigenvalue E_i.

We use Inverse Participation Ratio(IPR) analysis to investigate the localization of the tail states near the gap region. The degree of localization for a given electronic eigen state is measured by the IPR[9]; I=1 for highly localized states and N^{-1} for extended states, where N is the number of atoms, and IPR for a system with N atoms is defined as

$$I(E) = N \sum_i q(i, E)^2 \tag{1.14}$$

where $q(i,E)$ is the charge localized on an atom site i for a state with energy E.

1.3.3   Ion Dynamics

The dynamics of ions in the glass host is studied by computing the mean-squared displacement (MSD) for each atomic constituent as:

$$\langle r^2(t) \rangle_a = \frac{1}{N_a} \sum_{i=1}^{N_a} \langle |\vec{r_i}(t) - \vec{r_i}(0)|^2 \rangle \tag{1.15}$$

where the quantity in $\langle \rangle$ is the calculated statistical average over the particular atomic species α. Each instantaneous configuration is used to obtain the MSD and the average MSD for each species of interest is plotted as a function of time. Based on the plots diffusion coefficients are calculated using Einstein relation[10]. The Einstein relation for self-diffusion is given by:

$$\langle |\vec{r_i}(t) - \vec{r_i}(0)|^2 \rangle = 6Dt + C \tag{1.16}$$

where C is a constant and D is the self-diffusion coefficient. The ionic conductivity can be calculated from the equation

$$\sigma = \frac{ne^2 D}{k_B T} \tag{1.17}$$

where n is the number density of ions.

1.4   Applications of Chalcogenides

1.4.1   Electrolyte materials

There has been particular interest in Ge-Se glasses because of their excellent glass formation capability ($Ge_x Se_{1-x}$ binary system is an excellent glass former for x $\leq$0.43 [11]), easy synthesis, high transformation temperature and chemical stablity. Depending on the Ge content, the basic units of GeSe glasses consist of Ge-Se tetrahedra and Se chains combined in various ways[12]. Furthermore, this is one of systems in which formation of an intermediate phase has been demonstrated[13]. When doped with metals like Ag, Ge-Se glasses become solid electrolytes offering high ionic conductivities. Such

electrolytes are getting attention in ``conductive bridge ´´(flash) memory devices[3]. Since the knowledge of the structure of glasses essential to understand the properties of glasses, efforts have been made to understand structural properties of these glasses. Both the experimental [14–16] and the theoretical[17, 18] methods have been used to study the structure of Ge-Se-Ag glasses.

1.4.2 Phase change memory materials

Because of a capability of ultrafast and reversible phase transition between amorphous and crystalline states, with significantly different electrical conductivites and sufficient thermal stability, phase change memory materials (PCMMs) have potential application to non-volatile data storage[19, 20] . Already appearing in commercial cell phones, chalcogenide PCMMs offer a practical alternative to conventional Flash memory. Phase change random access memory (PCRAM) operates on principle of reversible phase transition between amorphous and crystalline phases of phase change materials (PCM) by joule or laser heating. Significantly high resistivity (low reflectivity) in the amorphous state and low resistivity (high reflectivity) in the crystalline state represent ``0´´and ``1´´states respectively, in the memory devices. Fig. 1.1 illustrates a basic principle of data storage in PCM [21]. PCM in crystalline state with high conductivity (low resistivity) or high optical reflectivity is heated with either laser or electric pulses, locally melting the material. The material is solidified fast enough that the crystallization is prevented and quenched to a amorphous phase. This is the process of writing. To erase the data the material in amorphous phase is heated above the crystallization temperature slowly until the material is crystallized.

Ovshinsky's observation of electrical switching in an amorphous chalcogenide stimulated the interest and research in the possibility of switching between an amorphous and a crystalline phases, with contrast properties, using electrical pulses [2]. The
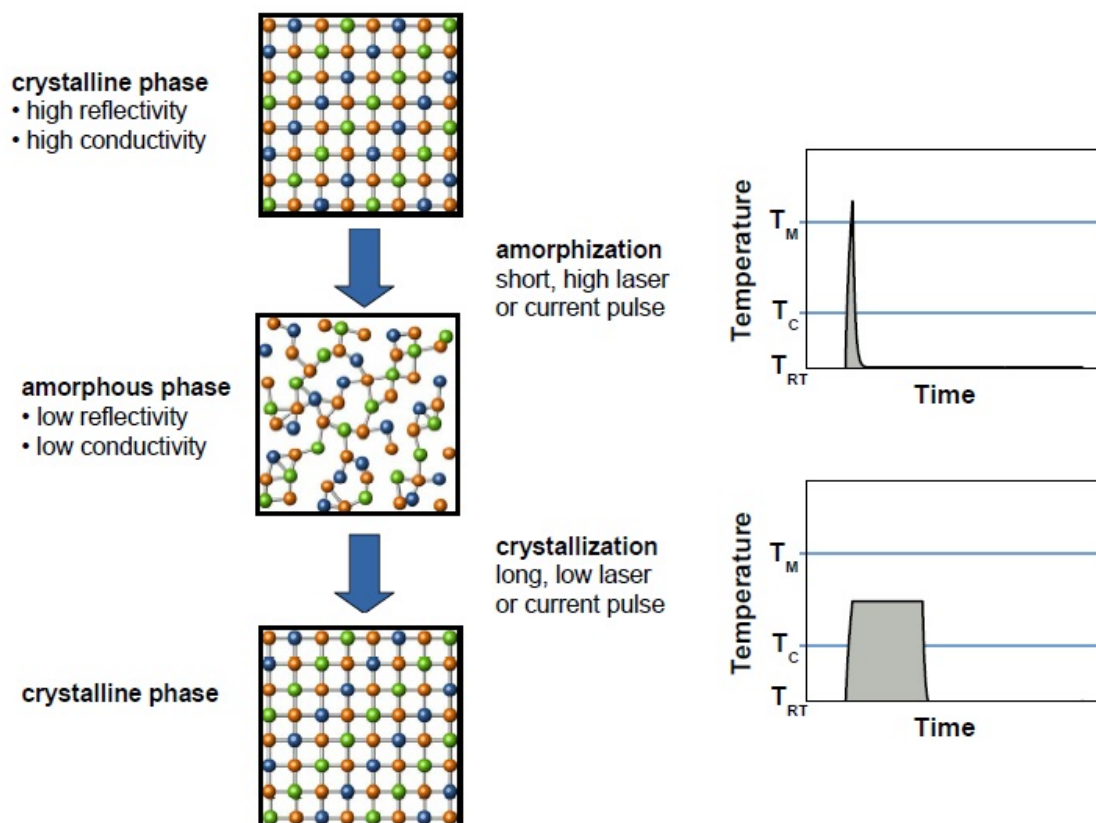
Figure 1.1: A process of write and erase of the phase change materials. A high but short laser or electric pulse is used to melt the crystalline phase. The melt is quickly quenched to form the amorphous phase (write). To erase the data the amorphous phase is annealed just above the crystallization temperature for relatively longer time with a low laser of electric pulse.

contrasting electrical and optical properties are prerequisites for PCM. but other demands should be satisfied in order for the material to be used in memory devices. The stability of amorphous phase is required to have good data retention. Furthermore the material should be stable over more than 10^9 phase transitions so that the device can be used for many read-write cycles. Beside these, the material should possess high crystallization speed to allow fast data processing. In 1987, Yamada *et al.* were able to discover a group of materials with these properties[20]. These materials lie along the tie line between GeTe

and Sb_2Te_3 as shown in Fig. 1.2. Apart from Ge-Sb-Te alloys, many other materials have been identified as PCM.
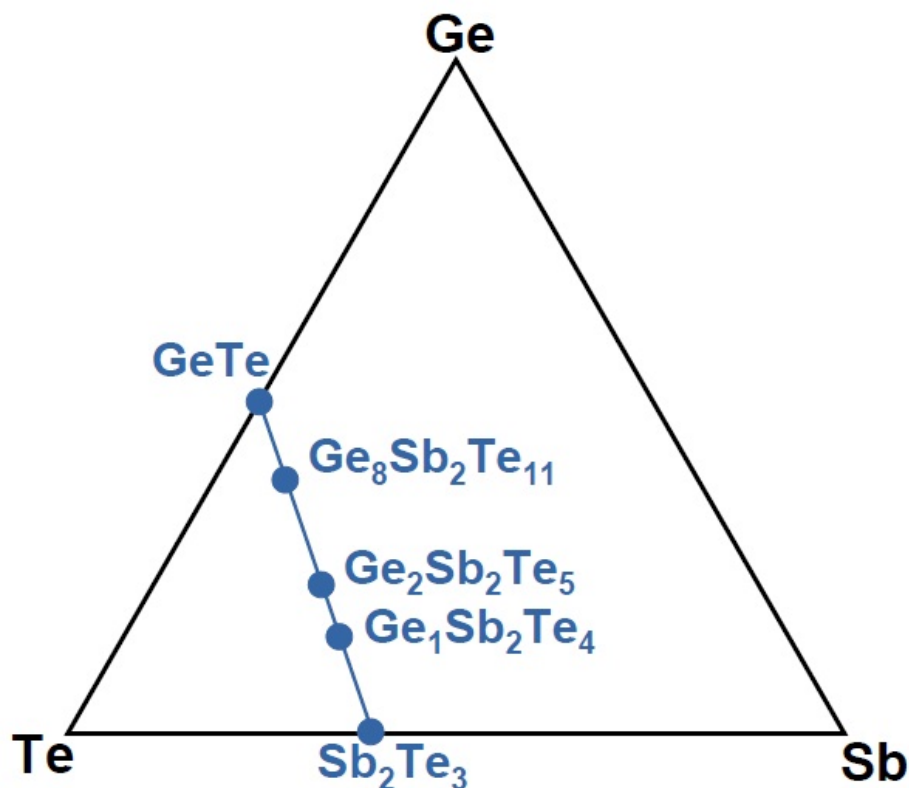
Figure 1.2: Ge-Sb-Te ternary phase diagram. Ge-Sb-Te alloys that lie on the tie line of GeTe and Sb_2Te_3 are shown in blue.

1.5 Organization of the dissertation

The dissertation is aimed to gain insights into the structures of the materials based on chalcogenides through both the experimental and computational methods whenever possible since the properties of any materials originate from the structures. In Chapter 2, we discuss briefly the computational methods followed by the experimental method in Chapter 3. We present the results and discussions of different projects from Chapter 6 to 9 followed by the conclusion in Chapter 10.

Based on the applications of chalcogenide materials, the dissertation can be divided into two parts. In Chapter 4 and 5, I will discuss the first principles calculations on TiO_2 and Ag/Cu-doped $GeSe_3$ glasses with potential uses in solid electrolytes. The discussions on these materials are published in Journal of Materials Science[22] and Physical Rev B. [17] respectively. On the other hand, Chapter 6 to 9 are dedicated to the study of phase change memory materials through both experiments and computations. Again Chapters 7 and 8 are mostly based on the published papers in App. Phys. Lett. [23] and Phy. Status Sol. B. [24] respectively. As a first author, my roles in these studies were to carry out all the computations described in the papers and to write the manuscripts.

2   DENSITY FUNCTIONAL THEORY : COMPUTATIONAL APPROACH

2.1   Background

Computational methods are becoming essential tools in the field of material science and condensed matter physics because of their reliability and local descriptions of material properties. Properties of materials are often not directly accessible from experiments for many reasons. For example, the sample size of certain materials may not sufficiently large enough for certain experiments. One real example is a single nanotube that cannot be easily studied with synchrotron beam (a powerful light source) that has beam diameter in the range of several micrometers. Another big advantage of computational methods over experimental work is in studying hyphothetical systems that have never been produced. However, as the reliability of computational results is always based on the experimental results, both the computational methods and the experimental methods should considered to be complement to each other. In the last few decades, ability of computer to perform large scale calculations has been significantly increased. The large scale calculations are important in the area of disordered/amorphous materials because these materials lack translational periodicity (unlike crystals) and require many particle models (supercells).

2.2   Density functional theory (DFT)

Density functional theory (DFT) is based on the notion that that ground state properties of a many body system can be in terms of single particle electron density that is considered a fundamental variable. As laid out by Hohenberg and Kohn [25], the theoretical foundation of DFT is based on two fundamental statements. The first one states that for any system of electrons in an external potential $V_{ext}(\mathbf{r})$, the Hamiltonian is fully governed by the ground state density *i.e.* if the ground state density is determined, ground state properties of the systems are readily known. The ground state energy as a

function of electron density n($\mathbf{r}$) is given by:

$$E[n(\mathbf{r})] = \int V_{ext}(n\mathbf{r})n(\mathbf{r})d^3r + F[n(\mathbf{r})] \tag{2.1}$$

The external potential V_{ext} is the contribution of electron-ion interactions and ion-ion interactions (but not e-e interactions) whereas F[n($\mathbf{r}$)] is a universal functional (in the sense that does not depend on the external potentials) of the density. However, the exact form of F[n($\mathbf{r}$)] is not known. The second statement asserts that the total energy functional E[n($\mathbf{r}$)] is minimized by the true ground state density. F[n($\mathbf{r}$)] can be decomposed as:

$$F[n(\mathbf{r})] = T[n(\mathbf{r})] + E_H[n(\mathbf{r})] + E_{xc}[n(\mathbf{r})] \tag{2.2}$$

where

$$E_H[(\mathbf{r})] = \frac{e^2}{2} \int \int \frac{n(\mathbf{r})n(\mathbf{r'})}{\mathbf{r} - \mathbf{r'}} d^3r d^3r' \tag{2.3}$$

is the Hartree term (interaction of the electrons). T and E_{xc} respectively are the kinetic energy of a noninteracting electron gas of density n and the exchange-correlation energy which is not a straight forward functional of n.

Kohn and Sham [26] have provided a practical means to solve these equations by introducing single-particle orbitals known as Kohn-Sham orbital $\psi_i(\mathbf{r})$ to solve Schrodinger-like Khon-Sham equation:

$$\left[-\frac{1}{2}\nabla^2 + V_{eff}(\mathbf{r}) \right]\psi_i(\mathbf{r}) = \epsilon_i\psi_i(\mathbf{r}) \tag{2.4}$$

where

$$V_{eff}(\mathbf{r}) = V_{ext}(\mathbf{r}) + \int d(\mathbf{r'})\frac{n(\mathbf{r})}{|\mathbf{r} - \mathbf{r'}|} + V_{xc}(\mathbf{r}) \tag{2.5}$$

with

$$V_{xc}(\mathbf{r}) = \frac{\delta E_{xc}}{\delta n(\mathbf{r})} \tag{2.6}$$

The charge density n($\mathbf{r}$) is given by:

$$n(\mathbf{r}) = 2 \sum_i |\psi_i(\mathbf{r})|^2 \tag{2.7}$$

The Kohn-Sham (KS) equation 2.4 is non-linear and must be solved self-consistently because V_{eff} is a functional of density n and n is determined from the soluction of KS equation 2.4. As soon as the self-consistent solution of KS equation is obtained, the ground state density and hence all its properties are readily available.

DFT assumes that there exists a form of the potential V_{eff} that depend only on electron density n($\mathbf{r}$), yielding an exact ground state energy. But this exact form is unknown requiring an approximation to be used. The simple approximation is the local density approximation (LDA) where E_{xc} is defined as:

$$E_{xc} = \int d^3 r \epsilon_{xc}[n(\mathbf{r})].n(\mathbf{r}) \tag{2.8}$$

where ϵ_{xc} is the exchange correlation energy per unit volume of a homogeneous electron gas of density n.

The LDA assumes that the exchange correlations are slowly varying in space which may not be always true and hence there exists an another approximation known as generalized gradient approximation (GGA). GGA considers ϵ_{xc} to be function of density as well as the gradient of the density at each point.

2.3   Molecular Dynamics simulation

Molecular Dynaimcs (MD) is a standard method of generating computer models of amorphous materials. In MD atoms are represented by point particles and the classical Newton equations of motion are numerically integrated. Given initial positions of atoms, the force on each atom may be computed and a new position of each atom is then predicted. The MD simulations superficially mimic the experimental process of glass formation. Amorphous materials are modeled through a molecular dynamic process called ``cook and quench´´method mimicking a whole set of experimental methods.

2.4   *Ab initio* **Molecular Dynamics simulation**

As pioneered by Car and Parrinello [27] and Sankey [28] in mid eighties, the
accuracy of ab initio density functional (DF) methods with force calculations can be
combined with the molecular dynamics techniques. In *ab initio* molecular dynamics
(AIMD), the nuclei are treated as classical particles which move in a potential determined
by density functional theory. Although AIMD is much more accurate than classical MD, it
is computationally expensive and limited to only few hundred atoms whereas thousands of
atoms can be easily handled by classical MD. However the advantage of AIMD over
classical MD is that in AIMD, only the information about the atomics species and the
positions of the atoms within the system is required. In contrast, classical MD requires
empirical or semi-empirical potentials whose parameters are usuall derived by fitting the
outcome of simulated data to experimental data making the parameters system dependent.
It is therefore hard to find a universal set of parameters for empirical potentials. This
problem is even worse in amorphous/disordered materials and hence AIMD is the best
choice in these systems. The potentials used in AIMD are determined by the electronic
structure of the species and therefore will be universal for all systems.

2.5   **Pseudopotential Method**

Since the electronic structure of a system mainly depends on the valence electrons,
their interaction with the ions and the core electrons can be approximated by a simplified
effective potential called pseudopotential[29]. In other words the pseudopotenial is an
attempt to replace the complicated effects of the motion of the core electrons of an atom
and its nucleus with an effective potential. This then reduces the number of electrons
explicitly from atomic number (Z) to valence electrons (Nv). A valence electron
experiences Coulomb forces as well as a repulsive force in the core region as a
consequence of Pauli exclusion principle forcing the the valence wavefunctions to be

orthogonal to the core wave functions which in trun makes the radial part of the valence wavefunctions vary rapidly within the core region[29]. The valence electrons experience a very weak potential in the atomic core region as the attractive and repulsive forces cancel each other to a great extent. This is why the replacement of the inner core region potential with a weak effective potential is possible while maintaining the correctness of physics outside the core. The pseudopotential and pseudo wavefunctions match outside a core region *i.e.* above a certain cutoff radius r$_c$ as shown in Fig. 2.1.
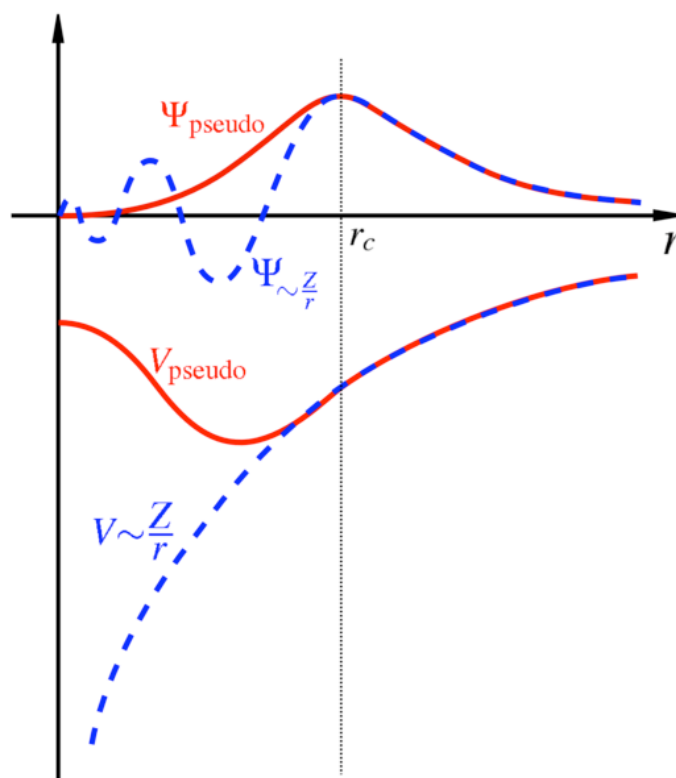
Figure 2.1:   Comparison of a wavefunction in the Coulomb potential of the nucleus (blue) to the one the pseudopotential (red).   the real and the pseudo wavefunction and potentials match above a certain cutoff radius r$_c$.   Source (http://en.wikipedia.org/wiki/Pseudopotential)

3 EXTENDED X-RAY ABSORPTION FINE STRUCTRE: AN EXPERIMENTAL APPROACH

3.1 Introduction

EXAFS spectroscopy has been widely used to probe local structures, particulary in amorphous materials. Since the long-range translational periodicity is lost in amorphous materials, a probe of the local environment is key to understanding the properties of these materials. EXAFS spectroscopy has an edge over other experimental methods, as this method is independent of the phase of the materials to be examined. The same technique can be used to investigate amorphous, crystalline and even liquid states and hence a contrast between different phases becomes apparent even before the detailed analysis.

3.2 Theory of EXAFS

X-ray, an electromagnetic wave with very short wavelengths ranging from 0.01Å to 100Å, can be absorbed by all matters through a photoelectric process. X-ray absorption spectroscopy is based on the absorption of X-ray photons with sufficiently high energy by an absorbing atom ejecting a core electron thereby leaving the atom in an excited state with an empty electron orbital called a core hole. The excited electron also known as photoelectron has a kinetic energy (E_k) that equals the difference between the incoming photon energy ($h\nu$) and the binding energy (E_b) of the electron.

$$E_k = h\nu - E_b \tag{3.1}$$

The fraction of an incident X-ray photon being absorbed per unit thickness by an atom (or materials) is defined as an absorption coefficient μ. μ increases strongly giving rise to a step-like feature called an absorption edge when the x-ray energy is equal to the binding energy E_b of the core-electron. The absorption edge, which is unique for each absorbing element, corresponds to an x-ray photon that has enough energy to free an electron in the

atom[4]. The absorption edge corresponding to innermost electron i.e. n=1 shell, is known as K-edge. Similarly the higher shells correspond to L-edge, M-edge and so on.

3.2.1   X-ray Absorption by an Isolated Atom

When an x-ray with sufficient high energy is absorbed by an atom, a core electron is ejected from the core level, and a photoelectron with a wave number k is created and propagates away from the atom. The absorption however depends on existance of an available state for the photoelectron *i.e.* there will be no absorption providing no available state. For example, an incident x-ray photon with energy smaller than the binding energy of 1s electron will only be sufficient to promote 1s electron to other higher levels (valence levels) below the binging energy (or Fermi level) but there is no level left for 1s electron since all the valence levels are already filled. In such a case there will be no absorption from the core level however, there will still be some absorption from the higher level electrons.

The absorption coefficient ($\mu(E)$) can be described by the Fermi's Golden Rule since x-ray absorption is a transition from one energy eigenstate (x-ray and a core-electron) into a continuum of energy eigenstates (a core hole and a photoelectron). Let us define the initial state as $|\, i \rangle$ and the final state as $|\, f_0 \rangle$. We can now define $\mu(E)$ as;

$$\mu(E) \propto |\langle i \mid H \mid f_0 \rangle|^2 \tag{3.2}$$

3.2.2   X-ray Absorption by a Condensed Matter

When an X-ray photon is absorbed by an atom in a condensed matter where the atom is surrounded by neighboring atoms, the absorption coefficient μ is not as simple as in the case of an isolated system. As shown in Fig. 3.1, the absorption coefficient shows an additional characteristic (an oscillation just above the absorption edge) along with two other characteristics already obserbed for isolated atoms[21]. When the absorbing atom is
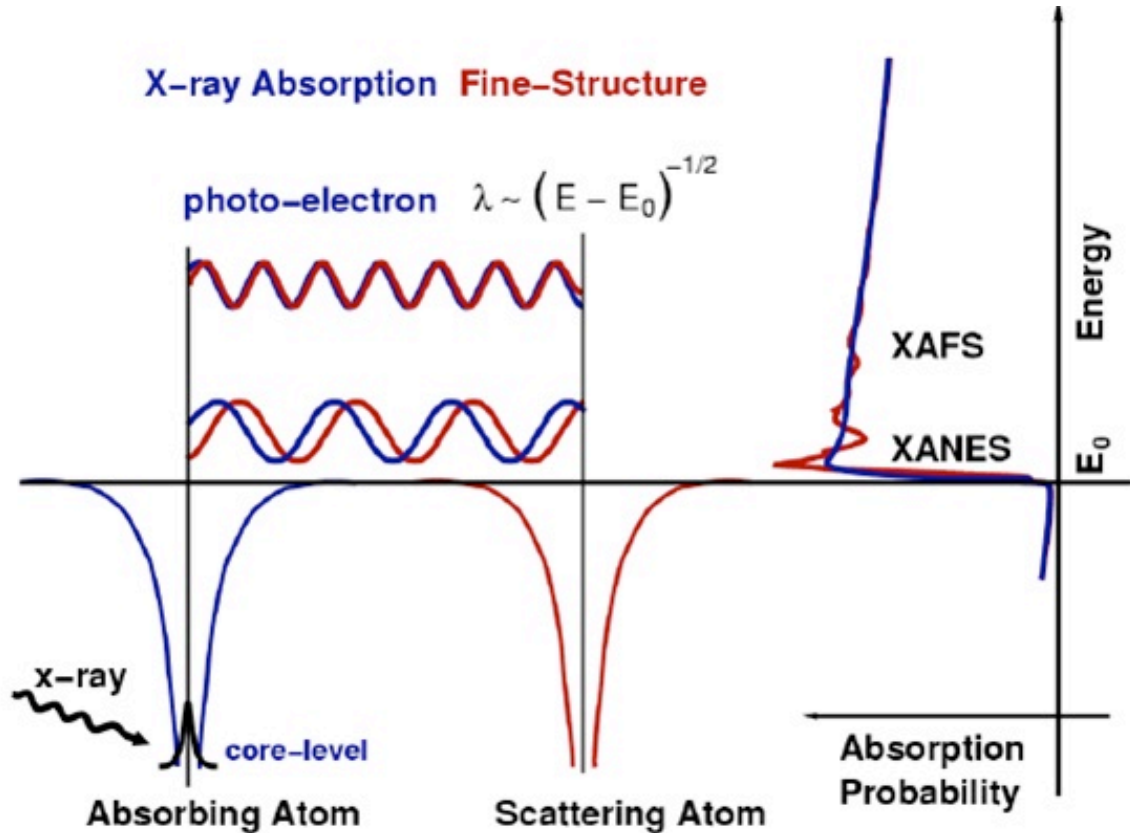
Figure 3.1: Origin of the x-ray absorption fine structure. [Ref. [21]]

surrounded by neighboring atoms, the outgoing photoelectron which can also be

represented as an outgoing electron wave is scattered by the electrons of the neighboring

atoms, and the scattered photoelectron can return to the absorbing atom hence giving the

final state as the superposition of the outgoing and the scattered waves. The modification

of the absorption coefficient due to scattering of the photoelectron by the surrounding

atoms is the origin of XAFS. Again we describe $\mu(E)$ with Fermi's Golden Rule as:

$$\mu(E) \propto | \langle i \mid H \mid f \rangle |^2 \tag{3.3}$$

The initial state $\mid i \rangle$ of the the core-level electron, which is very tightly bound to the

absorbing atom, will not be altered by the presence of the neighboring atoms. It is only the

final state $| f \rangle$ that is altered due to the presence of neigboring atoms. The final state can

be expanded as [4]

$$| f \rangle = | f_0 \rangle + | \Delta f \rangle \tag{3.4}$$

where $| f_0 \rangle$ is the final state as in absorption by an isolated atom and $| \Delta f \rangle$ is the effect

of the neighboring atoms. We can now expand Eq. 3.3 as

$$\mu(E) \propto | \langle i \mid H \mid f_0 + \Delta f \rangle |^2 \tag{3.5}$$

$$\mu(E) \propto | \langle i \mid H \mid f_0 \rangle |^2 + \{ \langle i \mid H \mid f_0 \rangle \langle \Delta f \mid H \mid i \rangle^* + c.c. \} + ... \tag{3.6}$$

$$\mu(E) \propto | \langle i \mid H \mid f_0 \rangle |^2 \ \{ 1 + [\frac{\langle i \mid H \mid f_0 \rangle \langle \Delta f \mid H \mid i \rangle^*}{| \langle i \mid H \mid f_0 \rangle |^2} + c.c.] + ... \} \tag{3.7}$$

where c.c. in Eq.3.7 is the complex conjugate of the preceeding expression. The first

term of Eq.3.7, that is proportional to $| \langle i \mid H \mid f_0 \rangle |^2$, refers to the absorption coefficient of

the free absorber μ_0 (Eq.3.2) and the second term refers to the EXAFS oscillations $\chi(E)$.

The higher term that is proportional $| \langle \Delta f \mid H \mid i \rangle |^2$ can be neglected since $(\mu - \mu_0) \ll \mu$.

The absorption coefficient μ of an absorber in condensed matter can be written as

$$\mu(E) = \mu_0(E)(1 + \chi(E)) \tag{3.8}$$

$\chi(E)$ is also known as x-ray absorption fine structure and can be written as

$$\chi(E) \propto \langle i \mid H \mid \Delta f \rangle \tag{3.9}$$

The peaks in the EXAFS correspond to the backscattered wave being in phase with

the outgoing wave whereas the valleys correspond to these being out of phase. Since

atoms have different scattering strength, the variation of EXAFS depends on the type of

atom giving the backscattering. Hence EXAFS contains information about the atomic

surroundings of the center atom, and with a more quantitative analysis of EXAFS it is

possible to obtain this information[4]. Conventionally, the EXAFS oscillations are often

defined with respect to the photoelectron wave number k:

$$k = \sqrt{\frac{2m_e}{\hbar^2}(\hbar\omega - E_o)} \qquad (3.10)$$

where E_o is the binding energy of the core-electron that is excited and $\hbar\omega$ is the

energy of the absorbed x-ray photon. The EXAFS in the single scattering approximation

can be expressed as[4]:

$$\chi(k) = \sum_s \frac{NA(k)S_0^2}{kR^2} e^{-\frac{2R}{\lambda(k)}} e^{-2k^2\sigma^2} sin(2kR + \phi(k)) \qquad (3.11)$$

Here A(k) is the backscaterring amplitude from each of the N neigbhoring atoms to

the central atom at distance R away. $\phi(k)$ is the total phase shift experienced by the

photoelectron whereas $\lambda(k)$ is the electron mean free path as a functio of k. $S_o^2(k)$ is the

amplitude reduction factor due to many-body effects at the central atom. σ is the

Debye-Waller factor which accounts for thermal vibration and static disorder.

3.3   Data Analysis

3.3.1   Data Collection

The EXAFS experiment was conducted at the 5-BM beamline of the Advanced

Photon Source (APS), Argonne National Laboratory. The synchrotron ring was operated

at 7GeV in a standard top-up mode with a constant beam current of 100 mA. The EXAFS

spectra were measured either under transmission mode or under fluorescence mode. The

transmitted X-ray beams were measured by the ionization chamber and the fluorescence

signals from the samples were collected by a 13-element Ge detector at room temperature.

A reference sample that contains the elements present in the sample was used as a

reference to calibrate the X-ray energy for different scans at the same K edges. Fig. 3.2

shows an absorption spectrum of amorphous $Ge_1Sb_2Te_4$ measured at Ge K edge.
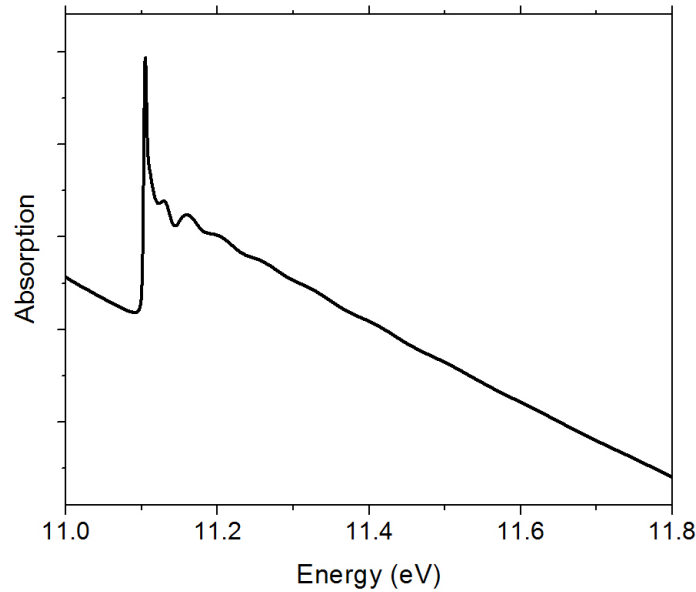
Figure 3.2: Absorption spectrum of a-Ge$_1$Sb$_2$Te$_4$ measured at Ge K edge in transmission mode.

3.3.2 Background Removal and Data Reduction

Analysis of the data starts with a reduction of measured raw absorption spectra into EXAFS spectra. This data reduction involves the normalization and conversion into k spectra from the raw absorption spectra using equations[4]:

$$k = \sqrt{\frac{2m_e(E - E_o)}{\hbar^2}} \tag{3.12}$$

$$\chi(k) = \frac{\mu - \mu_o}{\mu_o} \tag{3.13}$$

where, E_o is the threshold energy or the binding energy of the photoelectron, μ is the observed absorption coefficient and μ_o is the absorption that would be observed in the absence of EXAFS effects. It is based on the assumption that μ_0 is represented by the smooth part of μ and hence $\mu - \mu_o$ gives the required oscillatory part[5]. Here the division by μ_o is to normalize the EXAFS oscillations (Fig. 3.3). EXAFS represents the average structure around absorbing atoms. Since μ_o cannot be directly measured, it has to be approximated by fitting μ with some polynomial splines or using a least square procedure.

In this work we used a package called ATHENA[6] for this purpose. ATHENA approximates the background via linear approximation (to the pre-edge) and via spline function (to the atomic background).

(a)   (b)
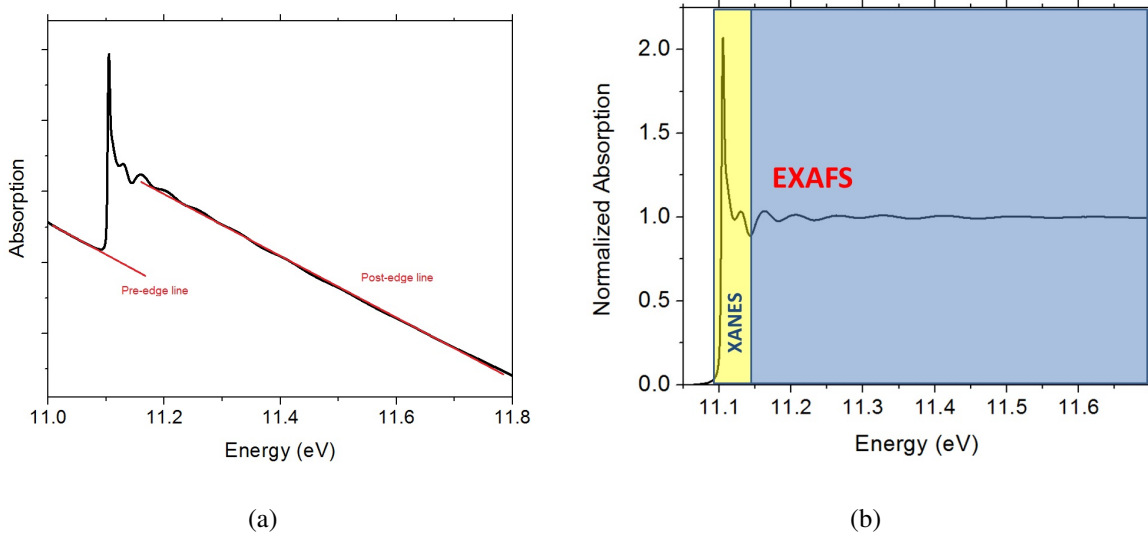
Figure 3.3: Absorption spectrum and Normalized absorption spectrum at Ge K edge. Difference between pre-edge and post-edge lines (in red) is used to normalize the absorption spectrum. The part of spectrum about ±50eV around the absorption edge is known as XANES while the EXAFS begins about 50eV above the absorption edge.

3.3.3   Determination of Structural Parameters

The next step is to analyze the $\chi(k)$ (Fig. 3.4(a)) data to obtain structural parameters such as bond length(R), coordination number (N) and mean squared relative displacement (σ^2) which are obtained by optimizing the parameters in an equation:

$$\chi(k) = \sum_s \frac{NA(k)S_0^2}{kR^2} e^{-\frac{2R}{\lambda(k)}} e^{-2k^2\sigma^2} sin(2kR + \phi(k)) \tag{3.14}$$

The parameters A(k), S_0^2, $\phi(k)$ and $\lambda(k)$ that define scattering are determined using model compounds of known structure. Equation 3.14 is however based only on the assumption that the X-ray excited photoelectron undergoes a single scattering before returning to the

absorbing atom. In fact, the photoelectron can undergo multiple scattering (scattered by more than one atom). This multiple scattering is more effective at low k while less effective at high k and is important while dealing with XANES. Analysis of EXAFS data in this work is based on single scattering of the X-ray excited photoelectron. The scattering paths and phase shift information are calculated by using FEFF[7] using a model compound of known structures. FEFF uses a scattering path formalism to compute the EXAFS spectrum. For every scattering path, determined by FEFF, with a path length below a cut-off length the EXAFS contribution is computed to obtain the backscattering amplitude $A(k)$, phase shifts $\phi(k)$ and the mean free path $\lambda(k)$ which are then stored individually for each path.

Finally the structural parameters in the expression of $\chi(k)$ are optimized by using ARTEMIS[6]. Least square fitting to equation 3.14 starts with defining at least four parameters: a change in the effective path length ΔR, debye-waller factor σ^2, an amplitude NS_0^2 and an energy shift ΔE_0 for each of the paths included in the fit[21]. Fig. 3.4(b) illustrates an example of fitted spectrum.

(a)   (b)
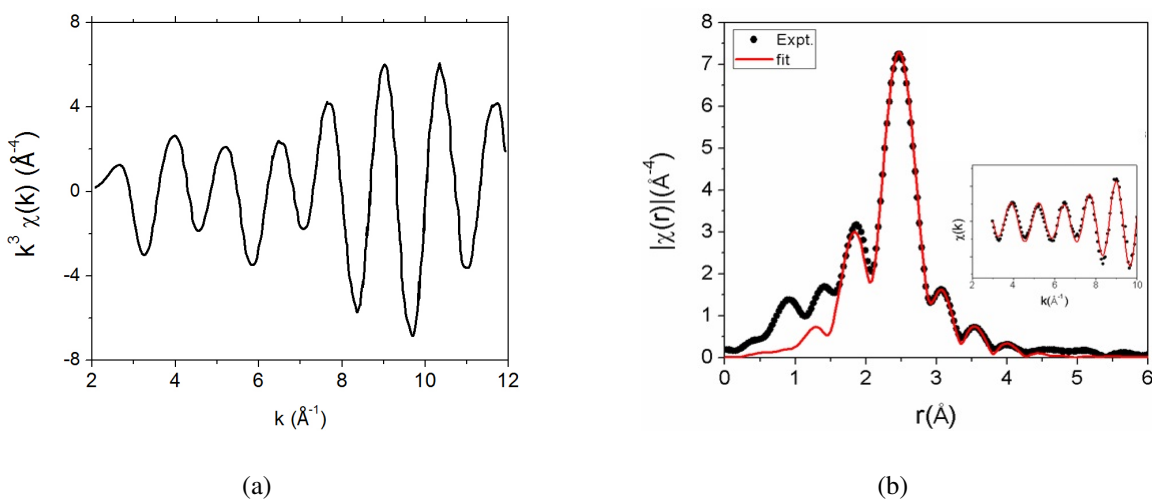
Figure 3.4: a) k^3 weighted $\chi(k)$ spectrum and b) the Fourier Transform of $\chi(k)$. Least square fit is also illustrated in b).

4 PROPERTIES OF AMORPHOUS AND CRYSTALLINE TITANIUM DIOXIDE FROM FIRST PRINCIPLES.

B. Prasai, B Cai, M. Kylee Underwood, James P. Lewis, and D. A. Drabold

Properties of amorphous and crystalline titanium dioxide from first principles

Journal of Materials Science, **47**, 7515-7521(2012).

4.1 Introduction

The discovery of titanium dioxide's ability to split water by photocatalysis under ultraviolet light by Fujishima and Honda [30], has led to enormous work on the material(see Ref. [31] for a recent review). The hope is that titanium dioxide (TiO_2), widely used as a pigment in white paint and in sunscreen, may prove to be an economical material for use in photovoltaic, photocatalytic, and sensing applications [31].

The majority of studies on titania are based upon three crystalline phases (anatase, rutile, and brookite), as well as in multiple forms (bulk, nanoparticle, thin film, etc.). However, titania is naturally obtained as powder consisting of a mixture of crystalline and amorphous phases. Various methods have been employed to enhance the crystalline quality of titania(e.g. Ref. [32]). However, recent research, including the results presented herein, has focused on understanding the structural and electronic properties of amorphous titania(a-TiO_2) with the hope that the desirable properties of TiO_2 can be found in this less processed, thus cheaper, form of the material [33–38]. For example, a-TiO_2 has been synthesized as a tinted or enhanced photocatalyst [39, 40], used to purify dye-polluted water [41], and applied to resistive random access memory applications [42]. As more synthesis techniques, like those of Battiston *et al.*[43] and Zhao *et al.*[44], are developed to create amorphous TiO_2 thin films, amorphous titania will be used in applications

traditionally reserved for crystalline TiO_2 or other more expensive amorphous films. Through our research we aim for a deeper understanding of the energetic and electronic properties of a-TiO_2 while confirming structural properties to aid in the development of these materials as a viable solution to current energy and environmental issues.

4.2 Methods

We used the Vienna *ab initio* simulation program(VASP), a density functional code employing a planewave basis[45–47] to generate 96-atom and 192-atom structures of a-TiO_2 and crystalline TiO_2 (Rutile and Anatase) structures. Vanderbilt ultra-soft pseudopotentials [48] were used with the generalized gradient approximation (GGA) of Perdew-Wang 91[49] throughout the calculations. We performed all molecular-dynamics simulations with a 1.6 fs time step using periodic boundary conditions at constant volume for annealing, equilibrating and cooling, as well as a zero pressure conjugate gradient (CG) for relaxation (a safe 450 eV energy cutoff was used for the relaxation). The details of these simulations to generate the amorphous and crystal structures are presented herein. A preliminary form of this work appeared in a proceedings paper[50].

4.2.1 Amorphous TiO_2

We created a 192-atom model (64 Ti atoms and 128 O atoms) with a mass density of 3.8 g/cm^3; a smaller 96-atom supercell was cut out of the 192-atom system. The final models were then prepared by using the method of melt quenching [51]. Using this approach, we annealed the 192-atom model, then we equilibrated at 2500K for 8ps, well above the melting point (2116K). We cooled this liquid TiO_2 system to 2200K (slightly above the melting point) over 4.8ps, and then equilibrated for another 4.8ps. After these initial annealing and cooling simulations, we further cooled the TiO_2 system to 1100K at the rate of 75K/ps. At this stage in the procedure, we were able to observe primary structural features of a-TiO_2. After we equilibrated the system for another 2ps at 1100K,

we further cooled the model to 300K at the rate of 200K/ps. After equilibrating for another 3.4ps at 300K, we quenched the model to its final ground state, fully optimized, structure. Two 96-atom model systems were prepared, using the same method as for the 192-atom model system, using two different rates of cooling (90K/ps and 75K/ps) between 2200K and 1100K. The densities of all amorphous models were calculated after zero-pressure relaxation, and presented in Table 4.1.

4.2.2 Crystalline TiO$_2$

We used $2 \times 2 \times 2$ supercells for both rutile TiO$_2$ (32 atoms) and anatase TiO$_2$(96 atoms) structures using the lattice parameters as provided in Ref. [52]. Both of the supercells were relaxed at zero pressure with CG option of VASP under similar condition as in a-TiO$_2$. For rutile supercell, a $4\times4\times6$ Monkhorst-Pack grid[53] was used for Brillouin-zone sampling whereas a $4\times4\times2$ grid was used for anatase supercell. The calculated densities and lattice parameters are presented in the Table 4.1 and 4.2 respectively.

Table 4.1: Densities and Total energies of a-TiO$_2$ models compared to crystalline phases.

Model	Density (g/cm^3) (this work)	Density (g/cm^3) (Expt.[52])	E$_{tot}$/atom (eV)
96-atom model I	3.59		-8.75
96-atom model II	3.56		-8.85
192-atom model	3.73		-8.80
Rutile TiO$_2$	4.13	4.25	-8.93
Anatase TiO$_2$	3.77	3.79	-8.95

Table 4.2: Calculated crystal TiO_2 properties as compared to experiment and other computational methods

	Rutile			Anatase		
	a=b(Å)	c(Å)	u	a=b(Å)	c(Å)	u
This Work	4.64	2.99	0.305	3.83	9.62	0.208
GGA PBE[54]	4.67	2.97	0.305	3.80	9.67	0.207
GGA PW[55]	4.63	2.98	0.305	-	-	-
HF[56]	-	-	-	3.76	9.85	0.202
Expt.[52]	4.594	2.958	0.305	3.785	9.514	0.207

4.3 Results and Discussion

4.3.1 Partial Pair Correlation Functions

We used partial pair correlation functions (PPCF) to examine the local bonding environment of atoms in a-TiO_2. For all models, the PPCF confirmed a chemically ordered system with no homopolar bonding (Fig. 5.2). The use of the "cook and quench" method to fabricate the models is unbiased and its prediction of a perfectly chemically ordered network is therefore significant. This system displays substantial order in the local environment of the atoms marked by sharp initial peaks for all models, but exhibits no long-range order. Of particular interest are the two distinct initial peaks found for all models in the Ti-Ti pair correlation function. These two peaks, also found in a Reverse Monte Carlo (RMC) model[33], are attributed to two different environments for Ti atoms. The first peak corresponds to edge-sharing Ti-Ti pairs, whereas the second peak

corresponds to corner-sharing Ti-Ti pairs. Although there is little variation in first peak position among the three models, the Ti-Ti distance is larger than the value of 3.0Å obtained in the RMC model[33]. By normalizing the PPCF for Ti-Ti, we were able to calculate the fraction of edge-sharing Ti-Ti pairs denoted by this first peak as 0.29, 0.30, and 0.38 for the 96-atom model I, 96-atom model II, and 192-atom model, respectively. For the second peak position we observe a larger variation among the three models (3.48 - 3.59 Å). These two Ti-Ti peaks are not unique to a-TiO$_2$ *i.e.* similar results are observed in crystalline TiO$_2$ with two Ti-Ti peaks at positions of 2.99 Å and 3.60 Å in rutile structure compared to 3.07 Å and 3.83 Å in anatase structure. Similarly, the width of the initial peak in the O-O pair correlation function also suggests both edge-sharing and corner-sharing environments for neighboring oxygen atoms however, not so prominent as in the case of Ti-Ti. Again, the calculated average O-O first peak position(2.85 Å, 2.83 Å and 2.74 Å in 96-atom model I and II, and 192-atom model respectively) is slightly over-estimated in all three models compared to the experimental value of 2.67 Å [33]. Like Ti, O also has both edge sharing and corner sharing environments with O-O distances of 2.56 Å (2.49 Å) and 2.8 Å (2.82 Å) respectively, in rutile(anatase) structure. Conversely, the calculated first peak position in the Ti-O correlation of (1.92 Å - 1.94 Å) is slightly less than the experimental Ti-O average bond distance of 1.96 Å [33]. In crystalline TiO$_2$, two types of Ti-O pairs are observed with bond lengths of 1.98 Å and 2.00 Å in the rutile structure, and 1.96 Å and 2.00 Å in anatase structure. These numbers are however slightly over-estimated compared to those observed experimentally(1.946 Å and 1.984 Å in rutile and 1.937 Å and 1.964 Å in anatase[57]). More detailed information on measured nearest neighbor bond distances is presented in Table 4.3. While all models are consistent with experiment, we attribute variation among the models, both with each other and as compared to experiment, to limited statistics from a small collection of small models. From the PPCF data, we found the mean coordination numbers of Ti to be 5.47,

5.50, and 5.76, and the coordination numbers of O to be 2.73, 2.74, and 2.88 for the 96-atom model I, 96-atom model II, and the 192-atom model, respectively. These results are consistent with the RMC and experimental coordination numbers of Ti (5.6 ±10%) and O (2.8 ±10%) [33]. Complete coordination statistics are presented in Table 4.4. This reveals that the local structure of a-TiO$_2$ resembles that of crystalline TiO$_2$ where Ti atoms prefer to bond with six oxygen neighbors that form an octahedral structure, and O atoms prefer 3 titanium atoms as neighbors.

Table 4.3: Mean nearest neighbor bond lengths in a-TiO$_2$(in Å).Ti-Ti$_1$ and Ti-Ti$_2$ refer to first and second peak of Ti-Ti correlation function.

	Ti-O	Ti-Ti$_1$	Ti-Ti$_2$	O-O
96-atom model I	1.92	3.08	3.48	2.85
96-atom model II	1.91	3.07	3.53	2.83
192-atom model	1.94	3.13	3.59	2.74
RMC + Expt.[33]	1.96	3.00	3.55	2.67
Rutile(this work)	1.97,2.00	2.99	3.60	2.56,2.80
Rutile(Expt.[57])	1.95,1.98	2.96	3.57	2.53,2.78
Anatase(this work)	1.96,2.00	3.07	3.83	2.49,2.82
Anatase(Expt.[57])	1.94,1.96	3.03	3.78	2.45,2.80

4.3.2   Bond Angle Distributions

We plot and analyze the Ti-O-Ti and O-Ti-O angle distributions of all three a-TiO$_2$ models to gain a better understanding of the simulated structures, plotted in Fig. 4.2. When compared to the angle distributions for the rutile and anatase TiO$_2$ bulk crystalline structures, we observed that, much of the local crystalline topology is preserved in a-TiO$_2$.
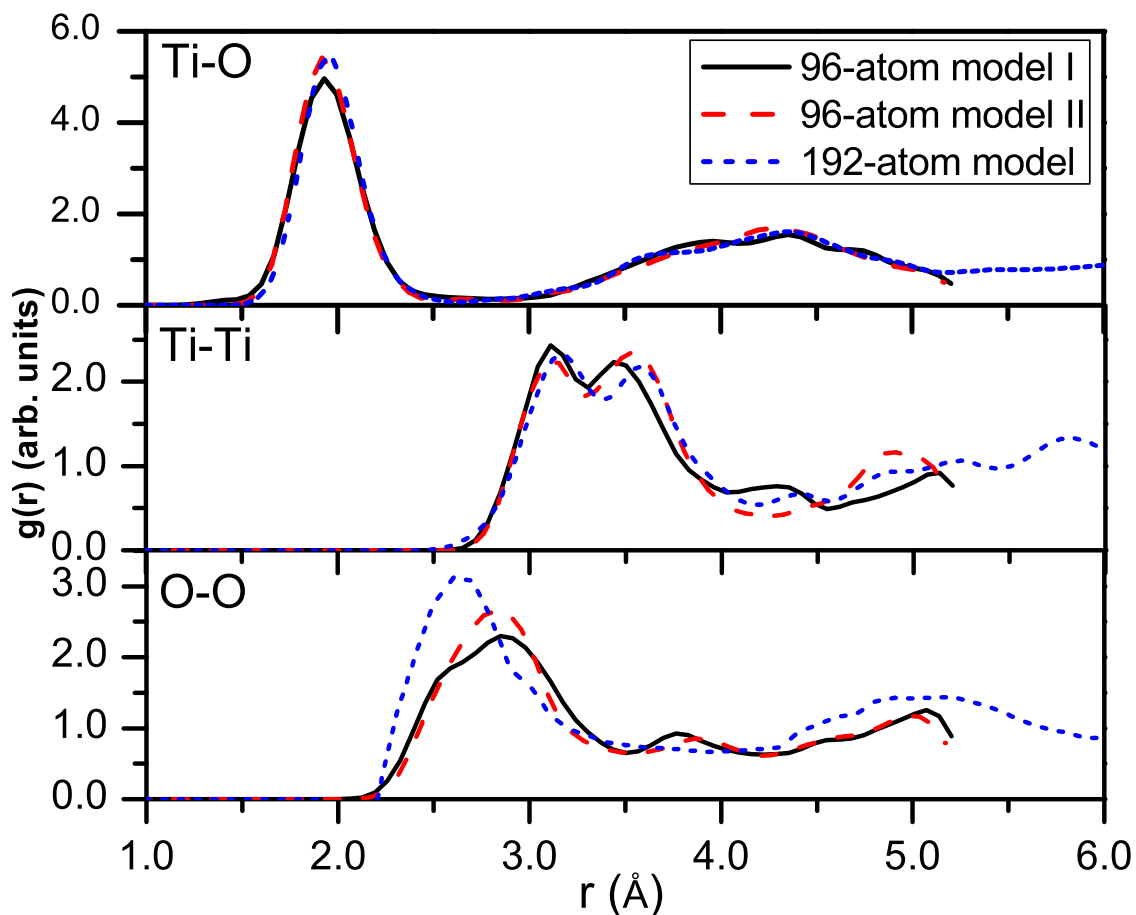
Figure 4.1: Partial pair correlation functions for Ti-O, Ti-Ti, and O-O coordination of the three a-TiO$_2$ models (96-atom model I, 96-atom model II, and 192-atom model) are plotted.

For comparison, the peaks for the Ti-O-Ti angle in anatase are 101.9^o and 156.2^o and in rutile are 98.7^o and 130.6^o; the peaks for the O-Ti-O angle in anatase are 78.1^o, 92.4^o, 101.9^o and 156.2^o and in rutile are 81.3^o, 90°, 98.7^o and 180°. Similar results were reported in ref. [58]. We observe interesting features which appear to be unique to the a-TiO$_2$ models. For instance, in the plotted Ti-O-Ti angle distribution, all of the a-TiO$_2$ models show a large peak positioned near 98°. We attribute this peak to Ti-Ti edge-sharing pairs described by the first peak in the Ti-Ti pair correlation function. The subsequent peaks are therefore attributed to Ti-Ti corner-sharing pairs. The variation among models

Table 4.4: Coordination statistics for amorphous and crystalline TiO$_2$.(in %).

	Ti$_4$	Ti$_5$	Ti$_6$	Ti$_7$	Ti$_8$	O$_2$	O$_3$	O$_4$	O$_5$	N$_{Ti}$	N$_O$
96-atom model I	6.3	46.9	40.6	6.2	–	34.4	57.8	7.8	–	5.47	2.73
96-atom model II	3.1	53.1	37.5	3.1	3.1	29	67.7	3.2	–	5.50	2.74
192-atom model	–	34.4	56.3	7.8	1.6	24.2	64.1	10.9	0.8	5.76	2.88
RMC + Expt.[33]	–	–	–	–	–	–	–	–	–	5.6	2.8
Crystalline TiO$_2$	–	–	–	–	–	–	–	–	–	6.0	3.0

Table 4.5: Comparison of Electronic Gaps (in eV) for different TiO$_2$ structures.

	Rutile	Anatase	a-TiO$_2$
This work	1.73	2.02	2.22
GGAPBE[54]	1.86	2.25	-
PWGGA[55]	1.90	-	-
LDA[59]	1.78	2.04	-
Expt.	3.03[60]	3.20[61]	3.4[62]

of these other peaks is consistent with the variation between models in the position of the second peak in the Ti-Ti pair correlation function. Similarly, we observe an initial peak in the O-Ti-O angle distribution near 75° for all three models and we attribute this peak to O-O edge-sharing pairs while subsequent peaks correspond to O-O corner-sharing pairs.

4.3.3 Electronic Structure

We describe the main features of the electronic structure by analyzing the electronic density of states (EDOS), projected density of states (PDOS), and inverse participation
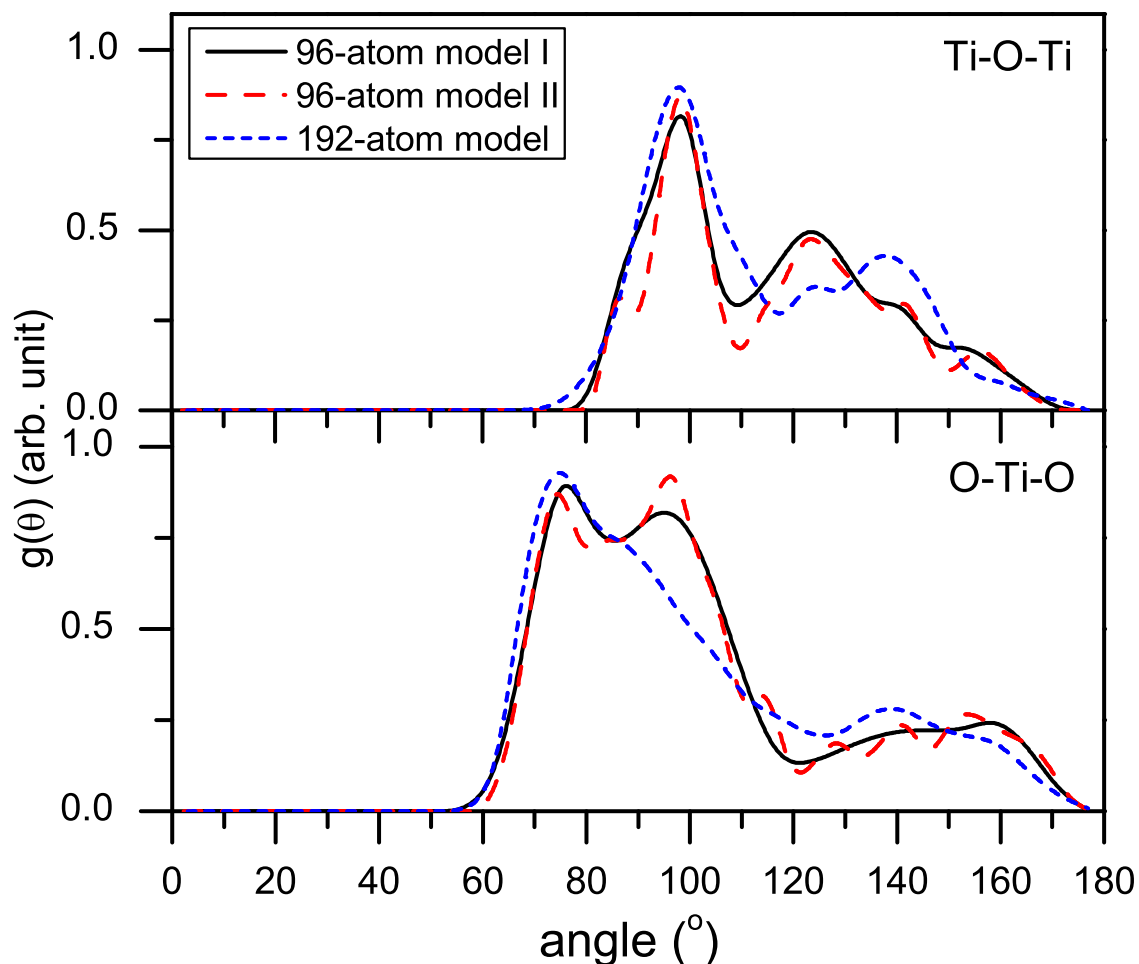
Figure 4.2: Angle distributions are plotted for the three a-TiO$_2$ models (96-atom model I, 96-atom model II, and 192-atom model). For comparison, the peaks for the Ti-O-Ti angle in anatase are 101.9^o and 156.2^o and in rutile are 98.7^o and 130.6^o; the peaks for the O-Ti-O angle in anatase are 78.1^o, 92.4^o, 101.9^o and 156.2^o and in rutile are 81.3^o, 90°, 98.7^o and 180°.

ratio (IPR) of each individual site for each of the three a-TiO$_2$ models. Fig. 4.3 shows the total EDOS of all three models with the Fermi level shifted to 0 eV. Excepting minor variations, the three EDOS are very similar. Furthermore, the total EDOS of a-TiO$_2$ is compared with that of the crystalline TiO$_2$ and presented in Fig.4.4. The total EDOS of the amorphous TiO$_2$ is fairly close to those of crystalline TiO$_2$. For a deeper understanding we also analyzed the PDOS for all three a-TiO$_2$ models. We present the

species PDOS and the orbital PDOS in Fig. 4.5. The lowest conduction band levels(near the Fermi level) are dominated by 3d states of Ti as in crystalline TiO_2 (both rutile and anatase). Also, similar to the crystalline phase, the valence band near the Fermi level has contributions from both 3d states of Ti and 2p states of O with oxygen 2p state dominating the tail region. Interestingly, we find that the Γ-point electronic gap of approximately 2.22 eV is comparable to the calculated results for bulk crystalline TiO_2(1.73eV for rutile and 2.02 for anatase). Similar results, as presented in Table 4.5, are reported from other calculations[54–56, 59].
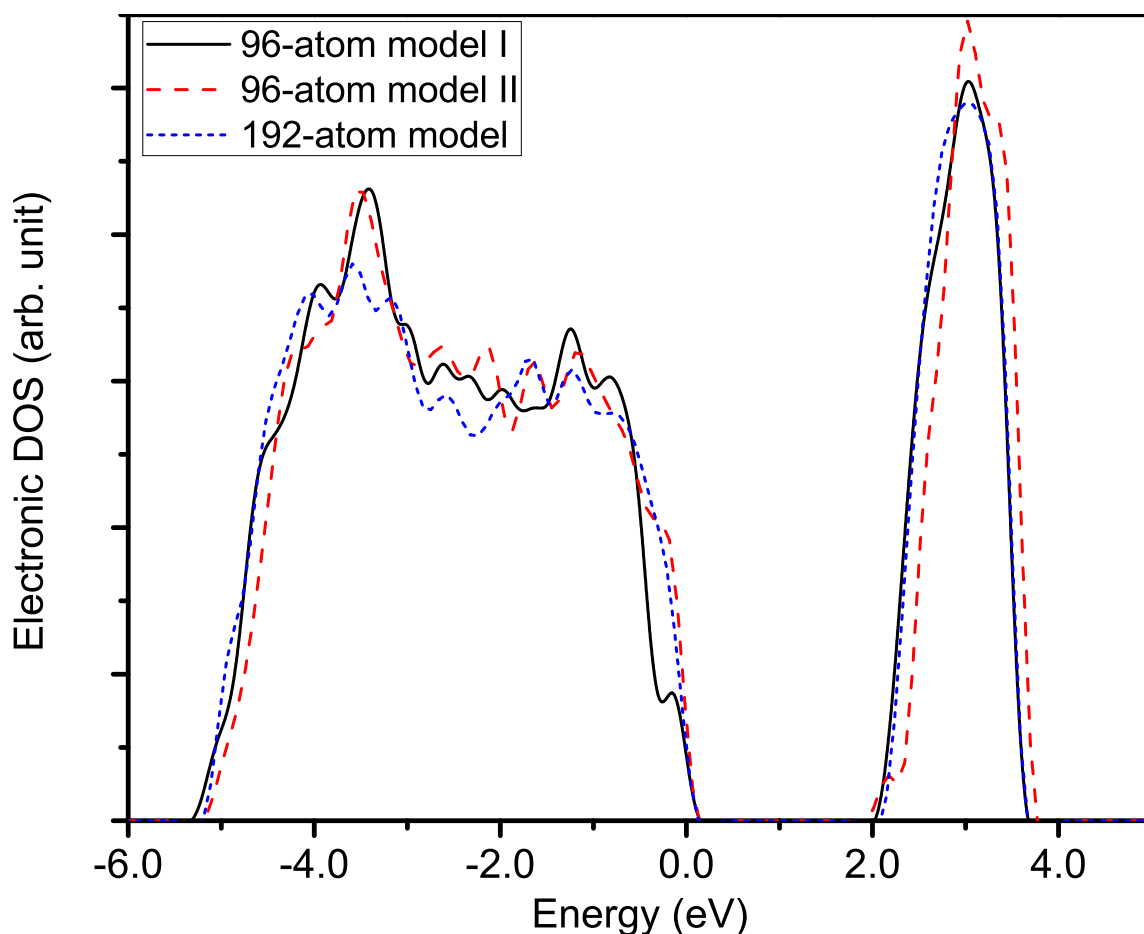
Figure 4.3: Electronic density of states (Γ point) for the three a-TiO_2 models (96-atom model I, 96-atom model II, and 192-atom model).Fermi level is at 0eV.
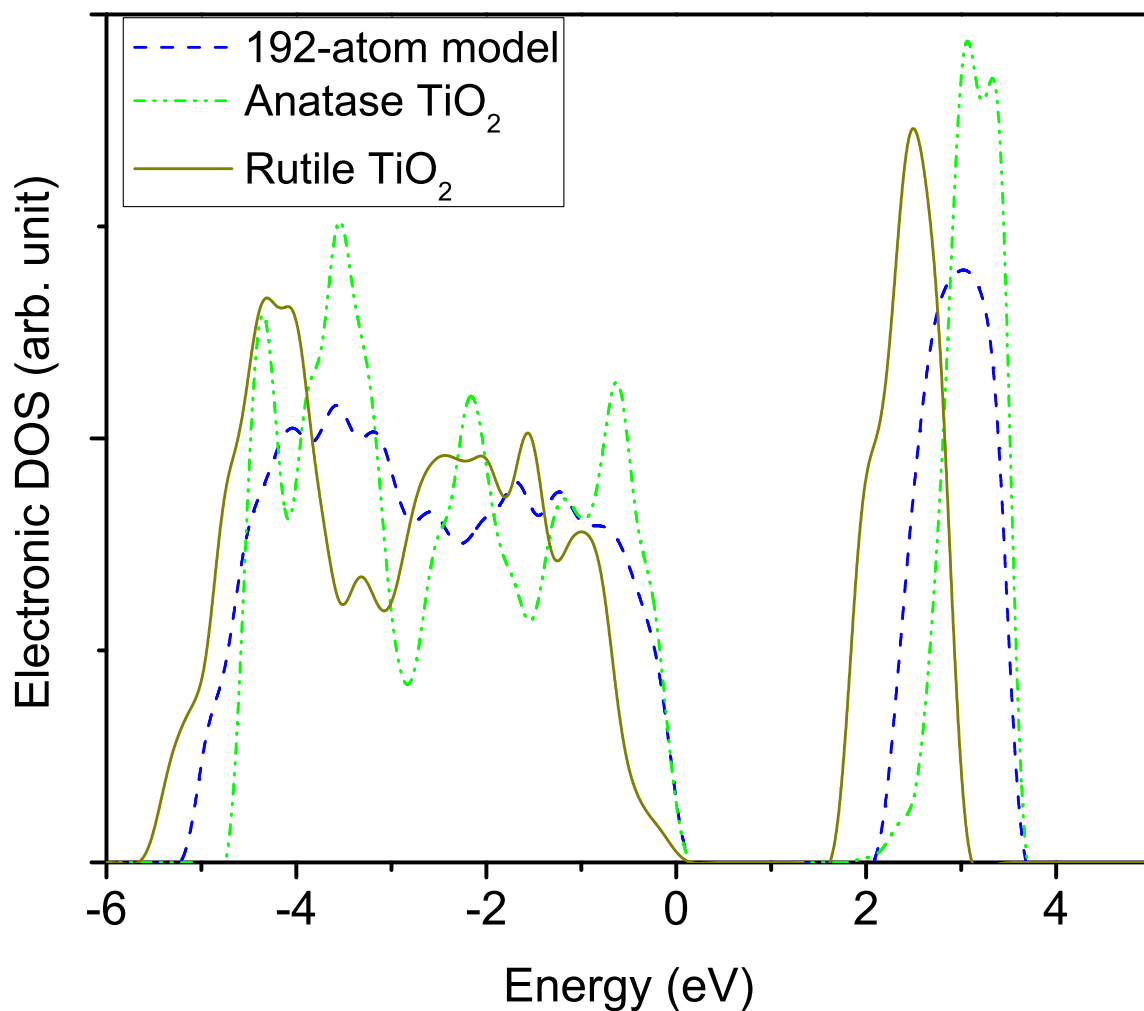
Figure 4.4: Electronic density of states for 192-atom a-TiO$_2$ model as compared with rutile and anatase TiO$_2$. Fermi level is at 0eV.

One of the major characteristics of an amorphous material is the localization of the tail states near the band gap in contrast to the completely delocalized tail states in a crystalline material. We used an Inverse Participation Ratio analysis to investigate the localization of the tail states near the band gap[63] in the a-TiO$_2$ models. Fig.4.6 illustrates the IPR for all three models. Except for the 96-atom model II, we observed that the valence tail states are highly localized. On the other hand, conduction tail states are relatively delocalized(except for in 96-atom model) somewhat reminiscent of a-GaN [64].
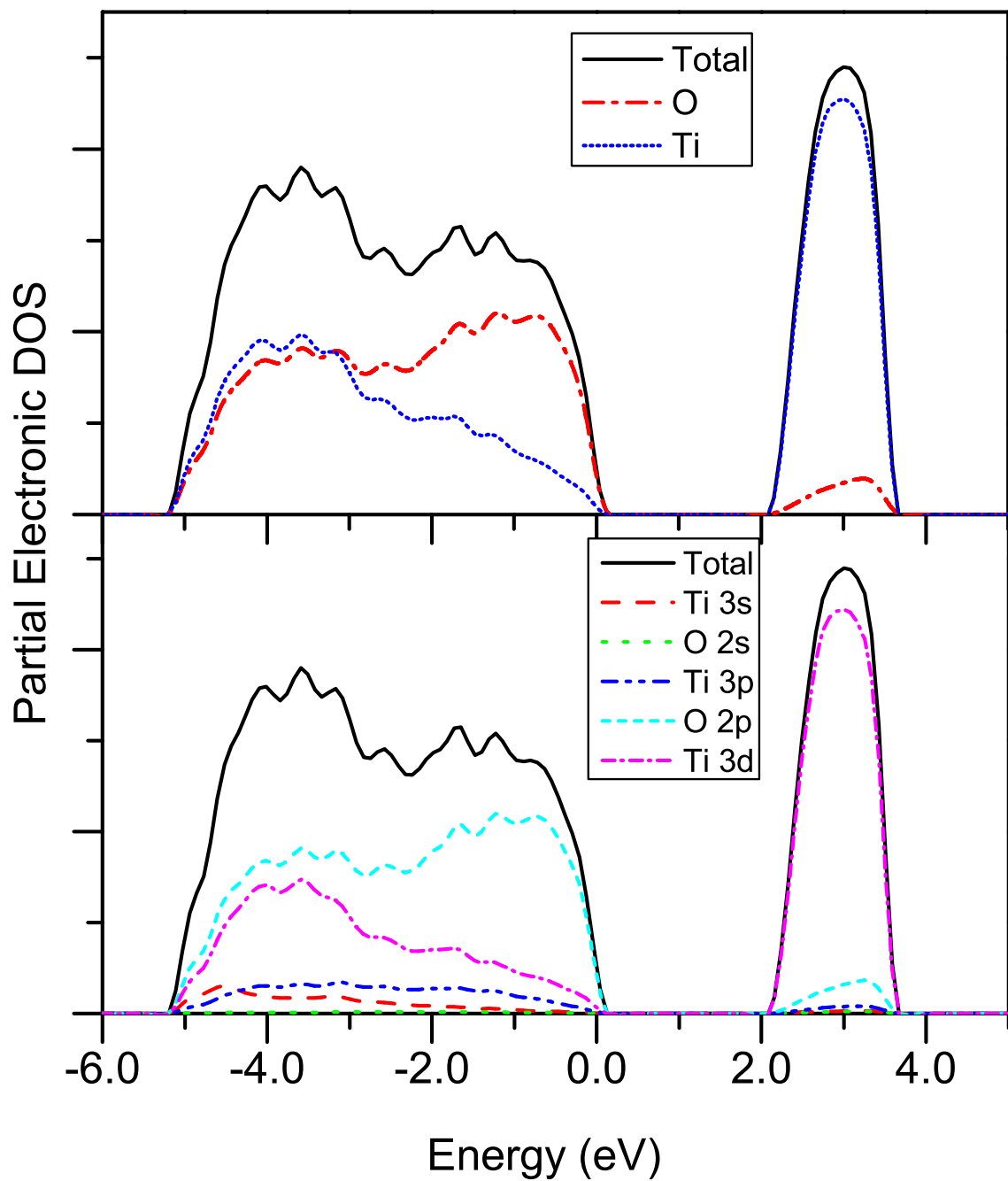
Figure 4.5: Partial electronic density of states (Γ point) for the 192-atom a-TiO$_2$ model. The other two 96-atom a-TiO$_2$ models as well as crystalline TiO$_2$ yield similar results (not shown for simplicity). Fermi level is at 0eV.

The valence tail states are localized on O-2p orbitals whereas conduction tail states are localized on Ti-3d orbitals. We analyzed the topology of the atoms associated with the tail states as indicated in the figure. All of the O atoms associated with the selected valence tail states (a-d) are three-fold coordinated, whereas the Ti atoms associated with the conduction tail states (e-g) are more than six-fold coordinated. However, the O atom is displaced from the plane containing the neighboring Ti atoms, forming a pyramidal structure. This means that the over-coordinated Ti is the cause of the conduction tail states, whereas the positional disorder of O is the origin of the valence tail states.
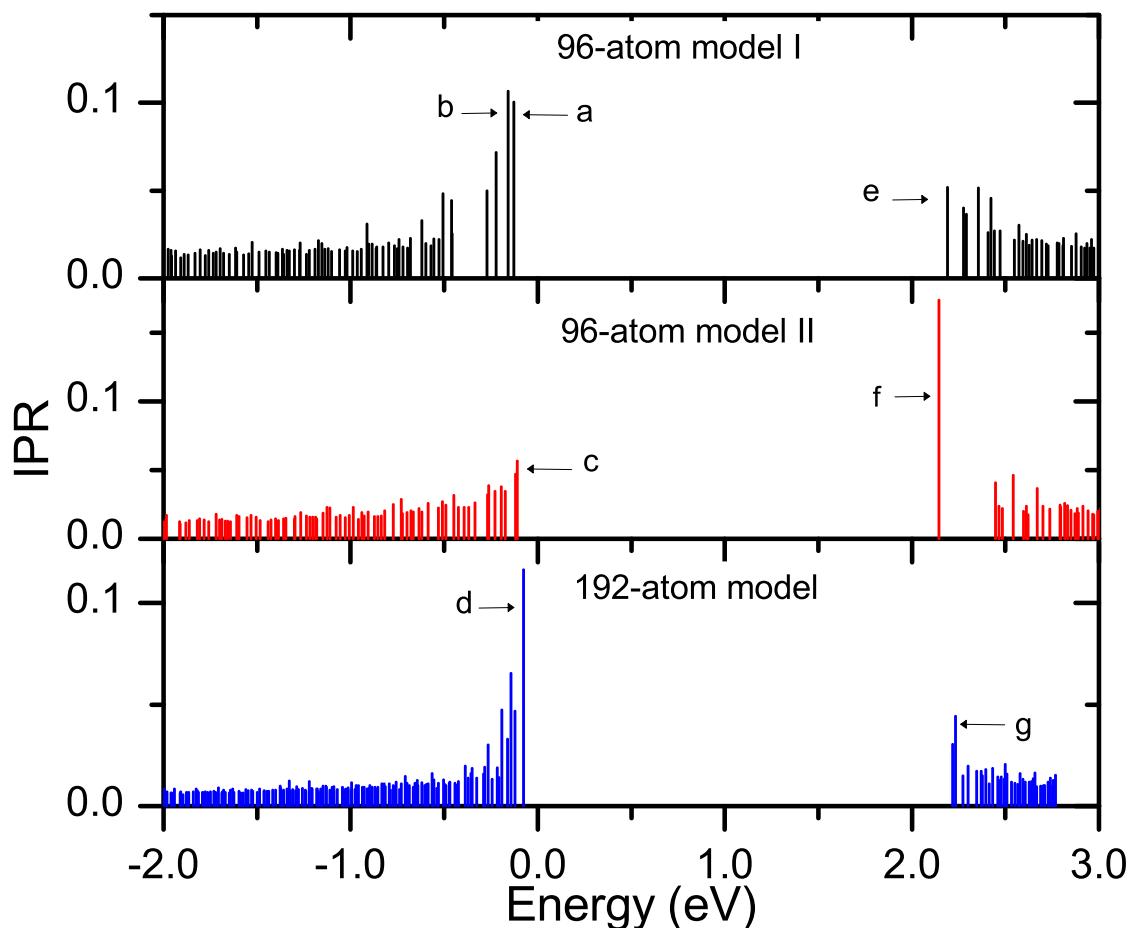
Figure 4.6: Inverse participation ratios are plotted for the three a-TiO_2 models (96-atom model I, 96-atom model II, and 192-atom model). Fermi level is shifted to 0 eV.

4.3.4   Optical Properties

We computed dielectric functions to characterize the optical properties for the crystalline (Rutile and Anatase) and the amorphous phases of TiO_2. figure 4.7 presents the calculated real and imaginary parts of the dielectric functions for the three phases (two crystalline and one amorphous) of TiO_2 as a function of photon energy. Except for a few minor differences, both the real and the imaginary parts of the dielectric functions for anatase TiO_2 and a-TiO_2 closely resemble each other. The similarities of the optical properites between these phases can be attributed to the similar electronic structures. Moreover, the density of the a-TiO_2 is also much closer to that of anatase TiO_2. Rutile TiO_2 has significantly different features from other two phases in both the real and imaginary parts, owing to different electronic structures as compared to those phases. Since the tetragonal cell of rutile and anatase is quite anisotropic, the optical properties are strongly dependent on the direction of the incoming polarized light, whereas, due to the isotropic nature of a-TiO_2 structure, the optical properties are independent on the direction of the incident light. To observe the optical anisotropy in different TiO_2 phases we present the two components(perpendicular and parallel to c axis) of the imaginary parts of the dielectric functions in fig. 4.8. We observed almost no change in the two components for a-TiO_2. The fundamental absorption edge, which results from the interband transition between the topmost valance band (VB) and the bottom of the conduction band(CB), describes the optical band gap. We could not observe the sharp absorption edge which we attribute to the smaller size of the structures. We estimated the absorption edge by extrapolating the perpendicular component of the imaginary part of the dielectric function, and found to be 1.8eV, 2.0eV and 2.4eV for rutile, anatase and amorphous phase respectively. These results for the crystalline TiO_2 phases are consistent with the results in Ref. [59]. The real part of the dielectric function as presented in Fig.4.7(b) is obtained from $\epsilon_2(\omega)$ by a Hilbert transform[65]. The static dielectric constant is obtained from the

real part in the $\omega \to 0$ limit. The calculated values of the static dielectric constant were found to be 5.43, 4.3 and 4.1(average for two models) for the rutile, anatase and amorphous phases respectively. In all respects the optical properties of the a-TiO$_2$ are quite similar to those of anatase phase TiO$_2$.
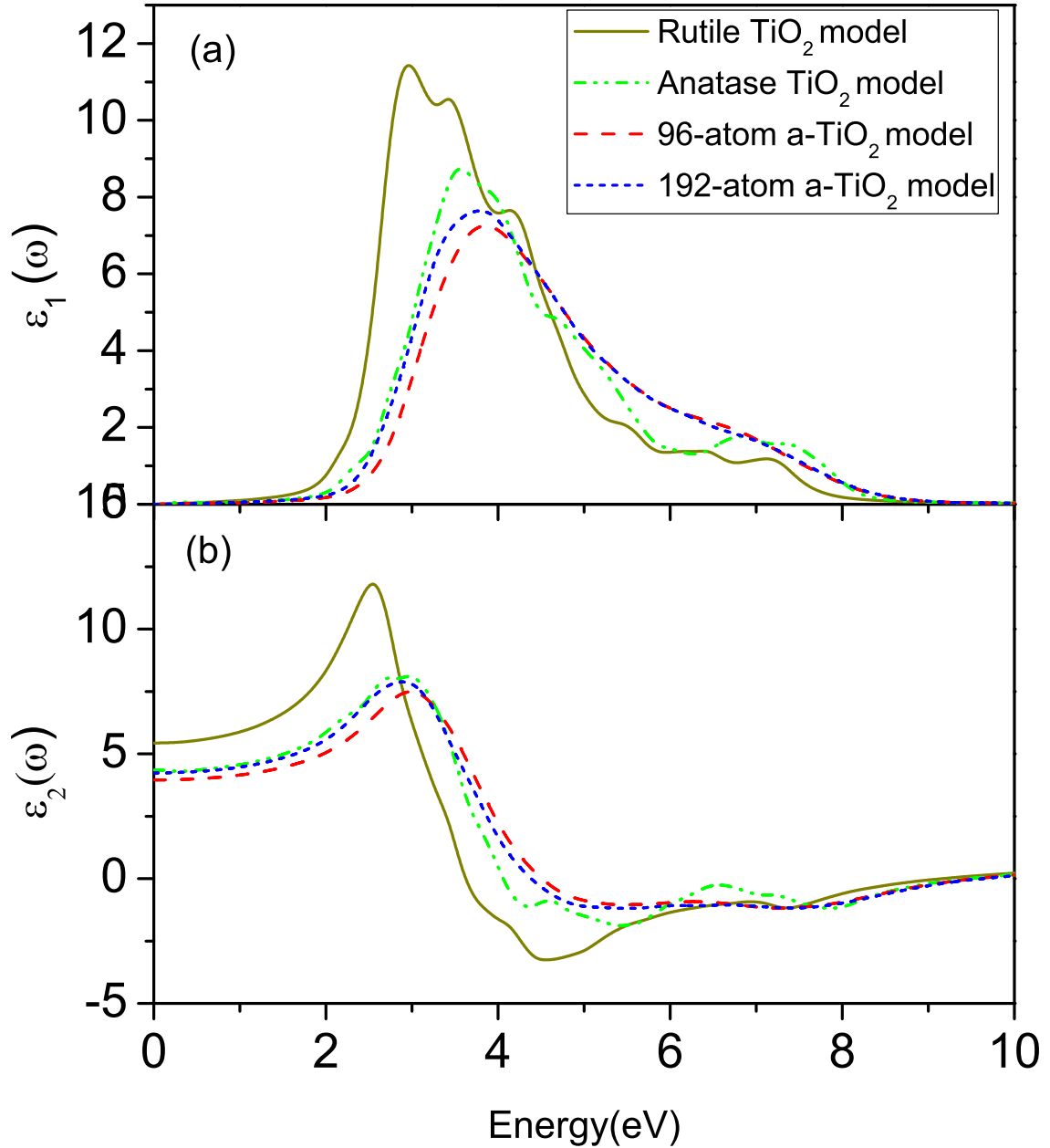
Figure 4.7: Calculated imaginary parts (a) and real parts (b)of the dielectric function of TiO$_2$ for Rutile, Anatase and amorphous structures.
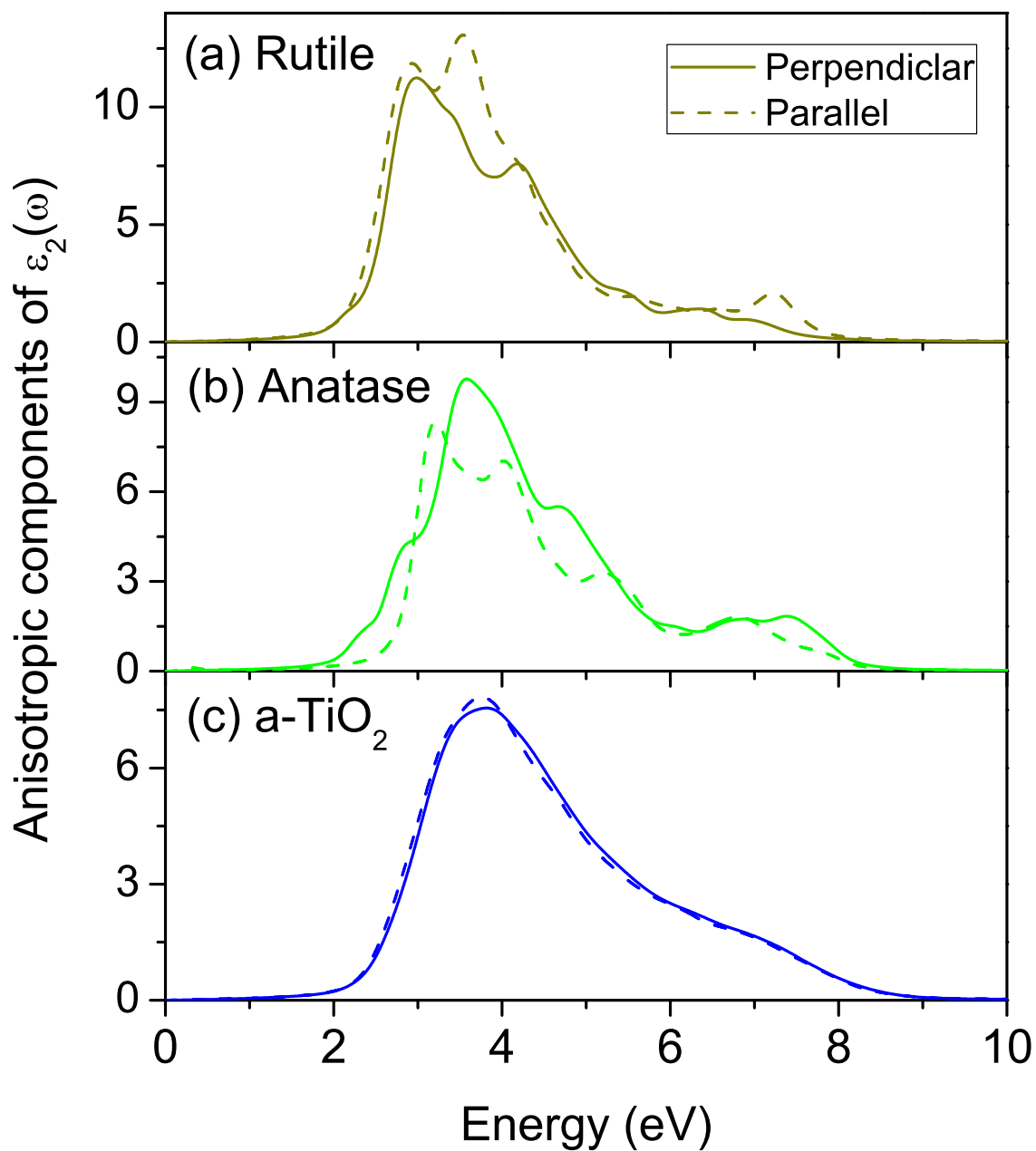
Figure 4.8: Anisotropic components of imaginary part of the dielectric function; (a) Rutile, (b) Anatase and (c) Amorphous structures. Perpendicular components(to c axis) are solid lines and parallel components are dashed lines.

4.4 Conclusion

We created different a-TiO$_2$ models (two with 96 atoms and one with 192 atoms) by using the 'melt-quench' method, and we were able to reproduce structural properties for a-TiO$_2$ as provided by experimental methods. Most of the Ti and O atoms tend to be six-fold and three-fold coordinated, respectively, showing the similar local structure to crystalline form TiO$_2$ (both in the anatase and rutile structures). In addition, the electronic sturctures of a-TiO$_2$ is similar to the crystalline elctronic sturctures in many respects, in fact much closer to the anatase TiO$_2$. The Γ-point band gaps of a-TiO$_2$ comparable to calculated results for bulk crystalline TiO$_2$ verifies the similarities. The IPR analysis showed that the tail states near the band edges are localized in a-TiO$_2$ in contrast to the crystalline TiO$_2$. The IPR analysis concluded that the valence tail states result from the positional disorder of O atoms, whereas, the conduction tail states result from over-coordinated Ti atoms. Furthermore, the optical properties of the a-TiO$_2$ resemble to those of anatase phase in many respects. The comparable structural, electronic and optical properties between a-TiO$_2$ and crystalline TiO$_2$ opens the possibility of a-TiO$_2$ being used as an alternative to crystalline TiO$_2$ and hence reducing the cost of processing. As seen from the Weaire-Thorpe theorem[66] in amorphous Si, the electronic structure of a-TiO$_2$ is determined by the short range order of the network. Since the local ordering is preserved within small distortions, the gross features of the electronic spectrum and dielectric functions are similar. All of this can be reformulated in terms of the decay of the density matrix in real space as discussed for example in Ref. [51].

5 AB INITIO SIMULATIONS OF SOLID ELECTROLYTE MATERIALS IN LIQUID AND GLASSY PHASES.

B. Prasai and D. A. Drabold

Ab initio simulation of solid electrolyte materials in liquid and glassy phases

Phy. Rev. B, **83**, 094202 (2011).

5.1 Introduction

Chalcogenide glasses have been studied extensively for the last few decades both for their basic scientific interest and because they are preferred materials for applications such as optical recording devices [3] and phase change memory[2]. There has been particular interest in Ge-Se glasses because of their excellent glass formation characteristics: the Ge_xSe_{1-x} binary system is an excellent glass former for x≤0.43 [11]. Ge-Se glasses when doped with metals like Ag become solid electrolytes offering high ionic conductivities. Such electrolytes are getting attention for their technological importance with the application in "conducting bridge" (flash) memory devices[1]. Since the properties of chalcogenide glasses accrue from their structure, the knowledge of the structure of these glasses is an essential precursor to unraveling their properties for further study.

The structure of GeSe glasses has been widely studied, and the basic structural units consist of Ge-Se tetrahedra and Se chains combined in various ways. X-ray[14] and neutron[15, 16] diffraction, and other experimental methods have been used to study the structure of Ge-Se-Ag glass. There have also been some computational studies to model the structure. Tafen et al.[18] reported two *ab-initio* models; $(GeSe_3)_{0.9}Ag_{0.1}$ and $(GeSe_3)_{0.85}Ag_{0.15}$ with short range order consistent with the experimental results. It has also been reported that Ag atoms prefer to sit at trapping center (TC) which is near the

midpoint of a line joining two host atoms (Ge or Se) separated by a distance between 4.7 and 5.2 Å with the bond length of Ag to the host atoms ranging 2.4-2.6 Å[67] for low Ag concentration.

The purpose of this study is to understand the structure of Ge-Se-Ag, Ge-Se-Cu and Ge-Se-Ag-Cu glasses and the ion dynamics for the single ion and the mixed ion cases. Section 5.2 of the paper briefly describes the method and the technical details of the simulations. Section 5.3 is organized into four distinct subsections with 5.3.1.1 devoted to the structure of the amorphous models and 5.3.1.2 to the structure of the liquid models. Electronic characteristics of both the amorphous and the liquid systems is presented in section 5.3.2 through the electronic density of states and the projected density of states. Section 5.3.3 is devoted to the dynamics of the ions at different temperatures 300K, 700K and 1000K. The character of the ion traps is described in section 5.3.4. Finally we present a brief summary in section 10.

5.2   Methods

We used the melt quenching method to generate the systems described in this work [51]. We constructed a cubic supercell, fixing the volume and the number to reproduce the experimental density according to the desired stoichiometry and with minimum acceptable distance between two atoms set to 2Å, starting with a random initial configuration. We generated each sample for four different models; $(GeSe_3)_{0.9}Ag_{0.1}$ with 27 Ge atoms, 81 Se atoms and 12 Ag atoms; $(GeSe_3)_{0.8}Ag_{0.2}$ with 24 Ge atoms, 72 Se atoms and 24 Ag atoms; $(GeSe_3)_{0.9}Cu_{0.1}$ with 27 Ge atoms, 81 Se atoms and 12 Cu atoms; $(GeSe_3)_{0.77}Cu_{0.03}Ag_{0.2}$ with 23 Ge atoms, 69 Se atoms, 4 Cu atoms and 24 Ag atoms. These models were annealed and equilibrated for 2.5 ps at 2000K, well above the melting points. The cells were then cooled to 1000K over 10ps and equilibrated at 1000K for 5ps. They were then cooled to 300K over 14 ps. Next these systems were equilibrated

at 300K for more than 50 ps. Finally these systems were fully relaxed. All of the calculations were carried out under the periodic boundary condition using Vienna *Ab-initio* Simulation Package(VASP)[45, 46], with Vanderbilt Ultra Soft pseudopotentials. VASP is based on density functional theory using a plane wave basis. We used the local density approximation (LDA) for the exchange correlation energy. These systems were annealed, equilibrated and cooled using molecular dynamic (MD) option of VASP and relaxation is carried out under conjugate gradient (CG) mode.

5.3 Result and Discussion

5.3.1 Structural properties

5.3.1.1 Structural properties of amorphous Ge-Se-Ag-Cu

Fig.9.2 shows the total radial distribution functions (RDFs) and structure factors for our four different models; g-$(GeSe_3)_{0.9}Ag_{0.1}$, g-$(GeSe_3)_{0.8}Ag_{0.2}$, g-$(GeSe_3)_{0.9}Cu_{0.1}$ and g-$(GeSe_3)_{0.77}Cu_{0.03}Ag_{0.2}$. The first peak of the RDF is the contribution from Ge-Se and Se-Se correlations whereas the second peak is due to Se-Se and Ge-Ag/Cu correlations (Fig.5.2 and Fig.5.3). There is not much variation in the short range order (SRO) i.e. nearest neighbor distance and second nearest neighbor distance for the different models. We observed a slight change in the nearest neighbor distance for the Ag rich model and Cu rich model. The average bond length and the mean coordination numbers are presented in Table 8.3. Table 5.2 gives the mean bond lengths for different bonds present in our models. We did not detect Ge-Ge bonds in any of our models as seen previously in g-$(GeSe_3)_{0.9}Ag_{0.1}$ [18]. We also observed that both Ag and Cu preferred to have Se as neighbor with only 16% of Cu/Ag bonded with Ge in our models. These results are very close to bond lengths measured by Piarristeguy et al. [14]. We have not seen any experiments for Cu-Ge-Se systems; however the Cu-Se correlation length we observed is not very far from the value (2.42 Å-2.44Å) measured by Merino et al. [68] for CuInSe$_2$.

Table 5.1: Short range order; nearest neighbor distance (NN), next nearest neighbor distance (NNN) and mean coordination number (CN).

	NN(Å)	NNN(Å)	CN
$(GeSe_3)_{0.9}Ag_{0.1}$	2.49	3.75	2.50
$(GeSe_3)_{0.8}Ag_{0.2}$	2.51	3.80	2.92
$(GeSe_3)_{0.77}Cu_{0.03}Ag_{0.2}$	2.45	3.80	2.9
$(GeSe_3)_{0.9}Cu_{0.1}$	2.40	3.83	2.8

We also obtained the silver and copper coordination number for each model. The coordination number 3.1 of silver at 20% is as predicted(3.0) by Mitkova et al. [69]. The coordination number 4.67 of copper at 10% is much higher than 2.16 of silver (found to be 2.0 by Tafen et al. [18]) for the same concentration. Topological information is presented in Table 5.3. We detected a few 3-fold Ge and 3 and 4 fold Se that we interpret as a structural defect in our models.

We also compared the static structure factors for our models(Fig.9.2). There is no significant change in the position of the first two peaks. We observed a weak peak in S(Q) slightly above 1 Å $^{-1}$. This peak, which is a precursor to the first sharp diffraction peak (FSDP), varies as a function of Ag concentration that the peak disappears as Ag concentration increases, also shown by Piarristeguy et al. [70]. We did not observe any particular correlation contributing to this peak as the partial structure factors(Fig.5.4) shows that the peak has contribution from all of the partials. We compared partial structure factors for $(GeSe_3)_{0.9}Ag_{0.1}$ and $(GeSe_3)_{0.9}Cu_{0.1}$ and observed the only differences in correlation of Ag-Ag and Cu-Cu as well as in Se-Ag/Cu.
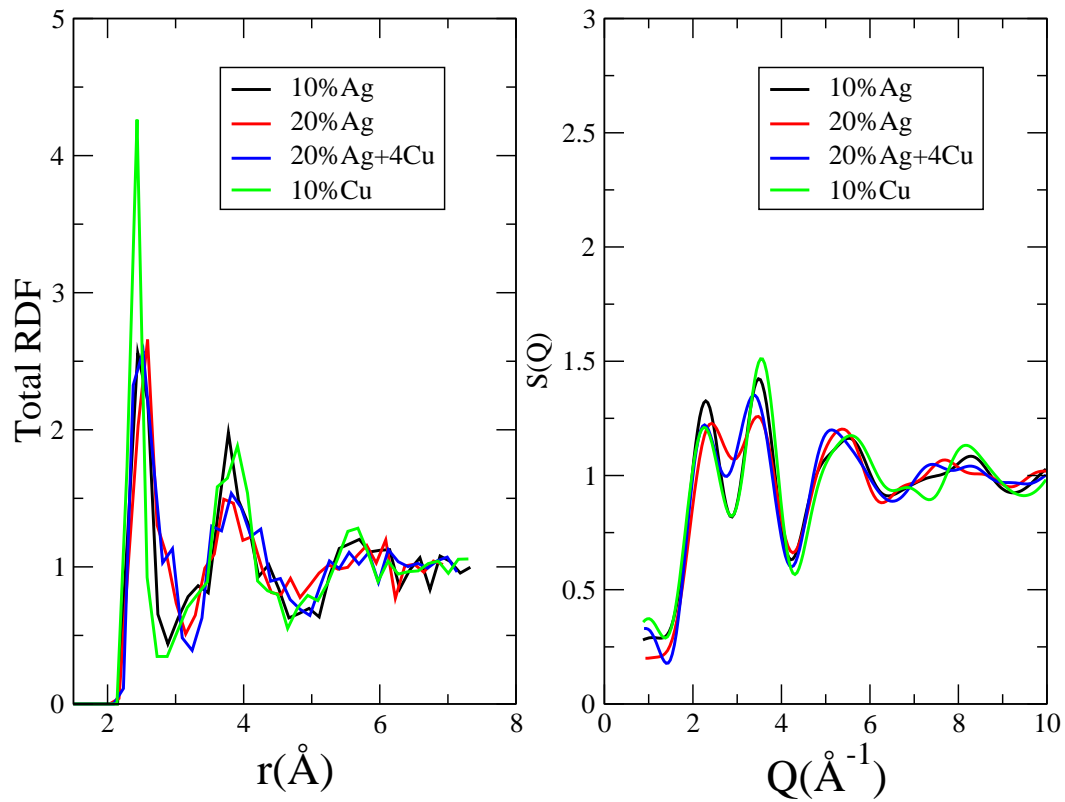
Figure 5.1: Comparison of total radial distribution functions and static structure factors for all amorphous models
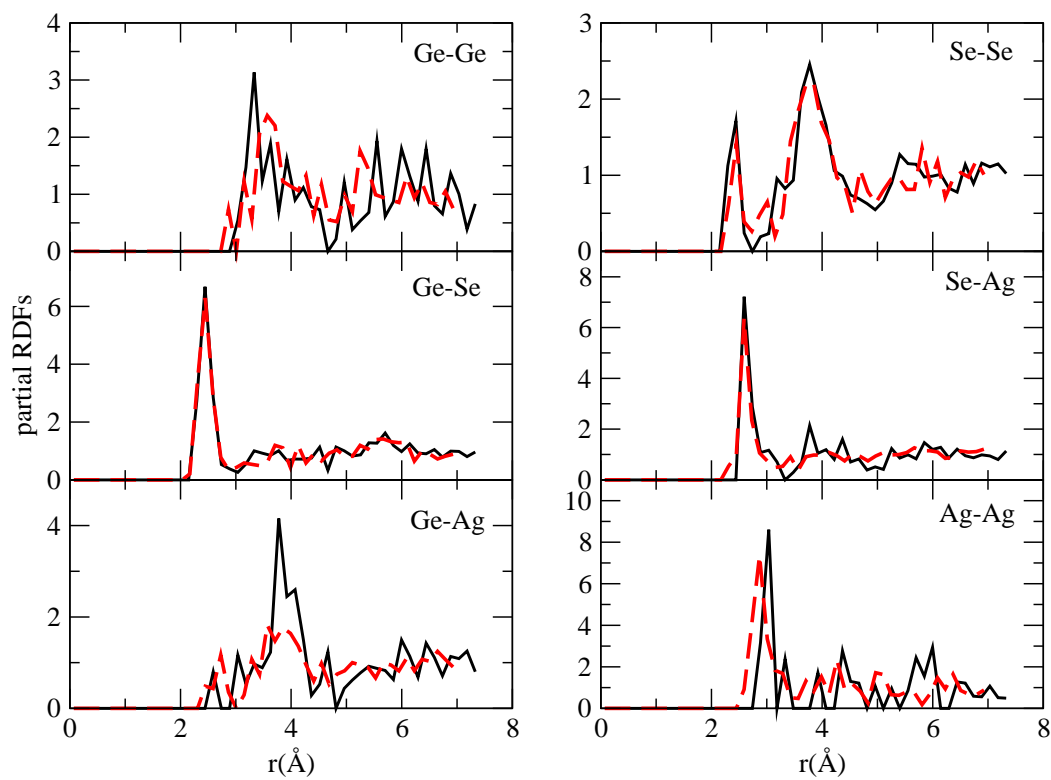
Figure 5.2: Partial radial distribution functions for amorphous $(GeSe_3)_{0.9}Ag_{0.1}$ (black) and $(GeSe_3)_{0.8}Ag_{0.2}$ (red/dashed line)
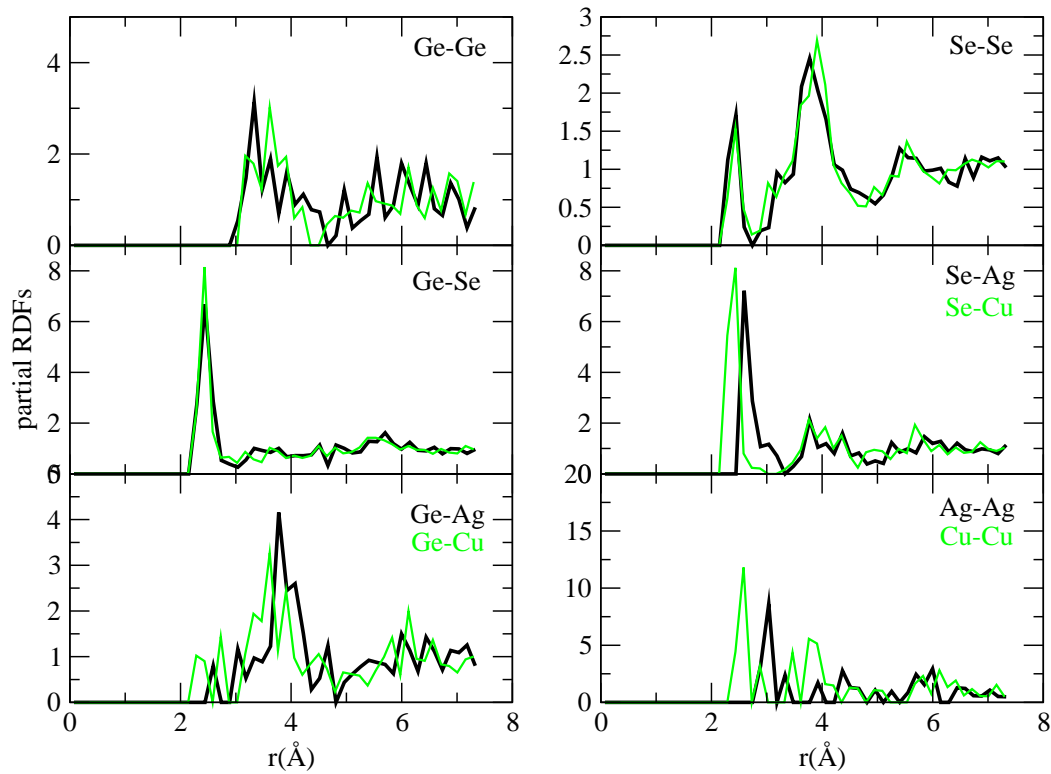
Figure 5.3: Partial radial distribution functions for amorphous $(GeSe_3)_{0.9}Ag_{0.1}$ (black) and $(GeSe_3)_{0.9}Cu_{0.1}$ (green/thin line)
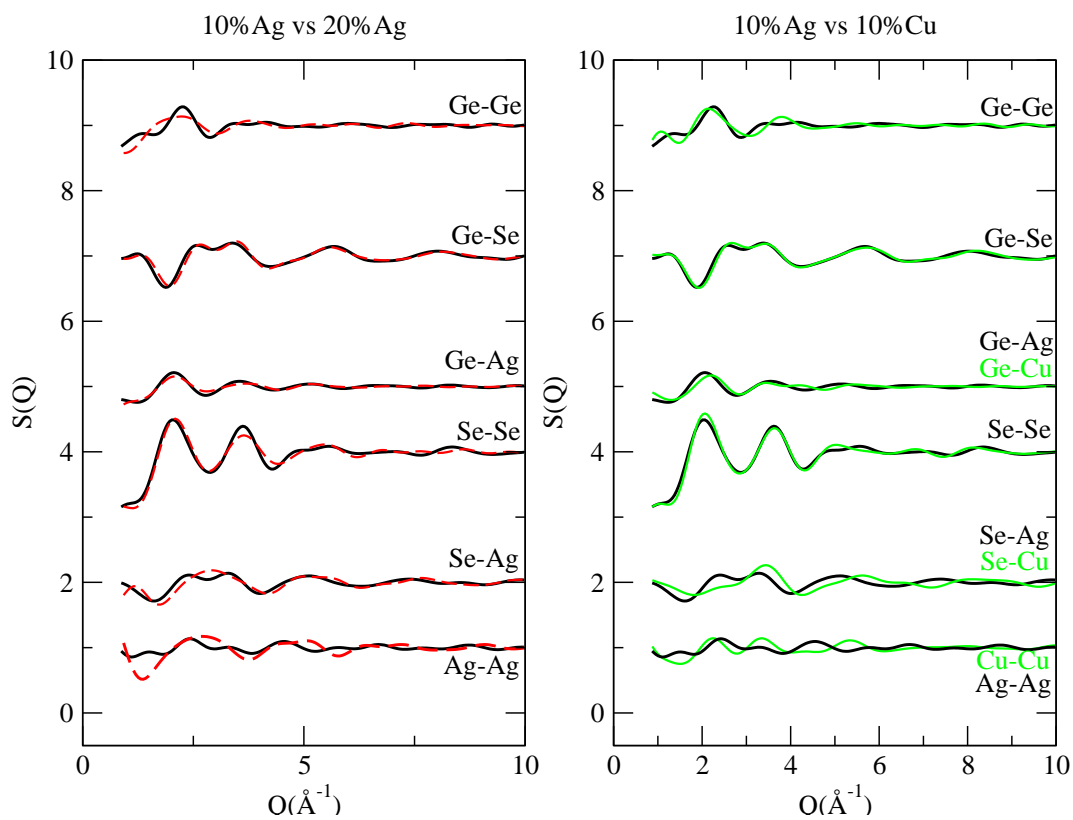
Figure 5.4: Partial structure factors of amorphous $(GeSe_3)_{0.9}Ag_{0.1}$ (black) ,$(GeSe_3)_{0.8}Ag_{0.2}$ -(red/dashed) and $(GeSe_3)_{0.9}Cu_{0.1}$ (green/thin).

Table 5.2: Mean nearest neighbor bond lengths(Å) in $(GeSe_3)_{0.9}Ag_{0.1}$ (I), $(GeSe_3)_{0.8}Ag_{0.2}$ (II), $(GeSe_3)_{0.9}Cu_{0.1}$ (III) and $(GeSe_3)_{0.77}Cu_{0.03}Ag_{0.2}$ (IV) glasses.

	I	II	III	IV	Expt.[70]
Ge-Se	2.37	2.37	2.35	2.37	2.37
Se-Se	2.39	2.40	2.41	2.40	2.37
Ge-Ag	2.55	2.60	2.60	–	–
Se-Ag	2.66	2.66	2.64	–	2.67
Ag-Ag	3.00	2.88	2.95	–	3.05
Ge-Cu	–	–	2.34	2.35	–
Se-Cu	–	–	2.34	2.34	–
Ag-Cu	–	–	2.77	–	–
Cu-Cu	–	–	–	2.54	–

Table 5.3: Coordination statistics for $(GeSe_3)_{0.9}Ag_{0.1}$, $(GeSe_3)_{0.8}Ag_{0.2}$, $(GeSe_3)_{0.9}Cu_{0.1}$, and $(GeSe_3)_{0.77}Cu_{0.03}Ag_{0.2}$ glasses. (in %)

	Ge	Ge	Se	Se	Se	Ag	Ag	Ag
	3-fold	4-fold	2-fold	3-fold	4-fold	2-fold	3-fold	4-fold
$(GeSe_3)_{0.9}Ag_{0.1}$	25.9	55.6	67.9	29.6	-	66.7	25.0	-
$(GeSe_3)_{0.8}Ag_{0.2}$	25.0	75.0	45.8	33.3	15.3	20.8	50.0	29.2
$(GeSe_3)_{0.77}Cu_{0.03}Ag_{0.2}$	8.7	73.9	39.1	39.1	11.6	12.5	66.7	20.8
$(GeSe_3)_{0.9}Cu_{0.1}$	18.5	70.5	63.0	27.2	3.7	-	-	-

	Cu				
	2-fold	3-fold	4-fold	5-fold	6-fold
$(GeSe_3)_{0.77}Cu_{0.03}Ag_{0.2}$	25.0	25.0	50.0	-	-
$(GeSe_3)_{0.9}Cu_{0.1}$	-	-	41.7	50.0	8.3

5.3.1.2 Structural properties of liquid Ge-Se-Ag-Cu

We performed thermal MD simulation of our models at 1000K for 25ps in order to obtain well equilibrated liquid systems. We calculated the radial distribution function (RDF) and present it in Fig.5.5. The RDFs are averaged over the last 2.5 ps. Figure 5.4 shows the dependence of peak position on the concentration of Ag/Cu with 2.45 Å for $(GeSe_3)_{0.9}Cu_{0.1}$, 2.48 Å for $(GeSe_3)_{0.9}Ag_{0.1}$ and 2.53 Å for $(GeSe_3)_{0.8}Ag_{0.2}$ and $(GeSe_3)_{0.77}Cu_{0.03}Ag_{0.2}$. We also present partial radial distribution functions in Fig.5.6 showing Ge-Ge, Ge-Se, Se-Se and Se-Ag/Cu correlations. All of our models except $(GeSe_3)_{0.9}Ag_{0.1}$ (2.6Å) confirm the presence of Ge-Ge homopolar bonds with peak position at 2.71 Å in contrast with the glass. We also observed Se-Se and Ge-Se bond distances of 2.47Å and 2.50 Å respectively. We observe no concentration dependence on the first peak position of Ge-Se,Se-Se and Se-Ag/Cu correlations. The major contribution to the first peak of the total RDF is from Ge-Se,Se-Se and Se-Ag/Cu correlations with Se-Ag/Cu correlation causing the shifts on the first peak positions. The second peak of the total RDF is mainly due to Se-Se correlation. We measured the first peak positions of $g_{\alpha\beta}(r)$ and present these in Table 5.4.
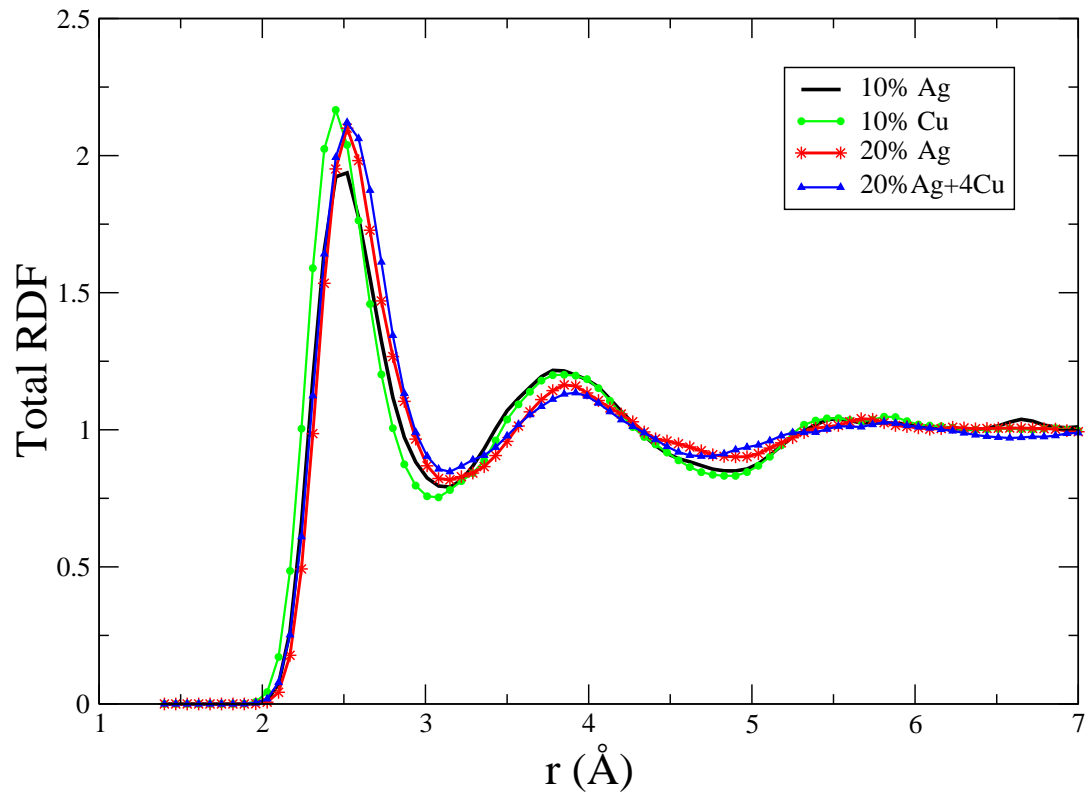
Figure 5.5: Comparison of total radial distribution functions for all liquid models at 1000K
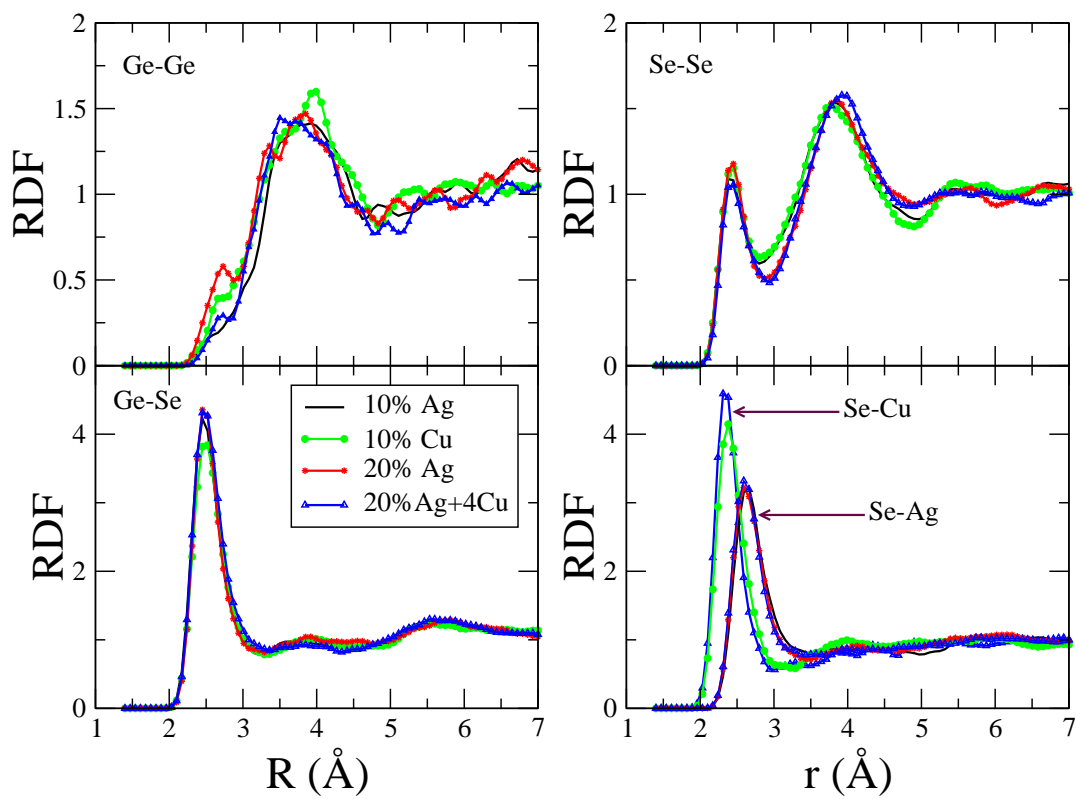
Figure 5.6: Comparison of partial radial distribution functions for all liquid models at 1000K

Table 5.4: Mean nearest neighbor bond lengths(Å) in $(GeSe_3)_{0.9}Ag_{0.1}$, $(GeSe_3)_{0.8}Ag_{0.2}$, $-(GeSe_3)_{0.9}Cu_{0.1}$, and $(GeSe_3)_{0.77}Cu_{0.03}Ag_{0.2}$ liquids at 1000K.

	Ge-Ge	Ge-Se	Se-Se	Ge-Ag	Se-Ag	Ag-Ag	Ge-Cu	Se-Cu	Ag-Cu	Cu-Cu
$(GeSe_3)_{0.9}Ag_{0.1}$	2.6	2.50	2.47	3.0	2.60	2.9				
$(GeSe_3)_{0.8}Ag_{0.2}$	2.71	2.50	2.47	2.7	2.60	2.9				
$(GeSe_3)_{0.77}Cu_{0.03}Ag_{0.2}$	2.71	2.50	2.47	2.7	2.60	2.9	2.46	2.31	2.80	2.67
$(GeSe_3)_{0.9}Cu_{0.1}$	2.71	2.50	2.47	..	..	..	2.40	2.35	..	2.60

5.3.2 Electronic Properties

5.3.2.1 Electronic properties of amorphous Ge-Se-Ag-Cu

We analyzed the electronic structure of our models through electronic density of states (EDOS). Fig.5.7-5.8 shows the EDOS and the projected density of states (PDOS) for the different models. The figures show both the species projected DOS and orbital projected DOS for our systems. The fermi level has been shifted to 0 in all cases. From our observation, it can be seen that the basic spectra for our systems look similar to the EDOS of GeSe binary systems [71]. For Ag doped $GeSe_3$, the first two bands are dominated by 4s-like state of Se and Ge. The third band consists mainly of p-like states of Se and d-like states of Ag and partly s-like states of Ge. The fourth band i.e., the lowest conduction band, contains p-like states of Se and partly s-like states of Ge and d-like states of Ag. The spectrum with the Cu doped $GeSe_3$ is also similar to Ag doped system with Cu contribution mostly to the third band with its d-like states at about -2.5 eV. From our simulation we found that the Γ point optical gap closes as we proceed from Ag rich to Cu rich. The narrowing of the gap with the addition of Cu is as predicted by Simdyankin et al.[72] and Aniya et al.[73], who showed that for the low concentration of Cu the gap closes with the addition of Cu in AsS and AsSe glasses.

To understand the spatial structure of electron states, we visualize the charge density associated with the eigenstates near the fermi level. We chose the highest state of the valance band and the lowest state of the conduction band and present the charge density associated with these states in Fig. 5.11 and Fig. 5.12 respectively. Fig.5.12 illustrates a somewhat localized state where the charge is primarily on a small cluster of atoms, whereas Fig.5.11 illustrates a less localized state or the linear combination of nearly localized states where the charge is distributed to a big cluster. It should be stated that these states are not fully localized in an Anderson sense, but are strongly spatially
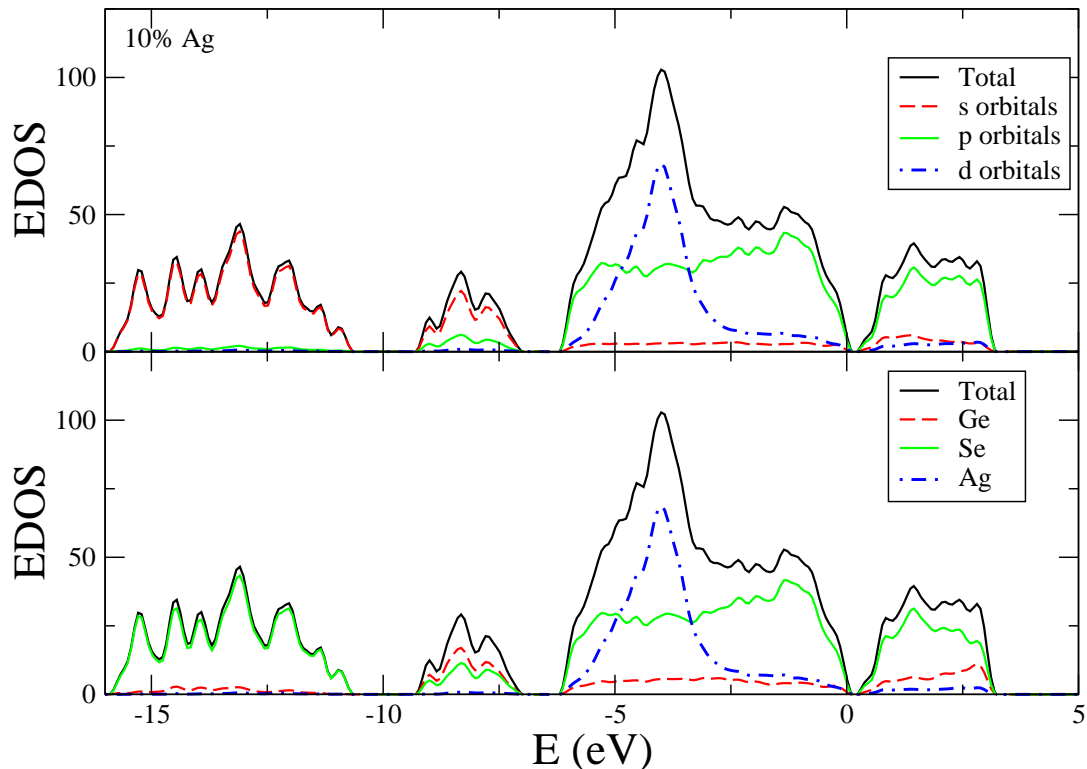
Figure 5.7: Electronic density of states for amorphous $(GeSe_3)_{0.9}Ag_{0.1}$.

non-uniform near the band edge[51]. Furthermore these figures clearly illustrate the dominance of p-like Se states and d-like Ag states on the valance tail and p-like Se states on the conduction tail.

We also analyzed the contribution of each species to the total EDOS near the gap region. Ge does not contribute to the EDOS near the fermi level in any of our models. But when we look at the contribution of Se we see substantial changes in our models near the gap region. To understand this we analyzed the Se EDOS as a function of its coordination number but we didn't observe any correlations. However when we analyzed Se EDOS for Se bonded with Cu or Ag and Se not bonded with Cu or Ag we observed some differences as shown in Fig.5.13. Independent of the coordination number, Se bonded with Ag opens
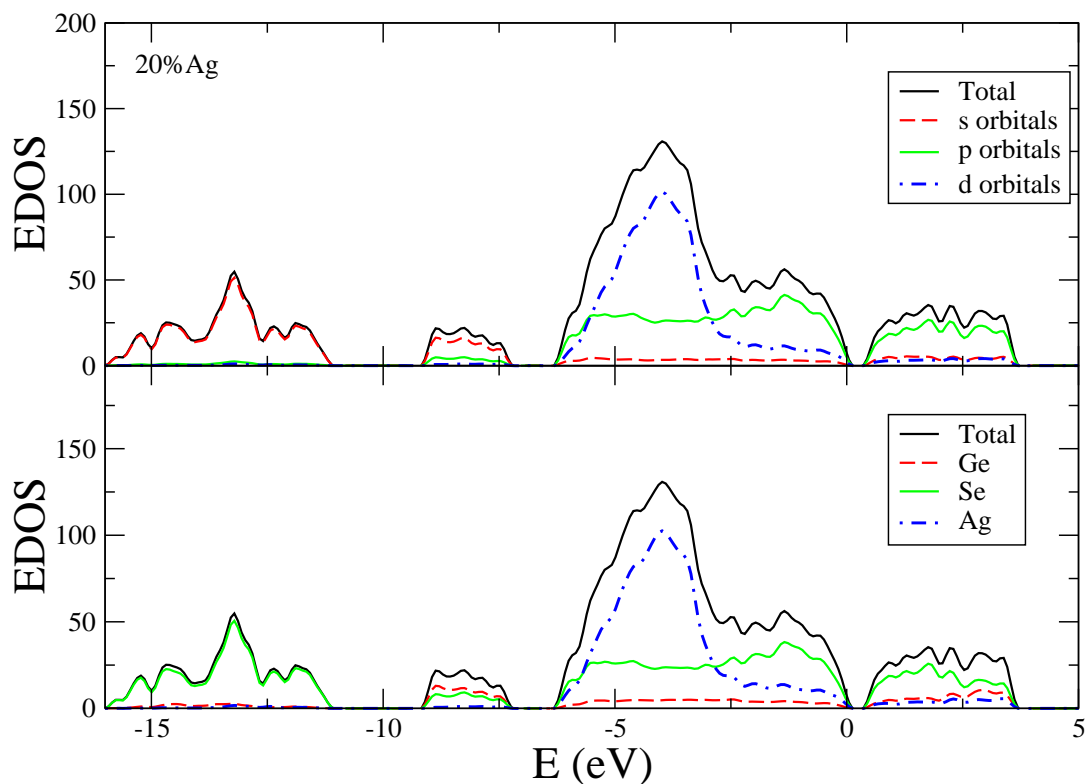
Figure 5.8: Electronic density of states for amorphous $(GeSe_3)_{0.8}Ag_{0.2}$.

the gap whereas Se bonded with Cu closes the gap. Cu also has contribution to the total EDOS in the gap region however it is lower than that of Se in that region.

5.3.2.2 Electronic properties of Liquid Ge-Se-Ag-Cu

In order to explore electronic properties of the liquid systems we calculated the electronic density of states at 1000K. We observed qualitatively similar pictures for the EDOS for all the models. To illustrate, we present EDOS of liquid $(GeSe_3)_{0.8}Ag_{0.2}$ along with amorphous $(GeSe_3)_{0.8}Ag_{0.2}$ in Fig.5.14. Relative to the glass, we observed almost no change in valence band in contrast to the conduction band that has been shifted towards the valance band filling the gap completely. The presence of a few homopolar Ge-Ge
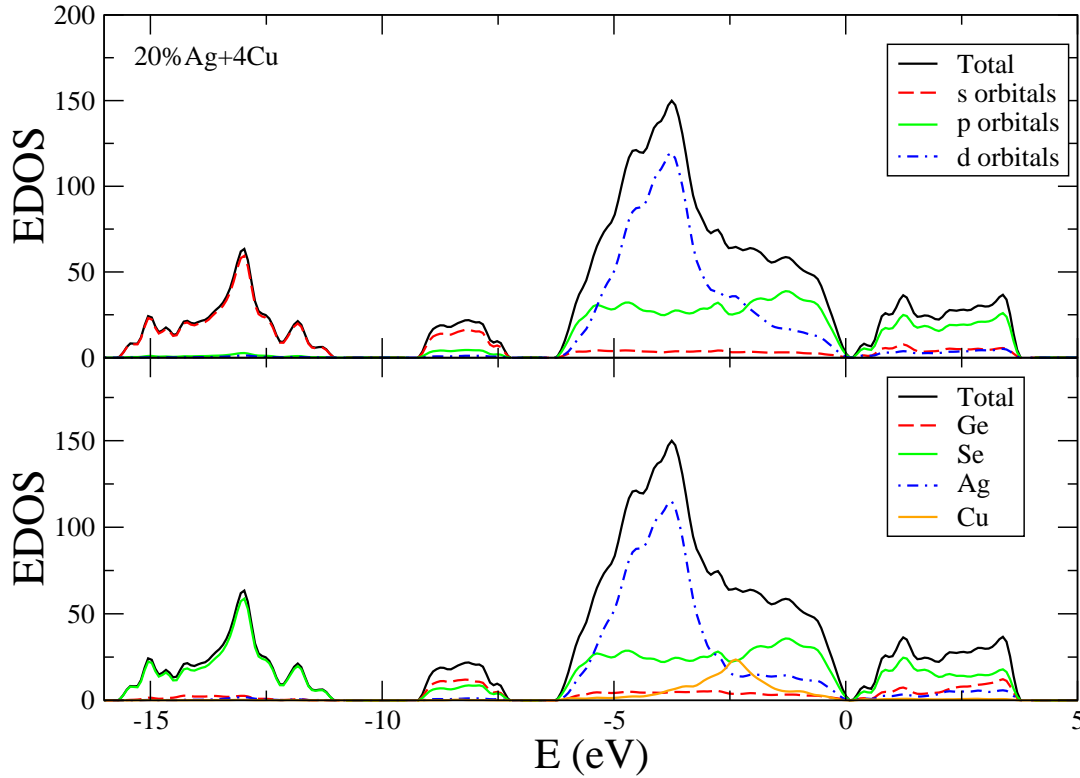
Figure 5.9: Electronic density of states for amorphous $(GeSe_3)_{0.77}Cu_{0.03}Ag_{0.2}$.

bonds, 2-fold Ge(25%),1-fold Se(18%) and 1-fold Ag(13%) as compared to non of these observed in amorphous $(GeSe_3)_{0.8}Ag_{0.2}$ is also noted.

5.3.3 Ion dynamics

We studied the dynamics of Ag and Cu ions in the $GeSe_3$ host by computing the mean square displacement (MSD) for each atomic constituent as:

$$\langle r^2(t) \rangle_a = \frac{1}{N_a} \sum_{i=1}^{N_a} \langle |\vec{r_i}(t) - \vec{r_i}(0)|^2 \rangle \tag{5.1}$$

where the quantity in $\langle \rangle$ is the calculated statistical average over the particular atomic species α. We carried out constant temperature molecular dynamic(MD) calculations at three different temperatures 300K, 700K and 1000K in order to study ion dynamics in our the amorphous as well as the liquid systems.
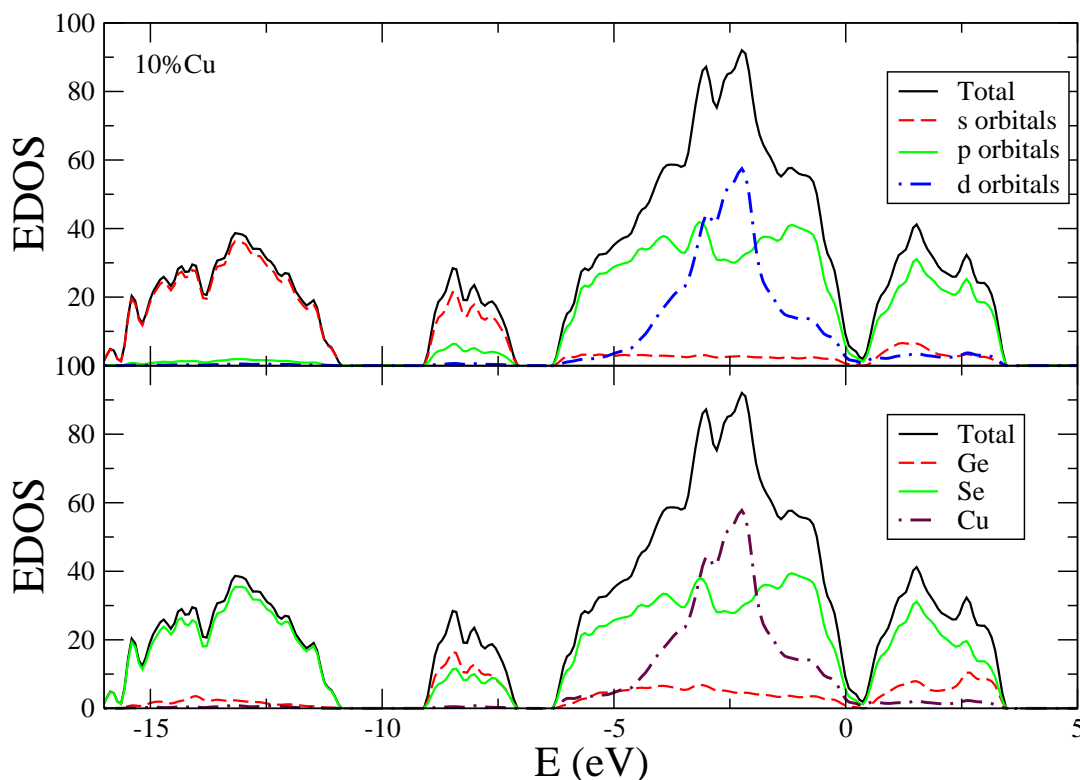
Figure 5.10: Electronic density of states for amorphous $(GeSe_3)_{0.9}Cu_{0.1}$.

5.3.3.1 Amorphous Ge-Se-Cu-Ag

As expected, at 300K none of the ions showed substantial diffusion. In order to illustrate the diffusion we chose T=700K and present the MSD for each species for each system calculated at this temperature in Fig.5.15. At 700K Ag ions show significant diffusion consistent with the previous result[18] in contrast to Cu ions that do not diffuse as much. To elucidate the diffusion of these ions we examine the trajectories for 20ps. Fig.5.16 and 5.17 show two dimensional projections of the trajectories of the most and the least diffusive ions in $(GeSe_3)_{0.9}Ag_{0.1}$ and $(GeSe_3)_{0.9}Cu_{0.1}$. The trajectories illustrate the wide range of diffusion for the ions with displacement ranging 1Å-3.87Å in $(GeSe_3)_{0.9}Ag_{0.1}$, 2Å-6.71Å in $(GeSe_3)_{0.8}Ag_{0.2}$ and 1Å-3.74Å in $(GeSe_3)_{0.9}Cu_{0.1}$. For the mixed-ion model $(GeSe_3)_{0.77}Cu_{0.03}Ag_{0.2}$ this displacement ranges between 1.73Å-2.82Å
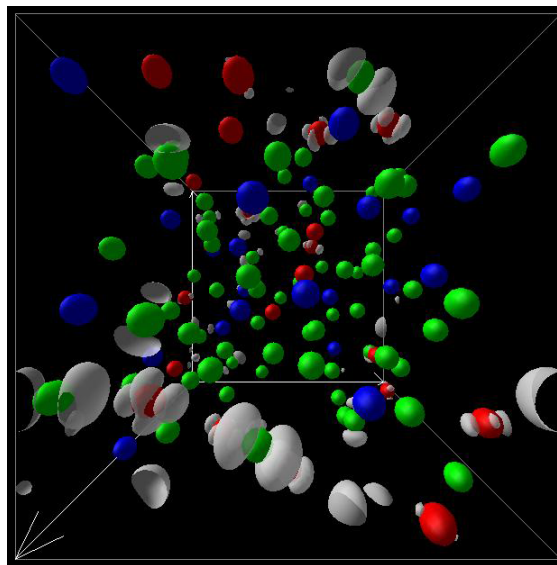
Figure 5.11:   Charge density of the highest state of valance band in amorphous $(GeSe_3)_{0.8}Ag_{0.2}$. The blue, green and red spheres are respectively Ge, Se and Ag atoms, and white clouds around the atoms are charge density.
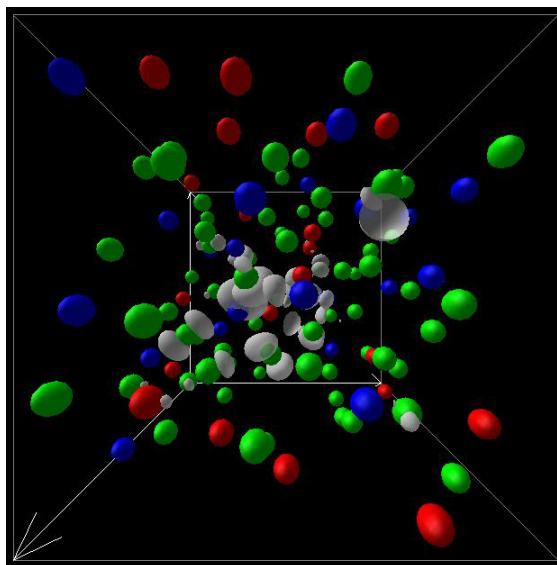
Figure 5.12:   Charge density of the lowest state of conduction band in amorphous $(GeSe_3)_{0.8}Ag_{0.2}$. The blue, green and red spheres are respectively Ge, Se and Ag atoms, and white clouds around the atoms are charge density.
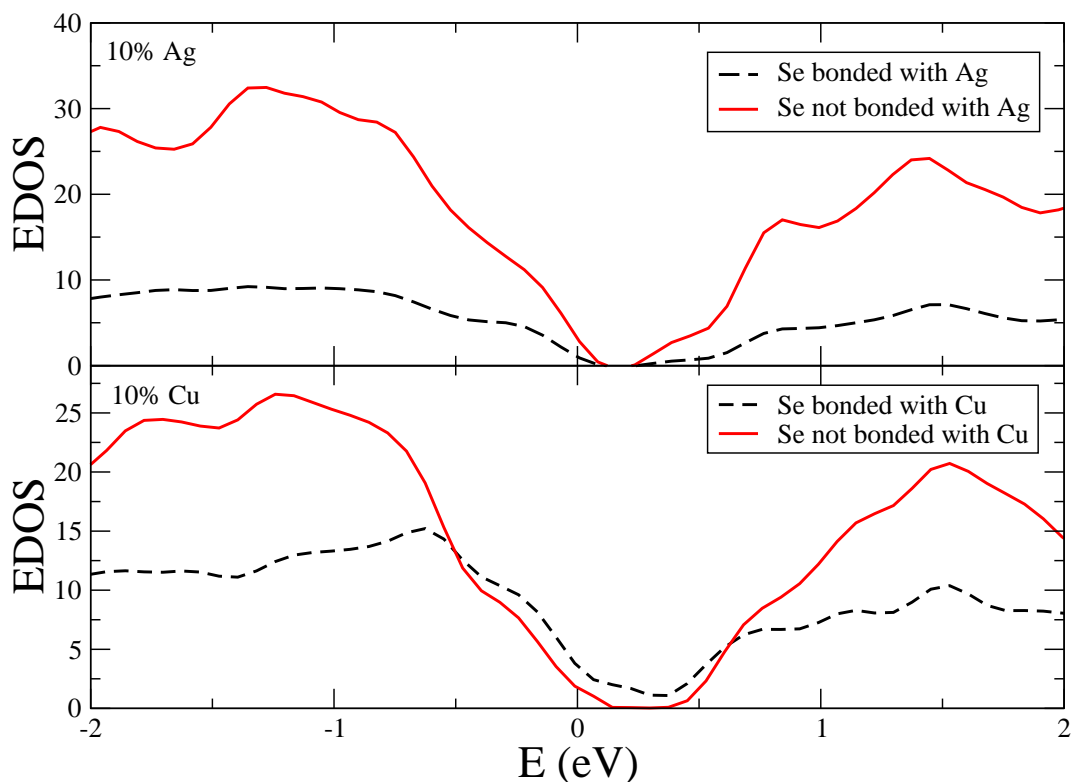
Figure 5.13:   Comparison of Se projected electronic density of states between Se bonded with Ag/Cu and Se not bonded with Ag/Cu in amorphous $(GeSe_3)_{0.9}Ag_{0.1}$ and $(GeSe_3)_{0.9}Cu_{0.1}$.

for Cu and 1.41Å - 8.06Å for Ag. For Ag rich models more than 60% of the ions have displacements greater than the average displacement (2.36Å in $(GeSe_3)_{0.9}Ag_{0.1}$ and 4.47Å in $(GeSe_3)_{0.8}Ag_{0.2}$) whereas for Cu, the majority has displacement smaller than the average(2.11Å). The wide range of diffusion can be attributed to variation in the local environment of the ions. To illustrate this we calculated the local densities of the most and the least mobile ions. We employed a sphere of radius 5.0Å around the ion and calculated the mean density of atoms inside the sphere. We observed that the most diffusive ion is located in the region with lower local density. In other words the most mobile ions have the wider variation of the local density as compared to that of the least mobile ion. Fig.5.18 shows one such comparison.
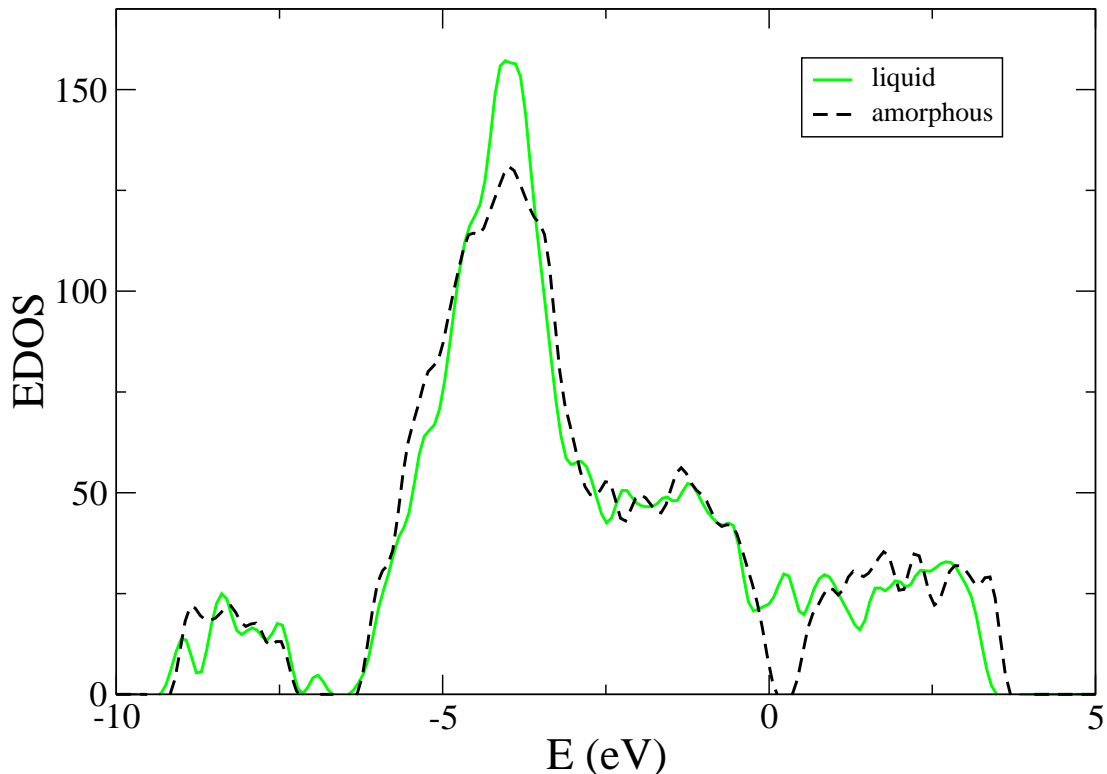
Figure 5.14: Electronic density of states for liquid $(GeSe_3)_{0.8}Ag_{0.2}$ (green/solid line) and amorphous (black/dashed line) $(GeSe_3)_{0.8}Ag_{0.2}$. Fermi level shifted to 0 eV

5.3.3.2 Liquid Ge-Se-Cu-Ag

One of the main properties of a liquid is the high diffusivity of atoms in the system. To illustrate this, we calculated the mean square displacements for each species at 1000K in all of our models. The diffusion plots as presented in Fig.5.19 shows that the MSD of each species increases rapidly as compared to that at 700K. We observe Ag diffusion still significantly larger than the host particles however; Ge and Se atoms are also diffusing rapidly. As before Cu still does not show high diffusion as Ag does compared to the host atoms.

Based on the plots we calculated diffusion coefficients using Einstein relation[10]. The time scale of about 20ps for our simulation was adequate to equilibrate the systems.
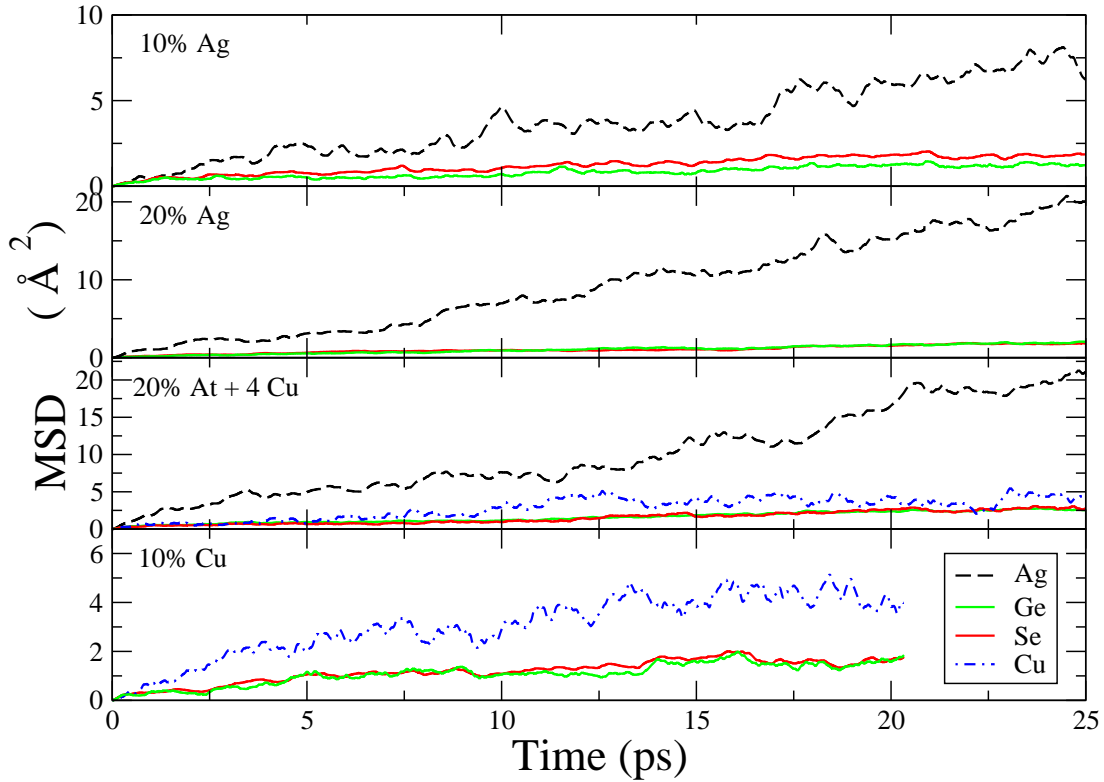
Figure 5.15:   Mean square displacement of atoms in amorphous $(GeSe_3)_{0.9}Ag_{0.1}$, $(GeSe_3)_{0.8}Ag_{0.2}$, $(GeSe_3)_{0.77}Cu_{0.03}Ag_{0.2}$ and $(GeSe_3)_{0.9}Cu_{0.1}$ (top to bottom respectively) glasses at T=700K. Ag(black) Ge(green), Se(red) and Cu(blue)

The Einstein relation for self-diffusion is given by:

$$\langle|\vec{r}_i(t) - \vec{r}_i(0)|^2\rangle = 6Dt + C \tag{5.2}$$

where C is a constant and D is the self-diffusion coefficient. The conductivity can be

calculated from the equation

$$\sigma = \frac{ne^2D}{k_BT} \tag{5.3}$$

where n is the number density of ions. The temperature dependence of the diffusion is

shown in Fig.5.20 and the values of diffusion coefficients and conductivities at different

temperatures are presented in Table 5.5. We did not find experimental results for the
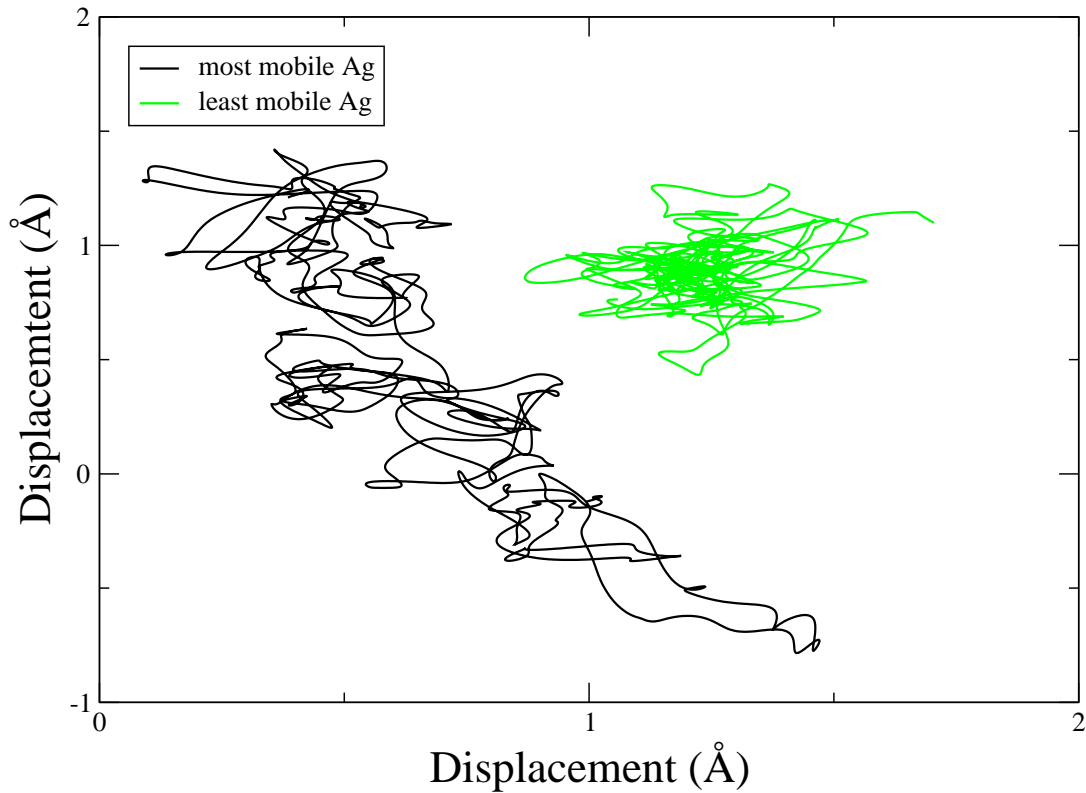
Figure 5.16: Trajectories of the most and the least diffusive Ag ions at 700K as a function of time in amorphous $(GeSe_3)_{0.9}Ag_{0.1}$.

conductivity of Cu ions; however Ag conductivity is close to ones reported by Urena et al.[74].

5.3.4 Trap centers and hopping of ions

To illustrate the different ionic transport properties of Ag and Cu, it is essential to study the local environment of Ag and Cu in our models. Fig.5.21 shows the local environment for Ag and Cu in $(GeSe_3)_{0.9}Ag_{0.1}$ and $(GeSe_3)_{0.9}Cu_{0.1}$ respectively. In the relaxed networks, most of the Ag ions(58.3%) are found to occupy the trap centers, between two of the host sites as also predicted by the previous workers [18, 67] but this is not the same case with Cu. Cu is always surrounded by more than two host atoms that makes the traps for Cu more rigid than for Ag. In Ag rich systems at 300K, we observed

Table 5.5: Self diffusion coefficient D and conductivity σ at 300K, 700K and 1000K for $(GeSe_3)_{0.9}Ag_{0.1}$ (10%Ag), $(GeSe_3)_{0.8}Ag_{0.2}$ (20%Ag), $(GeSe_3)_{0.9}Cu_{0.1}$ (10%Cu) and $(GeSe_3)_{0.77}Cu_{0.03}Ag_{0.2}$ (0.77%Cu)

	T(K)	D(cm^2/s)	σ(Scm^{-1})	
			This work	Expt.[74]
10%Ag	300K	1.15×10^{-9}	2.63×10^{-5}	1.3×10^{-5}
	700K	4.53×10^{-6}	0.0444	0.0207
	1000K	1.23×10^{-5}	0.0845	0.0898
20%	300K	1.16×10^{-8}	5.3×10^{-4}	7.5×10^{-5}
	700K	1.20×10^{-5}	0.235	0.0657
	1000K	2.53×10^{-5}	0.347	0.2584
10%Cu	300K	7.3×10^{-10}	1.67×10^{-5}	
	700K	3.3×10^{-6}	0.0323	
	1000K	1.13×10^{-5}	0.0775	
0.77%Cu	300K	$D_{Ag}=1.06\times10^{-8}$	4.85×10^{-4}	
		$D_{Cu}=7.16\times10^{-9}$	1.63×10^{-5}	
	700K	$D_{Ag}=1.30\times10^{-5}$	0.254	
		$D_{Cu}=1.16\times10^{-6}$	0.0038	
	1000K	$D_{Ag}=2.42\times10^{-5}$	0.332	
		$D_{Cu}=5.24\times10^{-6}$	0.012	
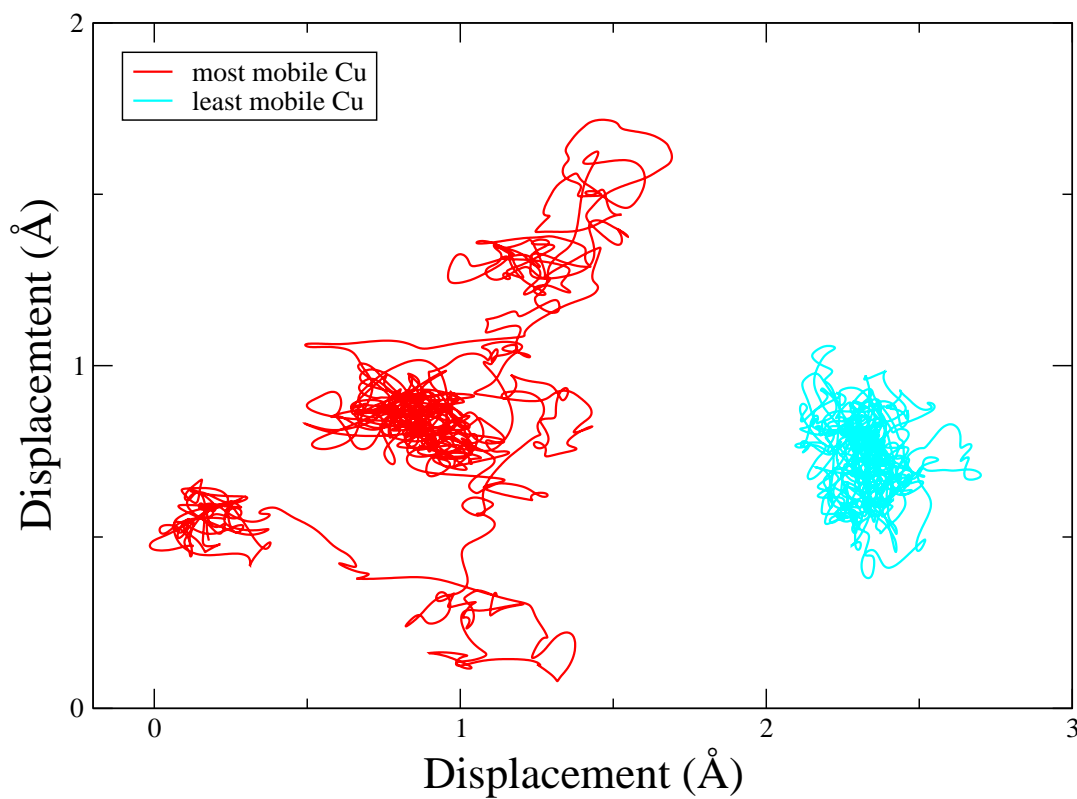
Figure 5.17: Trajectories of the most and the least diffusive Cu ions at 700K as a function of time in amorphous $(GeSe_3)_{0.9}Cu_{0.1}$.

that Ag is basically trapped with only a few hopping events. At 700K the lifetime of the trap decreases and hopping occurs. We observed the life time of the traps varying from 1ps - 3.5ps. However at 1000K we failed to observe the well defined hopping events because of the high the diffusion of the host itself. In the Cu rich system the story is completely different. Even at 700K we could observe only a few hopping events with much larger trap life time. It has also been shown by previous workers that the nature of trap or cage depends mainly on coordination number, nearest neighboring distance and angular distribution of the nearest neighbors[75]. The low coordination number of Ag makes it easy to escape the trap whereas for Cu, high coordination number, smaller
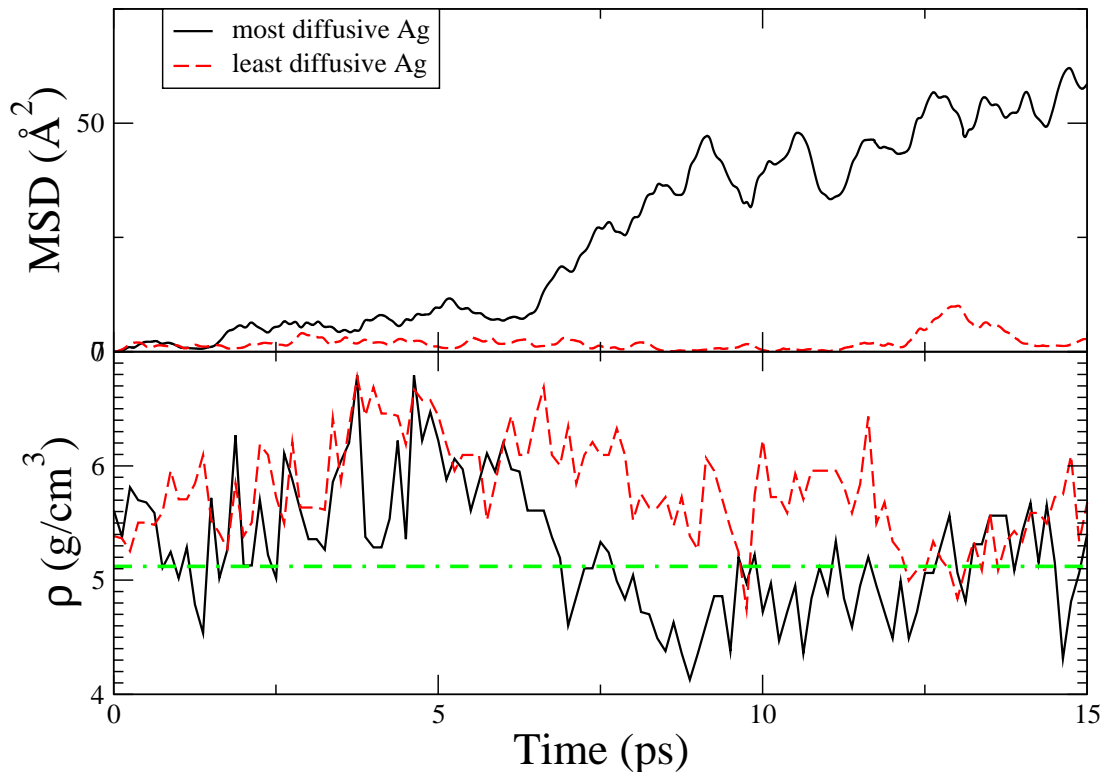
Figure 5.18: Local density of the most and the least diffusive Ag ions at 700K as a function of time in amorphous $(GeSe_3)_{0.8}Ag_{0.2}$.

neighbor distance and uniform angular distribution like tetrahedral network makes it very hard to escape from the trap.

5.4 Conclusion

We prepared different Ag and Cu doped $GeSe_3$ glass and liquid models by *ab initio* simulation using the 'melt-quench' method and analyzed their structural and electronic properties. We also simulated dynamics of Ag and Cu ions using molecular dynamics. We were able to reproduce structural data as provided by X-ray diffraction. From the electronic density of state we observed that the increase in Ag concentration widens the optical gap whereas increase in Cu concentration narrows the gap. We were also able to see the metallic behavior for the liquid systems with the gap closing completely at 1000K.
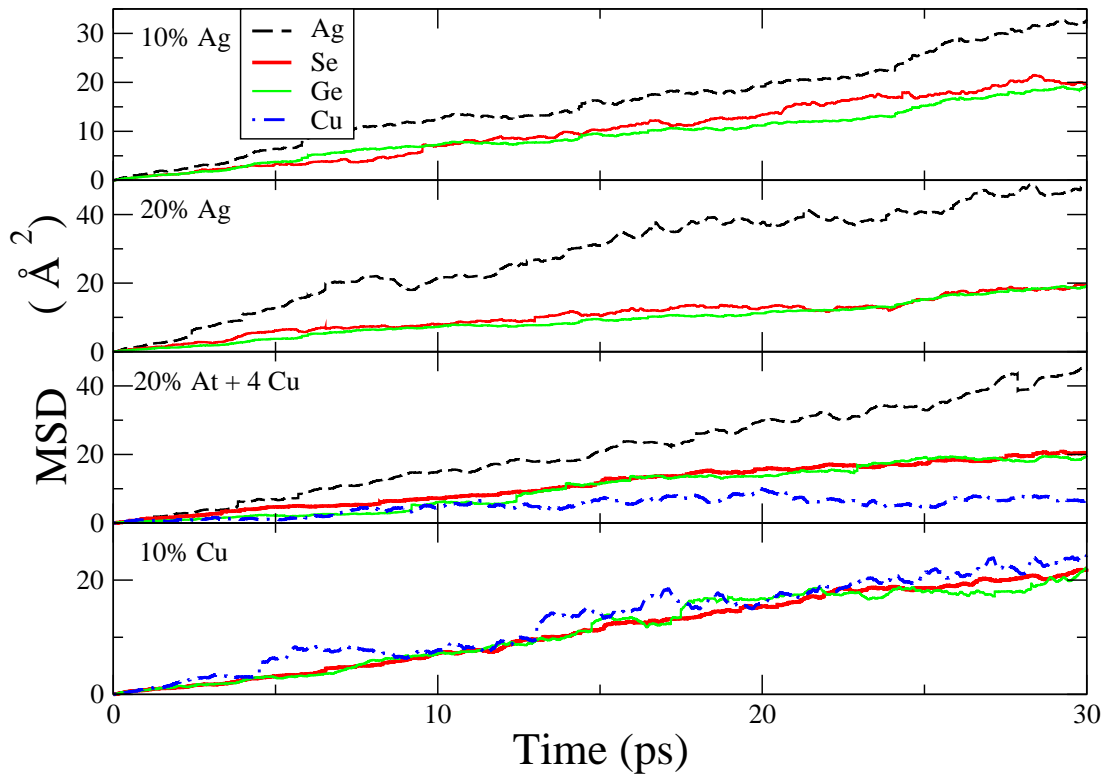
Figure 5.19:   Mean square displacement of atoms in liquid $(GeSe_3)_{0.9}Ag_{0.1}$, $(GeSe_3)_{0.8}Ag_{0.2}$, $(GeSe_3)_{0.77}Cu_{0.03}Ag_{0.2}$ and $(GeSe_3)_{0.9}Cu_{0.1}$ (top to bottom respectively) glasses at T=1000K. Ag(black) Ge(green), Se(red) and Cu(blue)

We were able to show the diffusion of the ions even in our time scale and predict the conductivity close to the experimental data. We also studied the trap and found that Cu traps are more rigid that those for Ag making very hard for Cu to diffuse.
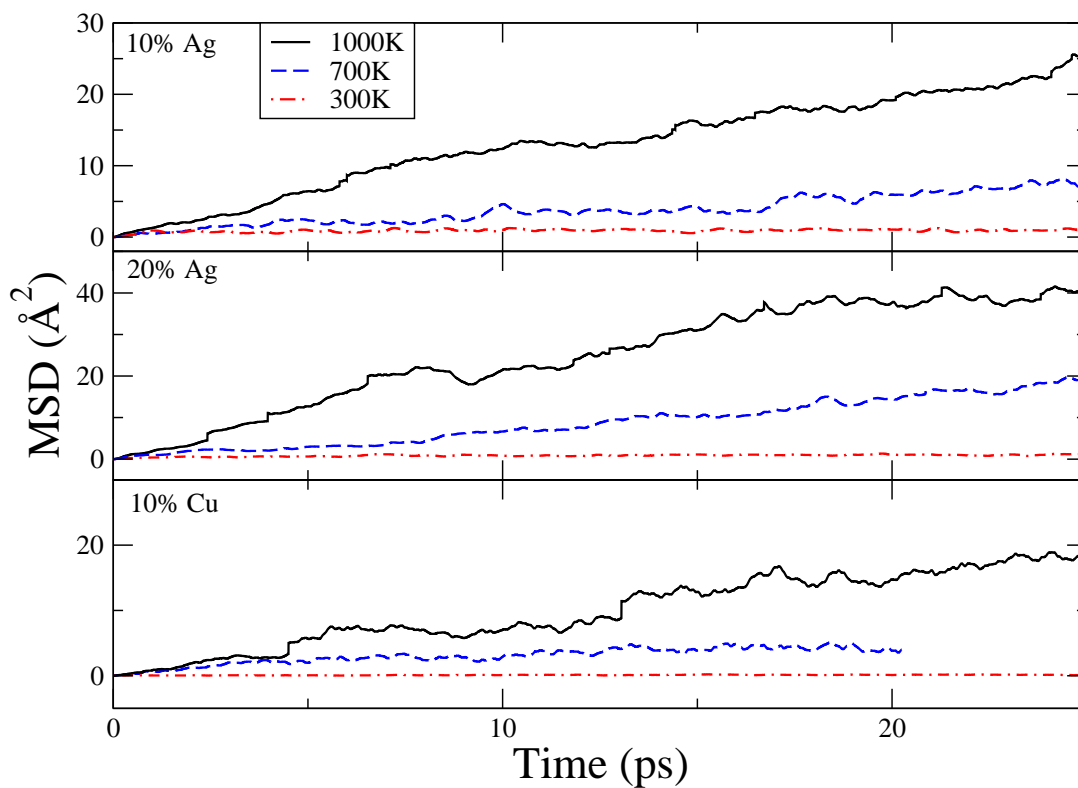
Figure 5.20: Temperature dependence of conductivity of ions for different models)
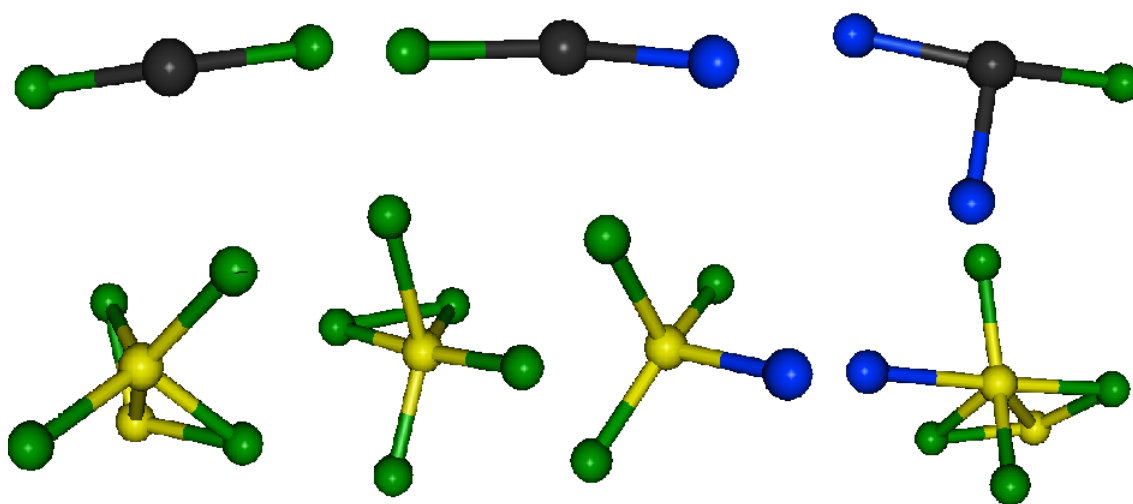
Figure 5.21: Local environments of Ag atoms(top) and Cu atoms (bottom). Black, green,blue and yellow colored atoms respectively represent Ag, Se, Ge and Cu)

6   EXAFS STUDY OF STRUCTURAL PROPERTIES OF *Ge-Sb-Te* THIN FILMS.

6.1   Introduction

Ge, Sb and Te based phase-change memory materials (PCMM) have been intensely studied for decades for their application in phase change memory devices[20]. PCMM have already been successfully used in rewritable media such as compact disks (CDs) and digital versatile disks (DVDs)[19, 76] and are currently being used in non-volatile electrical memory devices owing to their high switching speed and excellent scalability[77]. Among all the Te based alloys for the optical and electric memory applications,$Ge_2Sb_2Te_5$(denoted as GST(225))is most widely studied because of its high switching speed and long-term stability[78]. Even though properties of PCMM(e.g., electrical and optical properties) are well characterized[79], the mechanism of the structural rearrangement that takes place during crystallization and amorphization in these materials is incompletely understood. It is well known that the crystal structure of GST(225) closely resembles the rock-salt structure with Te atoms occupying one fcc sublattice site and Ge, Sb and vacancies occupying the second fcc sublattice site[19, 80]. However the structure of amorphous state of the alloy is still a topic of debate. The structure of amorphous GST(225) has been intensively investigated by EXAFS[81, 82], X-ray and neutron scattering[83, 84] and molecular dynamic simulations [23, 85–87].

In this study, we focus on atomic structure of amorphous Ge-Sb-Te (GST) alloys prepared using an electrodeposition and radio frequency sputtering methods. The purpose of this work is to understand the atomic structure of amorphous Ge-Sb-Te (GST) synthesized by using different methods. Various methods have been utilized for the synthesis of PCMM, and among which sputtering is employed dominantly. However, its poor performance in covering complex surfaces has become a critical issue in downsizing

the memory devices. The electrodeposition method could be one of the solutions for this problem because of its ability to deposit materials on mostly curved surface. This ability can be utilized to grow GST alloys in nanoporous materials and thus enables miniaturizing the phase-change memory devices. We perform an EXAFS analysis to study the atomic structures.

6.2   Methods

6.2.1   Electrodepostion

Ternary GST materials were synthesized by an electrodeposition method using a traditional three-electrode cell. A Princeton Applied Research potentiostat (model 273a) was used as the power source for the electrodeposition. The counter, reference, and working electrodes used for the electrodeposition were a platinum foil, a saturated calomel electrode (SCE), and a gold film (c.a. 50 nm in thickness) coated on a microscope glass slide, respectively. The electrodeposition was conducted at 22^oC on two solutions that contain Ge, Sb and Te ions. The solutions were prepared by adding various amounts of GeO_2, $SbCl_3$ and TeO_2 powders to a mixture of 1M nitric acid and 1M sulphuric acid. Then the solutions were stirred for an extended period of time until all the powders were dissolved completely. The final solutions were adjusted to pH = 0.3 by adding NaOH.

The deposition voltage was fixed at -0.6V (relative to SCE) for both solutions. The current densities were 0.5 and 0.8 mA/cm^2 for Sample 1 and 2, respectively, and the current was stable during the deposition. The thickness of the deposited films was estimated to be 100–200 nm.

6.2.2   Radio Frequency Sputtering

$Ge_1Sb_2Te_4$ thin film was prepared by radio frequency sputtering(13.56 MHz) from a $Ge_1Sb_2Te_4$ target (50 mm in diameter) in pure Argon at an average power of 5 $Watts/cm^2$.

Table 6.1: Solution contents and the sample composition

Deposition method	Ge%	Sb%	Te%
Electrodeposition	6	9	85
	9	27	63
Sputtering	16	28	56

Silver plates each measuring 8mm ×15mm ×1mm were placed on the target, with thin Tantalum foil placed between the plates and the $Ge_1Sb_2Te_4$ target. Typical Ar pressure was 8 mTorr. Thickness of the films was measured with a quartz crystal thickness monitor.

The compositions of the $Ge_1Sb_2Te_4$ film were obtained by energy dispersive X-ray spectroscopy (EDXS) performed at multiple locations of the samples and presented in Fig.6.1.

The EXAFS experiment was conducted at the 5-BM beamline of the Advanced Photon Source (APS), Argonne National Laboratory. The synchrotron ring was operated at 7GeV in a standard top-up mode with a constant beam current of 100 mA. The Ge K-edge(11.104KeV) EXAFS spectrum was measured under transmission mode and Sb(30.491KeV) and Ag(25.514KeV) K-edge spectra were measured under fluorescence mode. The transmitted X-ray beams were measured by the ionization chamber and the fluorescence signals from the samples were collected by a 13-element Ge detector at room temperature. A reference sample that contains the three elements was used as a reference to calibrate the X-ray energy for different scans at the same K edges.

The process of analysis of the data is described in Chapter 3. The scattering paths and phase shift information were calculated by using FEFF[7] using a model of $Ge_2Sb_2Te_5$ of Ref. [23] and the structural parameters in the expression of $\chi(k)$ were optimized by using Artemis[6].

6.3   Results and Discussion

The EXAFS oscillations (χ(k)) were extracted from the normalized absorption spectra and then Fourier transformed (FT) to get derived χ(r) spectrum. The derived χ(r) spectrum provides structural information such as bond length, coordination number and mean square relative displacement (MSRD) of the absorbing atoms. It should be noted that these $\chi(r)$ spectra are not a true radial distribution function since we ignored a multiple scattering effect, and the apparent distances in the FT magnitude are shifted due to the phase shift term $\phi(k)$. However, as the average bond length can be derived from the FT magnitude via correction of the total phase shift experienced by the photo-electron, the FT magnitude is often referred to as the pseudo-radial distribution function. Fig. 8.2 shows k^3 weighted Ge and Sb χ(r) spectra of the GST samples(uncorrected for phase shifts) with. k ranges selected for the Fourier transform were $3–10\text{Å}^{-1}$ and $4–10\text{Å}^{-1}$ for Ge and Sb edges, respectively. Beside the main peaks, we also observed smaller peaks near 1.0–2.0Å mainly in Ge and Sb edge spectra. These peaks are mostly due to a termination effect caused by finite k range of Fourier transform and thus are neglected in the analysis. To obtain the structural parameters, these χ(r) spectra were fitted with Artemis[6] using the appropriate scattering paths calculated from a corresponding GST model via FEFF[7]. Since the atomic numbers and radii of Sb and Te are close to each other, and they may not readily be distinguishable via EXAFS, the contribution from Sb neighbor atoms was ignored. This is appropriate in the analysis because, as also reported by Prasai *et al.* in the *ab-initio* molecular (AIMD) generated models, the probability of finding Sb as a neighbor is less than 0.15 for all Ge, Te and Sb central atoms. The fitted average bond lengths and the coordination numbers are illustrated in Table 6.2.

As a benchmark, we started with Sample 3 ($Ge_{16}Sb_{28}Te_{56}$) which has a composition close to $Ge_1Sb_2Te_4$. The average Ge-Te bond length of 2.61 Å and Sb-Te bond length of

Table 6.2: Fitted structural parameters of the first atomic shells of the Ge and Sb atoms in Sample 1 ($Ge_6Sb_9Te_{85}$), Sample 2 ($Ge_9Sb_{27}Te_{63}$), and Sample 3 ($Ge_{16}Sb_{28}Te_{56}$).

Bond Pairs	Samples	Bond length(Å)	Coord. No.	σ^2(Å^2) ($\times10^{-3}$)
	1	2.61±0.01	3.4±0.6	5.0±0.9
Ge-Te	2	2.61±0.01	3.2±0.6	4.5±1.0
	3	2.61±0.01	3.1±0.6	4.6±0.5
	[a]$Ge_1Sb_2Te_4$	2.61±0.01	3.3±0.3	3.5±0.4
	[b]$Ge_2Sb_2Te_5$	2.63±0.01	3.3±0.2	
	1	2.86±0.01	3.2±0.6	5.6±1.1
Sb-Te	2	2.84±0.01	3.0±0.5	5.4±0.9
	3	2.84±0.01	2.9±0.6	4.8±0.8
	[a]$Ge_1Sb_2Te_4$	2.84±0.01	2.9±0.4	3.7±0.6
	[b]$Ge_2Sb_2Te_5$	2.83±0.01	2.8±0.1	

[a] Ref. [21]

[b] Ref. [82]
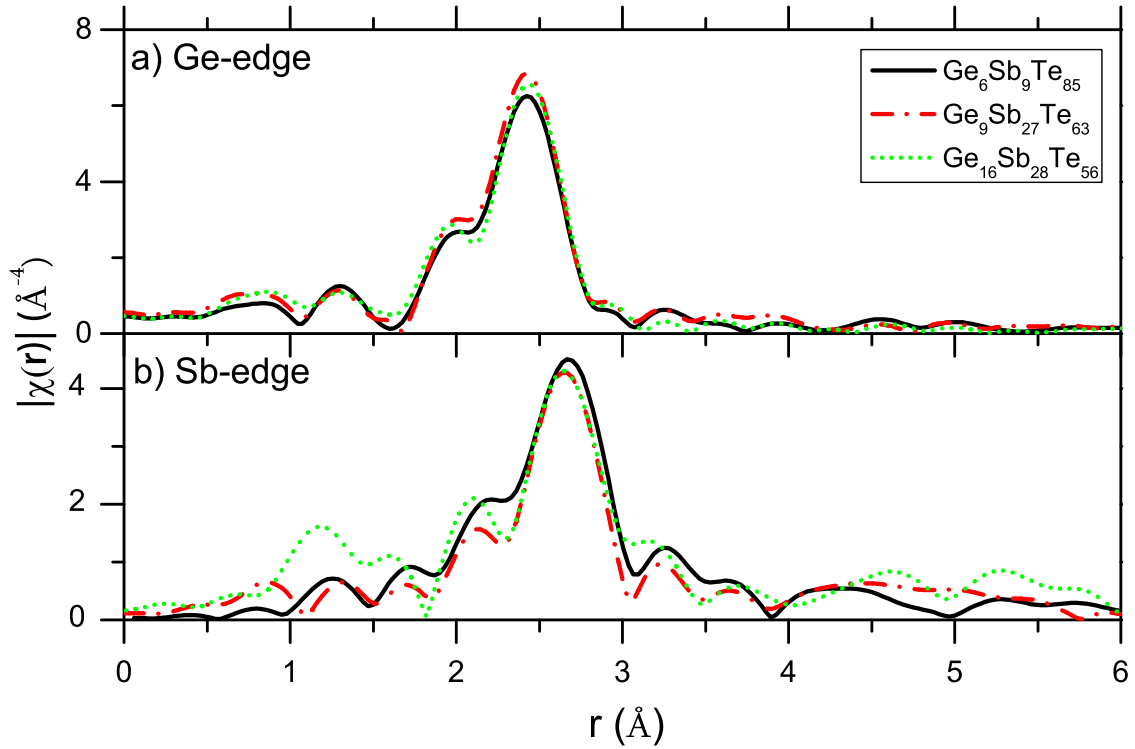
Figure 6.1: (Color online)Magnitude of k^3 weighted $\chi(r)$ spectra (uncorrected for phase shift) in GST samples. k ranges chosen for the Fourier Transform are; 2-12 Å^{-1} for Ge K-edge (a) and 3-11 Å^{-1} for Sb K-edge (b).

2.84Å obtained from our analysis are in consistency with the previously reported bond lengths for a-Ge$_1$Sb$_2$Te$_4$ [21, 84]. These numbers are also similar to those reported for a-Ge$_2$Sb$_2$Te$_5$ [81, 82] that also lies on the same pseudo-binary line of GeTe and Sb$_2$Te$_3$. Moreover, the coordination numbers of Ge and Sb are similar to those previously reported results[21, 82].

Now turning back to other samples, we observed no difference in the average Ge-Te bond lengths as the relative concentration of Ge increases (see Table. 6.2). In contrast, Sb-Te bond length showed some significant dependence on relative concentration of Sb in the samples. The average Sb-Te bond length is observed to be longer in the sample in which the concetration of Sb is very low as compared to that of Te. Nevertheless we

observed no significant difference in the average bond lengths between Sample 2 and 3, implying the similar local structure irrespective to the methods of sample preparations. The coordination numbers on the other hand are observed to be decreased for both Ge and Sb as the relative concentration of Ge and Sb increases.

The overall disorder parameters (i.e., MSRD) for the Ge-Te and Sb-Te pairs can be found in Table 6.2. The MSRD for the Sb-Te pairs was relatively higher in all samples as compared to the Ge-Te pairs, inferring more disorder in the case of Sb. One of the reasons behind this difference is probably due the fact that in a covalent network, the average coordination number of Sb is 3 while that of Ge is 4. The more rigid Ge-Te bonds make the network less flexible and thus result in a smaller value in the disorder parameter.

6.4   Conclusion

Ge-Sb-Te ternary mixtures with three different compositions were synthesized successfully using an electrodeposition or RF sputtering method. The EXAFS analysis confirms no significant difference in the average Ge-Te and Sb-Te bonds depending on the method of sample preparation. Although sputtering method is employed dominantly, its poor performance in covering complex surfaces limits the use of sputtering methods. The use of electrodepostion method can solve this issue as this method is known to have an ability to deposit materials on any surfaces irresptive of its curvature and thus can be utilized to grow GST alloys in nanoporous materials and thus enables miniaturizing the phase-change memory devices.

7 DIRECT *ab-initio* MOLECULAR DYNAMIC STUDY OF ULTRAFAST PHASE CHANGE IN *Ag*-ALLOYED *Ge$_2$Sb$_2$Te$_5$*

B. Prasai, G. Chen, and D. A. Drabold

*Direct ab-initio molecular dynamic study of ultrafast phase change
in Ag-alloyed Ge$_2$Sb$_2$Te$_5$*

Applied Physics Letters, **102**, 041907 (2013).

7.1 Introduction

With highly contrast optical and electrical properties, and ultrafast phase transition from amorphous to crystalline, phase change materials (PCMs) make themselves serious candidates for the next generation non-volatile memory technology[19, 88]. Already being used in commercially available rewritable optical devices and phase change random access memory (PCRAM), Ge$_2$Sb$_2$Te$_5$ (GST), with the compositions around GeTe-Sb$_2$Te$_3$ pseudobinary line[20], is one most popular PCMs.

The computational design of materials is still in its nascent stages, but is widely recognized to be one of the prime frontiers of materials science. The challenges are daunting for several reasons, among these: time and length scales drastically different in simulation compared to laboratory samples, the need for realistic interatomic interactions (nowadays largely based upon pseudopotentials and density functional theory) leads to tremendous demand for computational resources. In the case of the phase change memory materials, with compositions near Ge$_2$Sb$_2$Te$_5$ (GST), there is clear evidence that current first principles simulations can accurately simulate phase changes on the time scales accessible to these codes[86]. Other work suggests that key quantities like crystallization speed can be meaningfully inferred from such simulations[86]. These materials are of

fundamental interest for their ultrafast phase changes and are the leading candidate to replace current non-volatile computer memory, a multi-billion dollar market.

In this study, we explore new candidate phase change materials and show that a silver-doped variant may be superior to conventional GST. We elucidate the process of crystallization in atomistic detail and particularly note the role of the Ag in producing more stable and chemically ordered materials. Beside the specific prediction that the Ag alloy systems deserve careful exploration, we highlight the existence of a promising unexplored which strongly suggests that others probably exist as well, and deserve exploration.

7.1.1 Molecular Dynamic simulations

We have implemented an *ab-initio* molecular dynamic (AIMD) simulations to study the ultrafast crystallization of Ag-doped (alloyed)$Ge_2Sb_2Te_5$. The AIMD calculations were performed using Vienna *Ab-initio* Simulation Package (VASP)[45–47] to generate models of $Ge_2Sb_2Te_5$ and $Ag_{0.5}Ge_2Sb_2Te_5$ (AGST) with 108(24 Ge atoms, 24 Sb atoms and 60 Te atoms) and 114(24 Ge atoms, 24 Sb atoms, 60 Te atoms, and 6 Ag atoms) atoms, respectively. The calculations were performed by using the projector augmented-wave (PAW)[89, 90] method to describe electron-ion interactions. The Perdew-Burke-Ernzerhof (PBE)[91] exchange correlation functional was used throughout. Molecular-dynamics (MD) simulations were performed in a cubic supercell with a time step of 5.0 fs using periodic boundary conditions at constant volume for annealing, equilibrating and cooling, whereas, zero pressure conjugate gradient (CG) simulations were performed for relaxation. The final models were prepared by using the ``Melt and Quench´´ method[51] starting with a random configuration at 3000K. Densities of 6.046 gcm^{-3} and 6.234 gcm^{-3}, respectively for GST and Ag-GST, were used during the process. After mixing the random configurations at 3000K for 20ps, each model was cooled to

1200K in 10ps and equilibrated for 60ps. A cooling rate of 12K/ps was adopted to obtain the amorphous models from the melt at 1200K to 300K and followed by equilibration at 300K for another 50ps. Finally the systems were fully relaxed to a local minimum at 0 pressure. Three different models were generated for each of the structures. For the illustraion purpose one such zero-pressure structure, each of amorphous GST and AGST, is presented in Fig.9.1(a-b).Each of these models was then equilibrated at 300K for 25ps and data was accumulated for the last 10ps and statistically averaged to study the structural properties. Three independent models were generated for both structures.

7.2 Result

7.3 structure

The relaxed structures of amorphous and crystalline $Ge_2Sb_2Te_5$ and $Ag_{0.5}Ge_2Sb_2Te_5$ are presented in Fig.9.1. To investigate the modification of GST network, we analyzed the structural properties of the models via partial pair correlation functions (PPCFs), bond angle distributions (BADs) etc. The PPCFs and BADs at 300K are presented in figures 7.2 and 9.3 respectively. The peaks at 2.91, 4.11, and 6.25Å agree well with results reported by Akola *et al.* [92](2.88, 4.17, and 6.25Å). Except for few minor modifications, the PPCFs are identitcal in both the pure and doped a-GST. The detailed average bond lengths are presented in Table.7.1. One of the noticable changes is in amorphous Ge-Te bond length which is found to be increased (by 0.02Å) in doped GST. This slight change in the Ge-Te bond length can be attributed to change in Ge environment which is also reflected in Ge centered BAD. The supression near 109o in the BAD confirms the reduction of tetrahedral Ge due to addition of Ag. The reduction of tetrahedral Ge causes the decrease in the average Ge-Te bond length since Ge-Te bond lenghts with tetrahedral geometry is smaller than Ge-Te with octahedral geometry

(a)

(b)

(c)

(d)
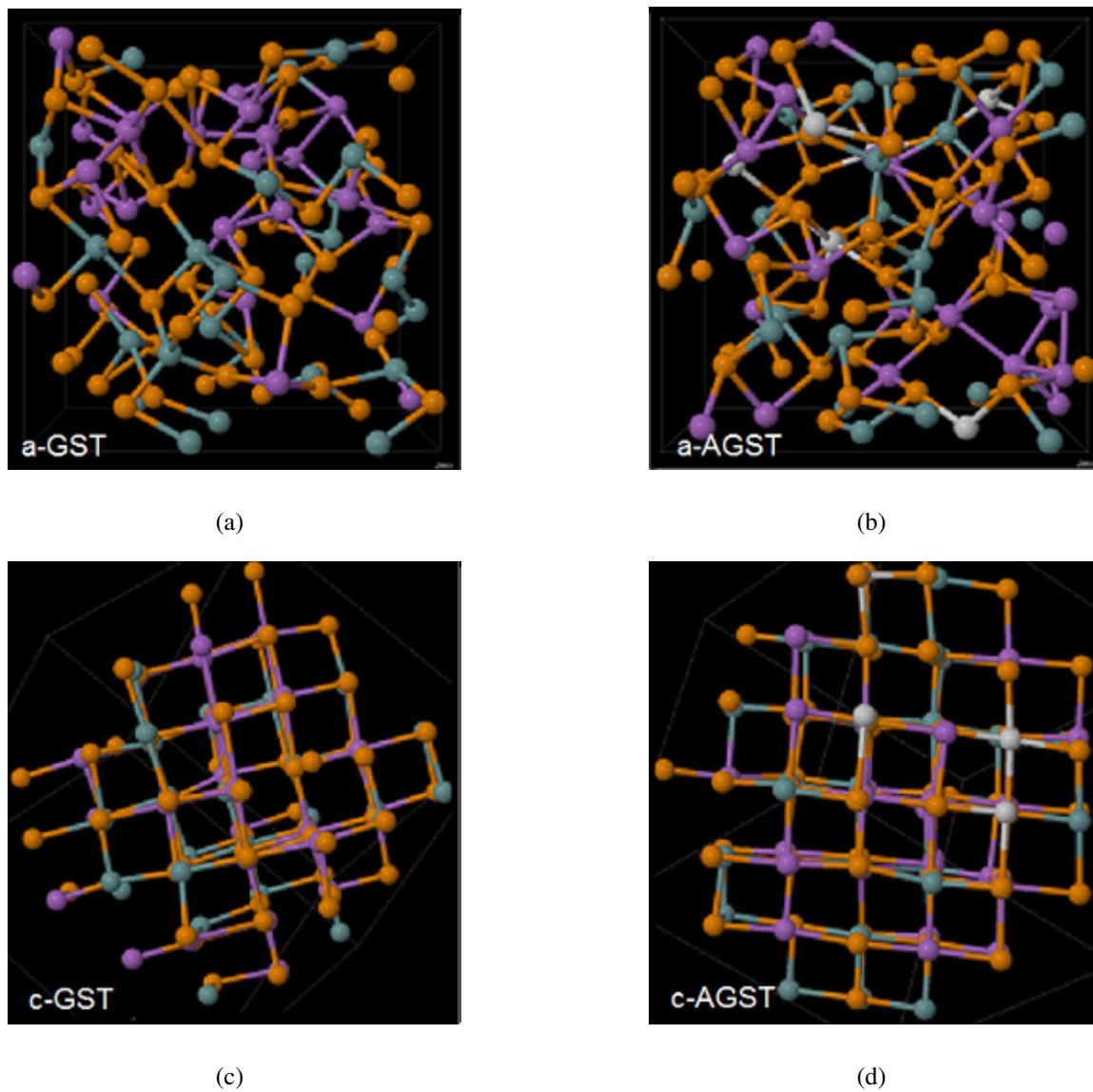
Figure 7.1: Simulated structures of a) a-$Ge_2Sb_2Te_5$, b) a-$Ag_{0.5}Ge_2Sb_2Te_5$, c)c-$Ge_2Sb_2Te_5$, and d) c-$Ag_{0.5}Ge_2Sb_2Te_5$. (Model 3).

[93, 94]. This can further be verified by equal Ge-Te bond lengths in crytalline phase where it is believed that all the tetrahedral Ge changes to an octahedral geometry. On the other hand, Sb-Te bond length remains same with no major change in the Sb-Te PPCF and Sb-centered BAD, in both the phases. This can also be supported by the fact that Sb always takes octhedral geometry in either of the phases. Besides Ge-Te and Sb-Te bonds
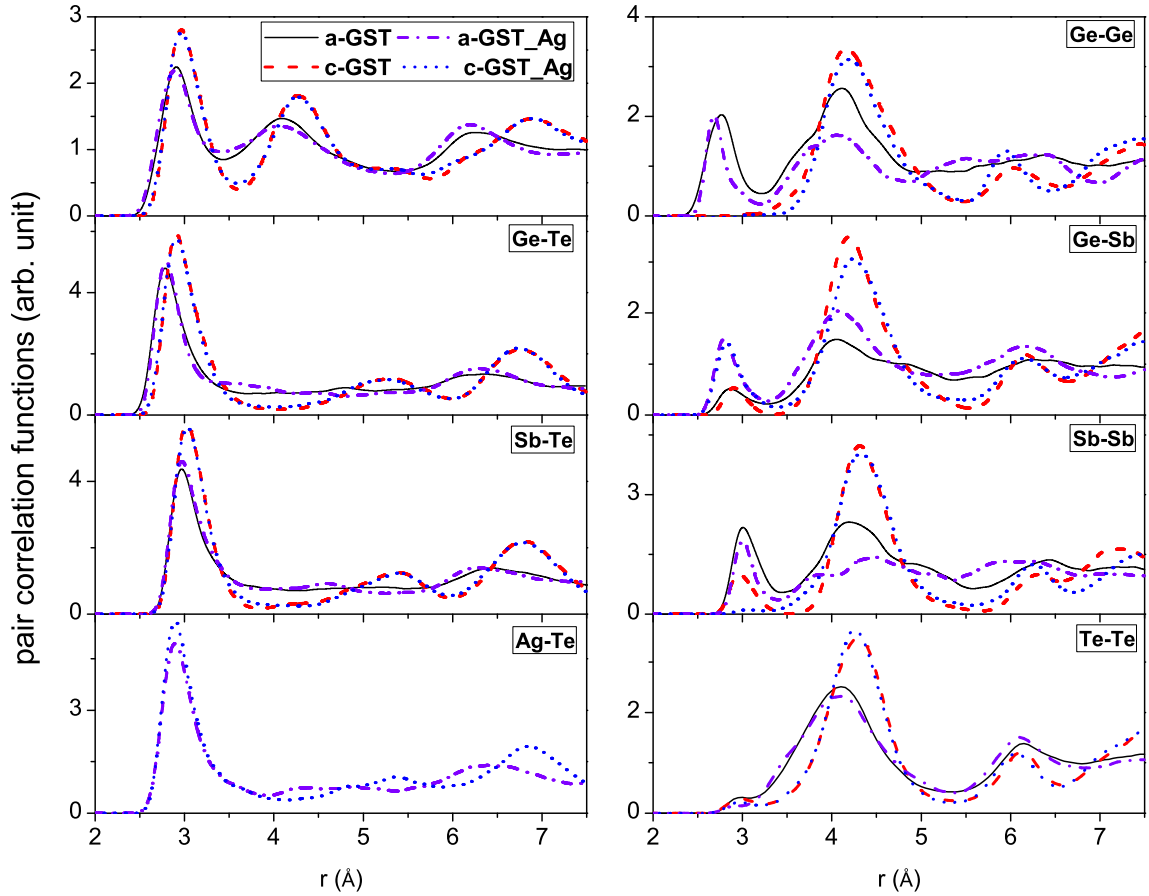
Figure 7.2: Partial pair correlation functions in amorphous and crystalline $Ge_2Sb_2Te_5$ and $Ag_{0.5}Ge_2Sb_2Te_5$ at 300K. Only one model(Model 3) from each of the $Ge_2Sb_2Te_5$ and $Ag_{0.5}Ge_2Sb_2Te_5$ models is presented for the illustrations purpose. Models with almost identical wrong bonds were chosen.

pairs we observed a significant amount of Ge-Ge, Ge-Sb, Sb-Sb and Te-Te bond pairs. These bond pairs which are termed as wrong bonds[86], count up to 25% in amorphous phases and comes down to about 6% in the crystalline phases. From the analysis of the local sturcture, we are also able to identify the interaction of the dopants (Ag atoms) in the host network. The Ag PPCF confirms that Ag is mainly bonded to Te rather than to Ge or Sb. This is also true in crystalline phase where Ag takes the vacancy sites(or similiar sites as Ge/Sb). Similar to the amorphous phase, the crystalline phases of both $Ge_2Sb_2Te_5$ and
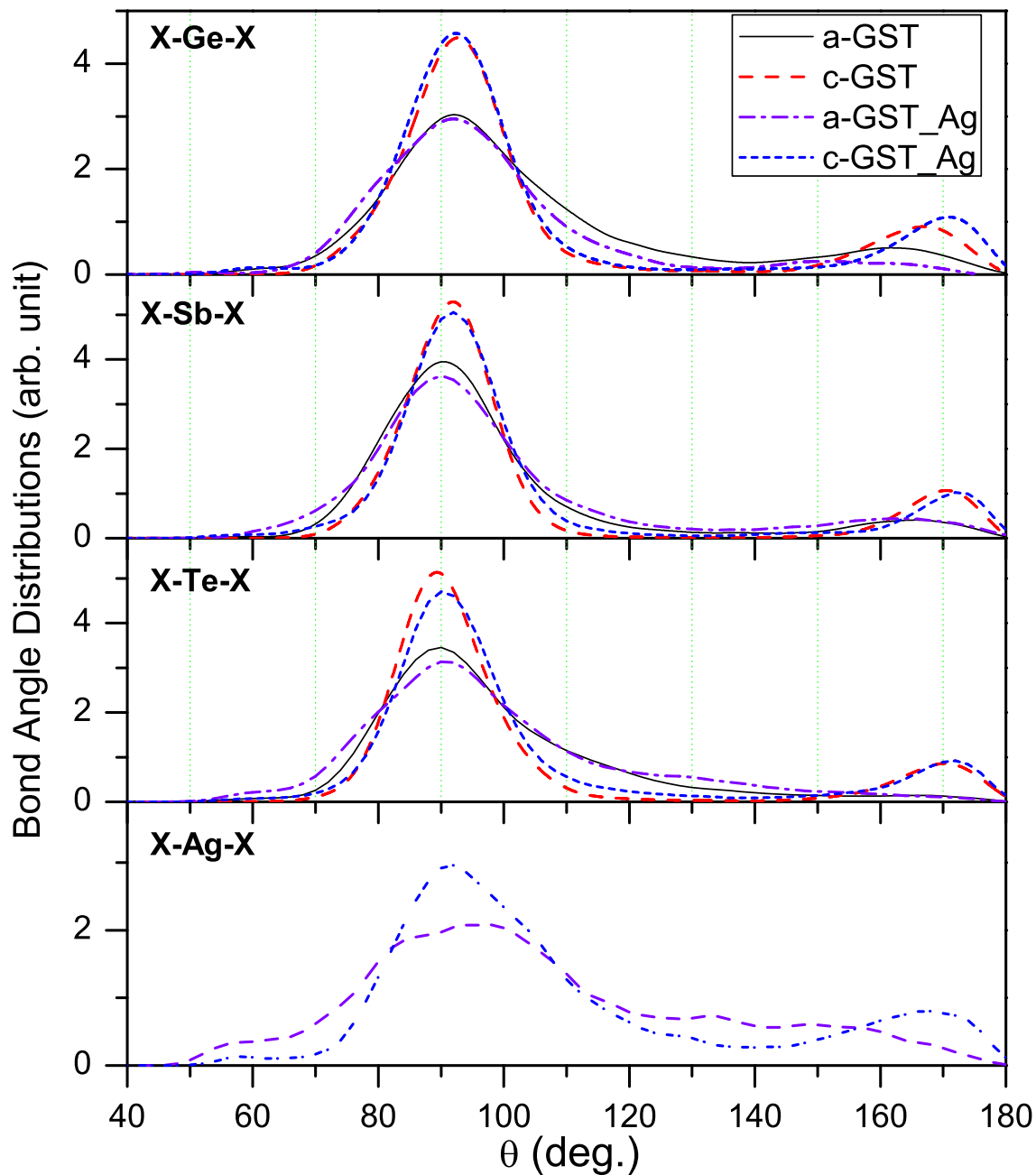
Figure 7.3:   Bond angle distributions(Model 3) in amorphous and crystalline $Ge_2Sb_2Te_5$ and $Ag_{0.5}Ge_2Sb_2Te_5$ at 300K.

$Ag_{0.5}Ge_2Sb_2Te_5$ confirms almost identical correlations functions. The peaks at 2.98, 4.26, 5.35, 6.87, and 7.45Å well represent the reminisence of crystalline $Ge_2Sb_2Te_5$. These

values are in good aggrement with results reported by Akola *et al.* [92]. The peaks at 2.98, 5.35 and 6.87Å are attributed to X-Te (where X=Ge,Sb,Ag) correlations whereas peaks at 4.26 and 7.45Å to so called wrong bonds(Ge-Ge,Ge-Sb,Sb-Sb, and Te-Te). In both of the phases there is no well defined Ag-Ag correlations. After relaxing both the phases of GST and AGST at 0 pressure we computed the atomic densities to compare the relative changes in the density between amorphous and crystalline phases. We observed relatively smaller density change (4.61%) between the two phases of AGST in contrast to density change of 6.84 % in pure GST. This smaller volume(density) change in Ag-doped GST results in the reduced residual stress in the PCM devices. We computed the coordination numubers by integrating the PPCFs upto the first minimum and present in Table9.3. From the coordination number analysis it is confirmed that the Ge-Te (N_{Ge-Te}) and the Sb-Te coordination numbers (N_{Sb-Te}) is not significantly affected as a result of doping. One interesting observation is the significant reduction of homopolar bond in $Ag_{0.5}Ge_2Sb_2Te_5$ as compared to $Ge_2Sb_2Te_5$.

Table 7.1: Average bond distances(in Å) in amorphous and crystalline $Ge_2Sb_2Te_5$ and $Ag_{0.5}Ge_2Sb_2Te_5$ at 300K, averaged over all three models. The deviation in the peak positions is within 0.01Å.

Bonds	a-GST	a-AGST	c-GST	c-AGST
Ge-Ge	2.76	2.68		
Ge-Te	2.78	2.80	2.92	2.92
Ge-Sb	2.85	2.79	2.90	2.82
Sb-Sb	3.00	3.00	2.97	3.29
Sb-Te	2.97	2.97	3.20	3.20
Te-Te	2.97	2.94	2.97	2.97
Ag-Te		2.89		2.90

Table 7.2: Comparison of coordination statistics in $Ge_2Sb_2Te_5$ and $Ag_{0.5}Ge_2Sb_2Te_5$ at 300K, averaged over all three models. The deviation is within 5%.

	Ge	Sb	Te	Ag
		a-GST		
Ge	0.55(0.58)	0.15(0.17)	3.48(3.63)	-
Sb	0.15(0.17)	0.49(0.42)	2.78(2.83)	-
Te	1.39(1.45)	1.11(1.13)	0.25(0.20)	-
		c-GST		
Ge	0.04(0.04)	0.12(0.13)	5.38(5.38)	-
Sb	0.12(0.13)	0.25(0.25)	5.23(5.08)	-
Te	2.15(2.15)	2.09(2.03)	0.22(0.20)	-
		a-AGST		
Ge	0.38(0.5)	0.37(0.46)	3.44(3.46)	0.13(0.04)
Sb	0.37(0.46)	0.37(0.42)	2.82(2.79)	0.03(0.08)
Te	1.37(1.38)	1.13(1.11)	0.14(0.17)	0.38(0.42)
Ag	0.50(0.17)	0.14(0.33)	3.77(4.17)	0.03(–)
		c-AGST		
Ge	0.04(-)	0.36(0.35)	5.41(5.34)	0.04(0.02)
Sb	0.36(0.46)	0.03(0.08)	5.21(5.18)	0.04(0.02)
Te	2.16(2.14)	2.08(2.07)	0.17(0.09)	0.53(0.53)
Ag	0.16(0.18)	0.16(0.08)	5.29(5.33)	–

7.4 Electronic Properties

We also computed the electronic density of states (EDOS) to compare the electrical properties of $Ge_2Sb_2Te_5$ and $Ag_{0.5}Ge_2Sb_2Te_5$ and present in Fig.9.5. The EDOS shows no major differences, with p-like states of Te, Sb and Ge dominating both the valence and
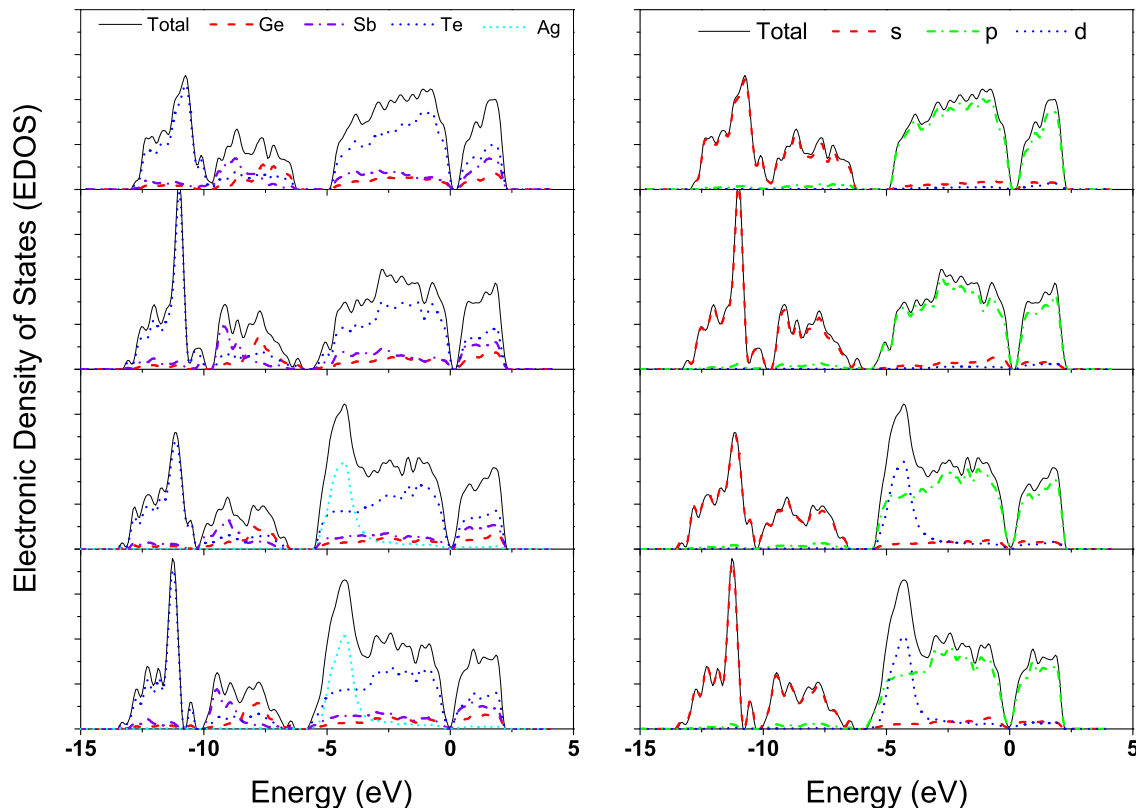
Figure 7.4: Electronic desity of stats(EDOS) in the two phases of $Ge_2Sb_2Te_5$ and $Ag_{0.5}Ge_2Sb_2Te_5$. (Model 3).

the conduction band. Ag on the other hand contribute to d-like state about 4eV below the fermi level. The gamma point band gap is observed to decrease with the presence of Ag. Since the larger band gap in a-GST as compared to c-GST is due the presense of sp^3-bonded Ge atoms[85], the reduced band gap due to doping can also be attributed to the reduction of the tetrahedral Ge atoms.

7.5 Optical Properties

One of the reasons why PCMs are so useful is the contrast optical properties they possess. Fig.9.6 illustrates the comaprison of the dielctric functions in $Ge_2Sb_2Te_5$ and $Ag_{0.5}Ge_2Sb_2Te_5$. The imaginary part and the real part of the dileclectric function confirm

that the optical contrast is preserved in $Ag_{0.5}Ge_2Sb_2Te_5$. These results are in a good agreement with the results reported by Shportko *et al.* [95] (presented in the insets of Fig.9.6). We estimated the optical dielectric constant i.e. the lower energy-limit of the real part of the dielectric function ($\omega \to 0$) and present in Table 7.3. We observed a slightly higher dielectric constant in $Ag_{0.5}Ge_2Sb_2Te_5$ as compared to $Ge_2Sb_2Te_5$ and attribute this to a fact that the medium-range order is improved in $Ag_{0.5}Ge_2Sb_2Te_5$. This improved medium-range order which is needed for resonant bonding and is absent in the amorphous phase[95] can lead to the faster crystallization in $Ag_{0.5}Ge_2Sb_2Te_5$ over $Ge_2Sb_2Te_5$.

Table 7.3: Comparison of dielectric constant between the two phases of $Ge_2Sb_2Te_5$ and $Ag_{0.5}Ge_2Sb_2Te_5$. (Model 3)

Material	Amorphous	Crystalline	%increase
$Ge_2Sb_2Te_5$	25.9	53.0	105
$Ge_2Sb_2Te_5$(Ref.[95])	16.0	33.3	108
$Ag_{0.5}Ge_2Sb_2Te_5$	26.9	60.2	124

7.6 Crystallization

To directly investigate amorphous to crystalline phase transition, we annealed the a-GST and a-AGST models at 600K and 650K respectively until each of the models is crystallized. The whole process consists mainly of three regions(I, II, and III), as also explained by Lee *et al.*[96]. The region I is basically termed as the incubation period, the region II that starts at the end of the incubation period is the main region where the whole process of crystallization occurs and the third region(III) defines the completely crystallized state. To understand the whole crystallization process we observed the evolutions of total energy of the system, the number of 4-member rings (seeds), and the number of wrong bonds as a function of time and present in Fig.9.8. Interestingly, we
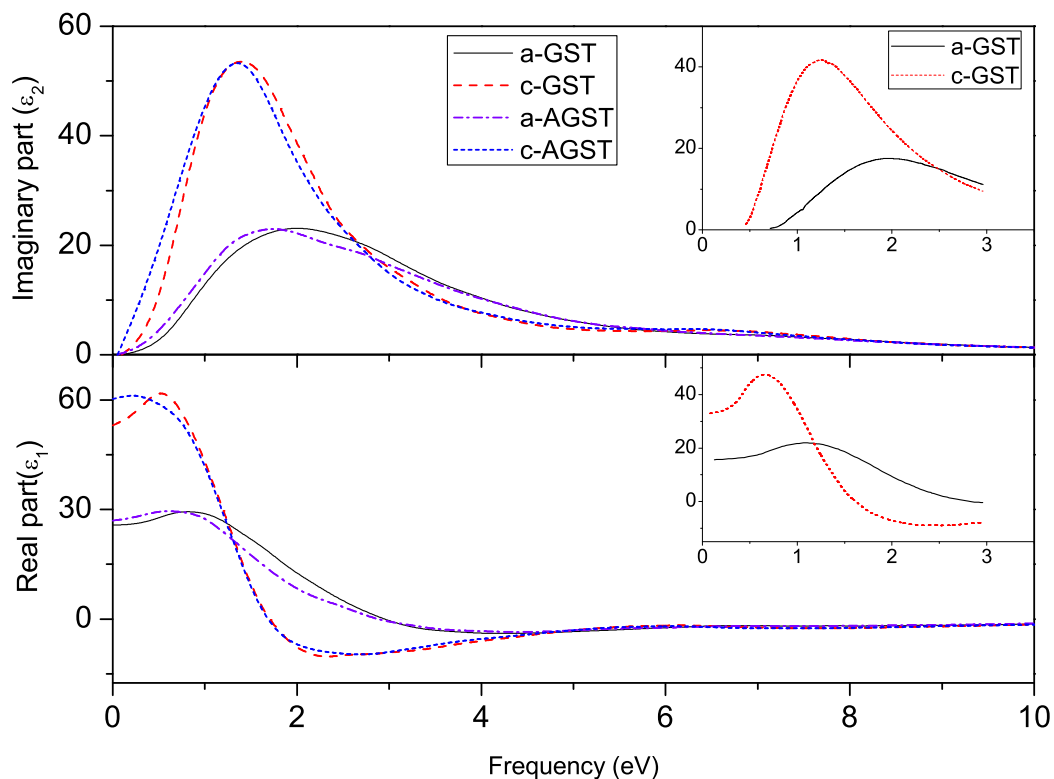
Figure 7.5: Comparison of dielectric functions in the two phases of $Ge_2Sb_2Te_5$ and $Ag_{0.5}Ge_2Sb_2Te_5$. (Model 3).

observe almost no change in the total energy and the number of 4-member rings during the incubation period(region I), however, we observe the significant decrease in the number of wrong bonds. Wrong bonds keep decreasing during the crystallization period (region II) until the crystallization period is complete. About 5 to 7 % of wrong bonds(mainly Ge-Sb and Sb-Sb bonds) still present even after the crystallization is occured. The total energy and the number of 4-member rings on the other hand are found to be correlated to each other, with number of rings increasing monotonously during the crystallization period. We further computed the evolution of pair correlation functions, the Ge-centered bond angle distribution and the coordination numbers(for model 3) and

present in figures 7.7,7.8, and 7.6(b) respectively. The top panels of Fig.7.7 represent the total pair correlation functions (TPCF), middle panels the X-Te pair correlation functions and bottom panels the correlation of wrong bonds. All of these figures clearly depict the evolution of medium to long range order which is the signature of the crystalline structures. The prominent medium to long range peaks start evolving during the period II. The average peak postions at 2.98Å, 5.3Å, and 6.8Å for X-Te and 4.2Å and 7.4Å for wrong bonds well represent the crystalline GST structure. Similarly, Ge-centered BAD (Fig.7.8) shows narrow and prominient distribution around 90° and 180°, the singatures of crystalline GST structures. The peak at 90° becomes narrow and tall illustrating the conversion of tetrahedral Ge (angular distribution at 109°) into the octrahedral Ge. The peak at around 180° also becomes visible during the period II showing a clear correlation with the pair correlation functions. The coordination numbers(CN), on the other hand depicts a correlation with the total energy of the system *i.e.* the CN is almost constant during the incubation period while starts increasing during the crystallization period and becomes constant after the crystallization is estabilished.

Now, to investigate the effect of dopant (Ag) to the crystallization we compare total energy, the number of four member rings and the coordination number (Fig.9.8 and 7.6(b)). Since the crystallization of three different models of pure GST shows big fluctuation in the duration of region I and II, especially the region I, the estimation of crystallization time shows big uncertainty. The incubation periods(region I) in three different pure $Ge_2Sb_2Te_5$ models vary from 50 ps to 200ps whereas the crystallization periods (region II) vary from 40ps to 150ps. These times in $Ag_{0.5}Ge_2Sb_2Te_5$ are (80-110ps) for incubation periods and (70-110) for crystallization periods. To understand this we examined the local structures of the starting configuration of the three GST models. Interestingly we observe a clear distinction in the number of wrong bonds and
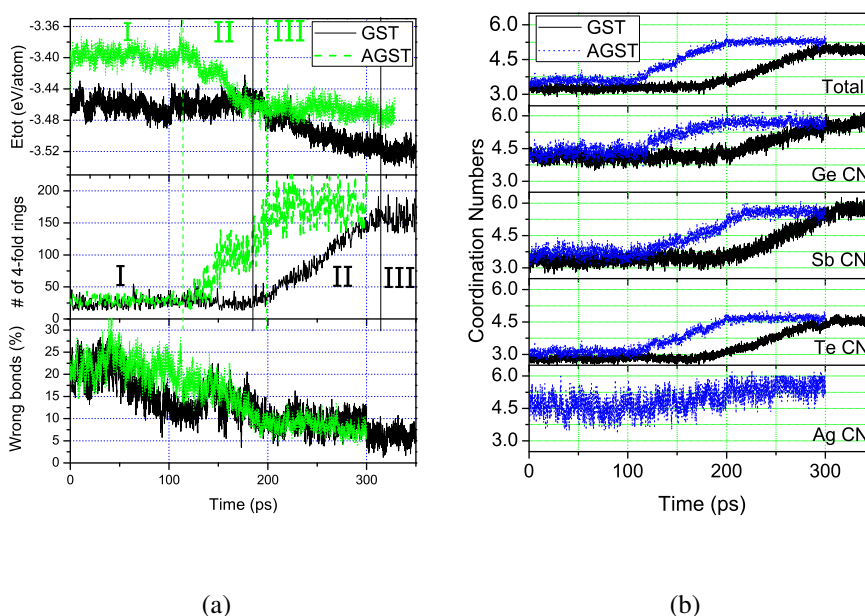
Figure 7.6: a) Comparison of the total energy (top), the number of four-fold rings (middle), and the number of wrong bonds (bottom) and b) coordination numbers as a function of time in $Ge_2Sb_2Te_5$ and $Ag_{0.5}Ge_2Sb_2Te_5$.(Model 3).

four membered rings, i.e. the model with the incubation as well as the crystallization period shorter has the least number of wrong bond and most number of four membered rings(more ordered in a plane). Hence, to compare the crystallization of $Ge_2Sb_2Te_5$ and $Ag_{0.5}Ge_2Sb_2Te_5$ we chose configuration with almost the same number of the wrong bonds. We observed a clear contrast in the duration of both the incubation period and the crystallization period in these two networks. Both of the periods were shorter in AGST than in $Ge_2Sb_2Te_5$. Total of these two periods in AGST measure about 200ps against about 315ps in pure $Ge_2Sb_2Te_5$, clearly suggesting a faster crystallization in Ag-doped GST. The total coordination numbers in the crystallization has been improved due to the high coordination number of Ag. We further, computed the difference in the energies between the amorphous and the crystalline phases in both the GST and AGST. The energy difference of 80 meV/atom in $Ag_{0.5}Ge_2Sb_2Te_5$ is about 20meV/atom more than that of
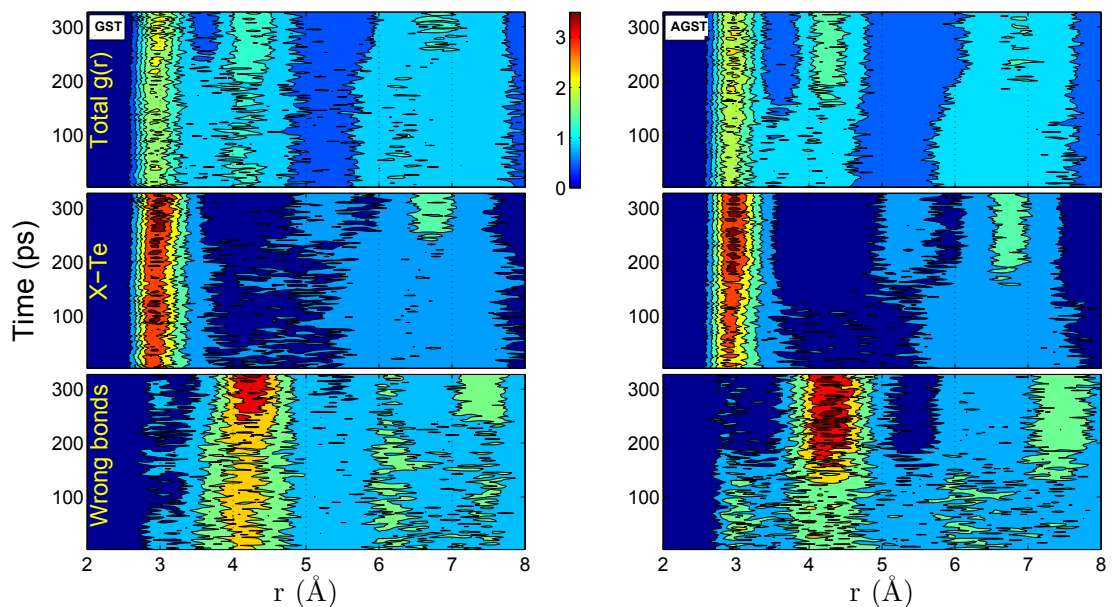
Figure 7.7: Evolution of pair correlation functions in $Ge_2Sb_2Te_5$ (left) and $Ag_{0.5}Ge_2Sb_2Te_5$-(right) with time. (Model 3).
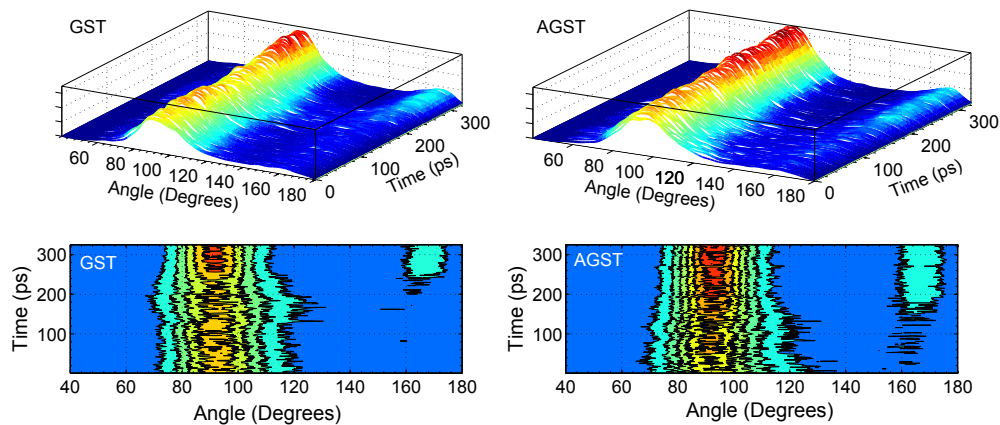
Figure 7.8: Time evolution of Ge-centered bond angle distributions in $Ge_2Sb_2Te_5$ (left) and $Ag_{0.5}Ge_2Sb_2Te_5$ (right). (Model 3).

pure $Ge_2Sb_2Te_5$. This larger energy difference could explain the better thermal stability of $Ag_{0.5}Ge_2Sb_2Te_5$ which could improve the data retention capability.

7.7   Conclusion

In conclusion, we have used AIMD simulations to study the effect of Ag doping in $Ge_2Sb_2Te_5$. The medium range order is found to be improved with the addition of Ag in the form of increased four membered rings and decreased tetrahedral Ge whereas the local structure is well preserved. We were also able to simulate the whole process of amorphous to crystalline phase transition. The incubation period and the crystallization period were found to depend on the wrong bonds presented in the amorphous phase. Moreover, our simulation revealed that the crystallization speed is increased by doping $Ge_2Sb_2Te_5$ with Ag. The larger energy/atom difference between amorphous and crystalline phases also suggests that $Ag_{0.5}Ge_2Sb_2Te_5$ is thermally more stable than $Ge_2Sb_2Te_5$. On the other hand, smaller density difference in $Ag_{0.5}Ge_2Sb_2Te_5$ between the two phases as compared to $Ge_2Sb_2Te_5$ could well reduced the residual stress in the PCM devices. Furthermore, the increased difference between the optical constrast between two phases as well as the increased crystallization speed could well be implimented in PCM devices with better performance.

8 ATOMISTIC ORIGIN OF RAPID CRYSTALLIZATION OF *Ag*-DOPED *Ge-Sb-Te* ALLOYS: A JOINT EXPERIMENTAL AND THEORETICAL STUDY

B. Prasai, M.E. Kordesch, D. A. Drabold, and G. Chen

Atomistic origin of doping-enhanced rapid crystallization in Ag-doped

Ge-Sb-Te alloys:

a joint experimental and theoretical study

Phy. Status Solidi B, 1-6 (2013).

8.1   Introduction

Chalcogenide alloy systems have proven to be among the most flexible and useful materials. They are the basis of rewritable DVD technology[19], phase change[2] and conducting bridge[1] computer memory, they exhibit exotic and apparently unique photo-response, including the opto-mechanical effect[97]. Chalcogenide glasses doped with transition metals are solid electrolytes with many potential applications[1].

GST alloys near the pseudobinary $GeTe$-Sb_2Te_3 tie line [20] are widely accepted phase-change memory materials (PCMM) for application in optical and electronic memories because of their outstanding switching performance, and efforts have been devoted to improve material properties such as switching speed, phase transition temperature, and thermal stability. One way to modify the physical properties of PCMM is by doping or alloying with other elements. Doping has been studied during the past few years either by experimental methods[98–103] or theoretical/computational methods[23, 104–106].

Experimental investigations suggest that in the case of $Ge_2Sb_2Te_5$ the crystallization temperature is elevated by C, N, Mo, and Zn[98–100] doping, whereas Sn and Bi [102, 103] lower the crystallization temperature. Doping also affects the speed of crystallization. It has been reported that Ag in $Ge_2Sb_2Te_5$ accelerates the crystallization[101] .

Ab initio molecular dynamics (AIMD) investigations suggest that dopants like C and N[104–106] affect the local order of amorphous $Ge_2Sb_2Te_5$ by elevating the fraction of tetrahedral Ge atoms and hence enhancing the thermal stability. It has also been reported that Si and O[105] dopants slow the crystallization of $Ge_2Sb_2Te_5$ whereas Ag dopants[23] enhance the crystallization speed of $Ge_2Sb_2Te_5$.

The traditional trial and error approach to materials discovery has been a major obstacle to identifying new PCMM with improved properties because of our incomplete understanding of the structure-property relations. As properties of PCMM accrue from the structure, knowledge of the structure and dynamics of these materials is essential. A deep understanding of the PCMM requires a comprehensive approach that involves coupled theory and experiment. In this chapter, we present a joint experimental/theoretical study of silver doped phase change GST alloy. Building on a preliminary report on the $Ge_2Sb_2Te_5$[23] , we detail the role of Ag in the network, and its impact on crystallization in a different stoichiometry. We address two questions: (1) How does Ag affect the atomic structure of GST alloys? (2) How does Ag affect the speed of crystallization of GST? To answer these questions, we perform an extended X-ray absorption fine structure (EXAFS) analysis and density functional (DF) simulations to study the local structure of Ag doped amorphous $Ag_{0.5}Ge_2Sb_2Te_5$. DF simulations of such materials are particularly important as they provide structural information that is not readily obtained from EXAFS. Direct comparisons of EXAFS measurements and simulations demonstrate how Ag converts tetrahedral Ge into octahedral, and provides new directions in the exploration for

improved materials. Hegedus and Elliott were the first to show that direct *ab-initio* simulation of crystallization are possible[86]. We exploit this discovery in our work.

8.2 Method

8.2.1 Experimental

$(Ge_1Sb_2Te_4)_{\frac{100-x}{7}}Ag_x$ (x=0, 7, 14, 20, and 40) thin films were prepared by radio frequency sputtering (13.56 MHz) from a $Ag_{0.5}Ge_2Sb_2Te_5$ target (50 mm in diameter) in Argon at an average power of 5 Watts/cm^2. Silver plates each measuring 8mm ×15mm ×1mm were placed on the target, with thin Tantalum foil placed between the plates and the $Ag_{0.5}Ge_2Sb_2Te_5$ target. Typical Ar pressure was 8 mTorr. Thickness of the films was measured with a quartz crystal thickness monitor. $Ag_{0.5}Ge_2Sb_2Te_5$-Ag films with five different Ag dopant levels (0-40.2%) were fabricated. The compositions of the $Ag_{0.5}Ge_2Sb_2Te_5$-Ag films were obtained by energy dispersive X-ray spectroscopy (EDXS). Figure 8.1 presents the compositions of the $Ag_{0.5}Ge_2Sb_2Te_5$-Ag films used in the present study.
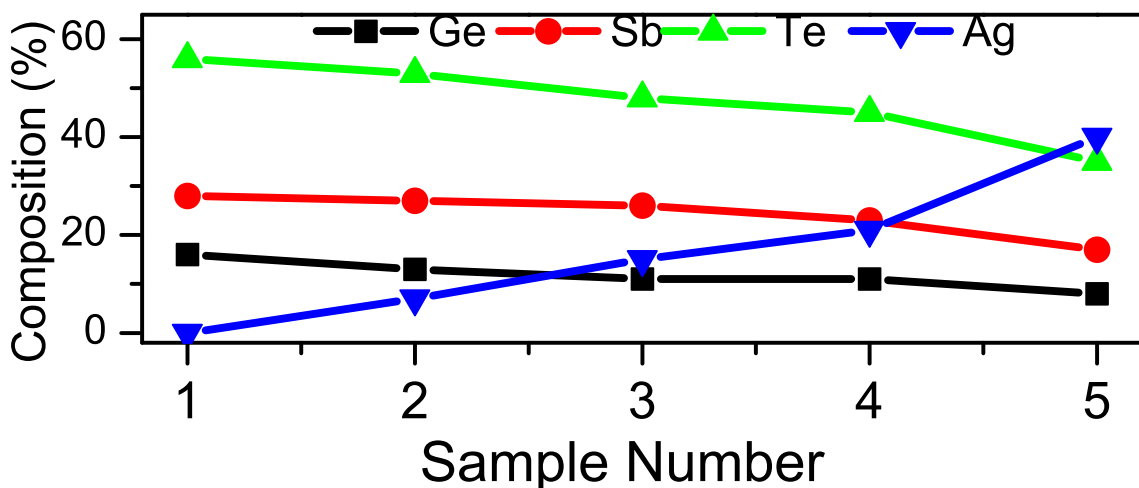
Figure 8.1: Sample compositions(in %) in Ge-Sb-Te-Ag films as measured by energy dispersive X-ray spectroscopy (EDXS). The uncertainties lie within 2%.

The EXAFS experiment was conducted at the 5-BM beamline of the Advanced Photon Source (APS), Argonne National Laboratory. The Ge K-edge (11.104KeV) EXAFS spectrum was measured at room temperature under transmission mode with ionization chambers, and Sb (30.491KeV) and Ag (25.514KeV) K-edge spectra were measured under fluorescence mode with a 13-element Ge detector. A reference sample that contains the three elements was used as a reference to calibrate the X-ray energy for different scans at the same K edges. The EXAFS data was analyzed with the FEFF[7] code (for phase shift information) using a model of $(Ge_1Sb_2Te_4)_{\frac{100-x}{7}}Ag_x$ and the structural parameters were optimized by using ARTEMIS[6].

8.2.2 Modeling: Molecular Dynamic simulations

AIMD simulations were performed using Vienna *Ab-initio* Simulation Package(VASP)[45–47] code to generate models of amorphous $(Ge_1Sb_2Te_4)_{\frac{100-x}{7}}Ag_x$. We prepared four computer models of Ag doped $Ag_{0.5}Ge_2Sb_2Te_5$ materials with Ag concentration (x) ranging 0-42%: x=0 (15 Ge atoms, 30 Sb atoms and 60 Te atoms), x=6 (15 Ge atoms, 30 Sb atoms, 60 Te atoms, and 7 Ag atoms), x=12 (15 Ge atoms, 30 Sb atoms, 60 Te atoms, and 14 Ag atoms), and x=42% (10 Ge atoms, 20 Sb atoms, 40 Te atoms, and 50 Ag atoms). The models were prepared by following the methods of Ref.[23]. Each model was equilibrated at 300K for at least 10ps and EXAFS data was simulated by using the FEFF[7] code from the configurations predicted at every 0.25ps, and subsequently, statistically averaged. At least two independent models were generated to investigate the model dependence of the structural properties. The structures (up to 10% Ag concentrations) were annealed at 650K until crystallization occurred.

8.3 Results and Discussion

Figure 8.2 shows k^3 weighted Ge, Sb, and Ag Fourier transformed EXAFS spectra ($\chi(r)$) of Ag doped $Ag_{0.5}Ge_2Sb_2Te_5$ samples (uncorrected for phase shifts) with different

Ag concentration (x). Beside the main peaks, we observed smaller peaks near 1.0–2.0Å

mainly in Ge and Sb edge spectra. These peaks are mostly due to a termination effect

caused by finite k range of Fourier transform and thus are neglected in the analysis. To

obtain the structural parameters, these $\chi(r)$ spectra were fitted with ARTEMIS[6] using the

appropriate scattering paths calculated from a $(Ge_1Sb_2Te_4)_{\frac{100-x}{7}}Ag_x$ model via FEFF[7].

Since the atomic numbers and radii of Sb and Te are close to each other, and they may not

readily be distinguishable via EXAFS, the contribution from Sb neighbor atoms was

replaced by Te atoms. This is appropriate in the analysis because the coordination number

analysis in the AIMD generated models confirms that the probability of finding Sb as

neighbor is less than 0.15 for all Ge, Te, Sb and Ag central atoms. The fitted average bond

lengths and the coordination numbers are illustrated in Figure 8.3 and Figure 8.4(a)

respectively.

As a benchmark, we started with Sample 1, whose composition (Ge=16, Sb=28, and

Te=56) is close to composition of $Ag_{0.5}Ge_2Sb_2Te_5$ within the experimental uncertainty

(2%). The average Ge-Te bond length of 2.61 Å and Sb-Te bond length of 2.84Å obtained

from our EXAFS analysis are consistent with those reported in a previous study for

a-$Ag_{0.5}Ge_2Sb_2Te_5$ [21] and are similar to those previously reported for amorphous

$Ge_2Sb_2Te_5$ [81, 82] that also lie on the same pseudo-binary line of Ge-Te and Sb_2Te_3. The

structural similarities between slightly off-stoichiometric GST alloys and stoichiometric

GST alloys have been confirmed by Caravati *et al.*[107]. However both the Ge-Te and

Sb-Te bond lengths are shorter than those obtained from DF calculations[85–87, 107].

The Ge and Sb coordination numbers of 3.0(0.4) and 2.9(0.6) obtained from our EXAFS

analysis are similar to the ones for amorphous $Ag_{0.5}Ge_2Sb_2Te_5$ as reported previously in

Ref. [21] (*i.e.* 3.3(0.3) for Ge and 2.9(0.4) for Sb). These numbers are consistent with

those obtained from DF calculations of a-$Ag_{0.5}Ge_2Sb_2Te_5$ (3.7 for Ge and 3.6 for Sb)

presented herein and those reported previously (3.5 for Ge and 3.8 for Sb) by Raty *et al.*[93].
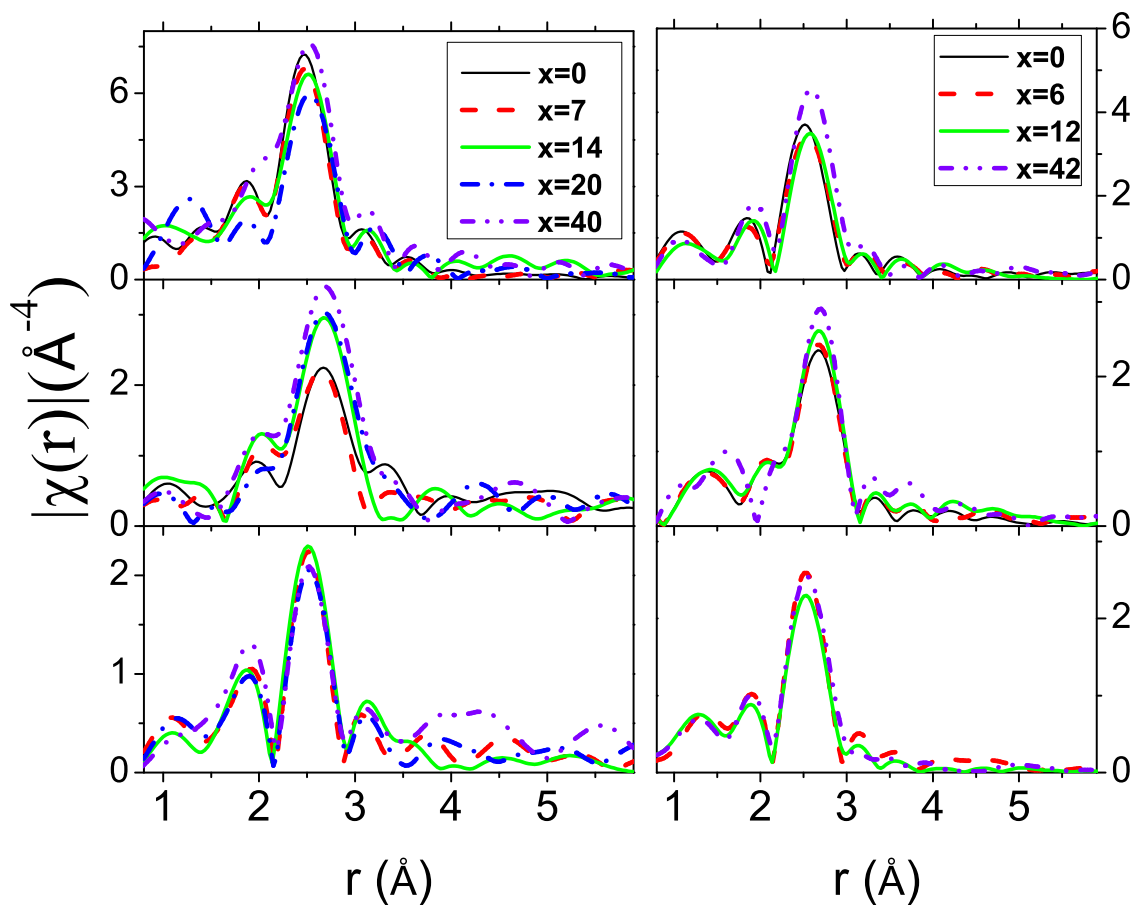
Figure 8.2: Magnitude of k^3 weighted $\chi(r)$ spectra(uncorrected for phase shift) as a function of Ag concentration. k ranges chosen for the Fourier Transform are; $3\text{-}10\text{Å}^{-1}$ for Ge K-edge spectra (top left), $4\text{-}10\text{Å}^{-1}$ for Sb K-edge spectra(middle left) and $2\text{-}10\text{Å}^{-1}$ for Ag K-edge spectra(bottom left). Figures on the right are the $\chi(r)$ spectra obtained from the FEFF simulations at 300K.

In Ag-doped a-$Ag_{0.5}Ge_2Sb_2Te_5$ the average Ge-Te bond length increases with Ag concentration while other bonds (mainly Sb-Te and Ag-Te) remain unchanged. These experimental results are consistent with both the EXAFS simulations based on the models as well as the direct partial pair correlation functions (PPCF) analysis (Fig. 8.3). The
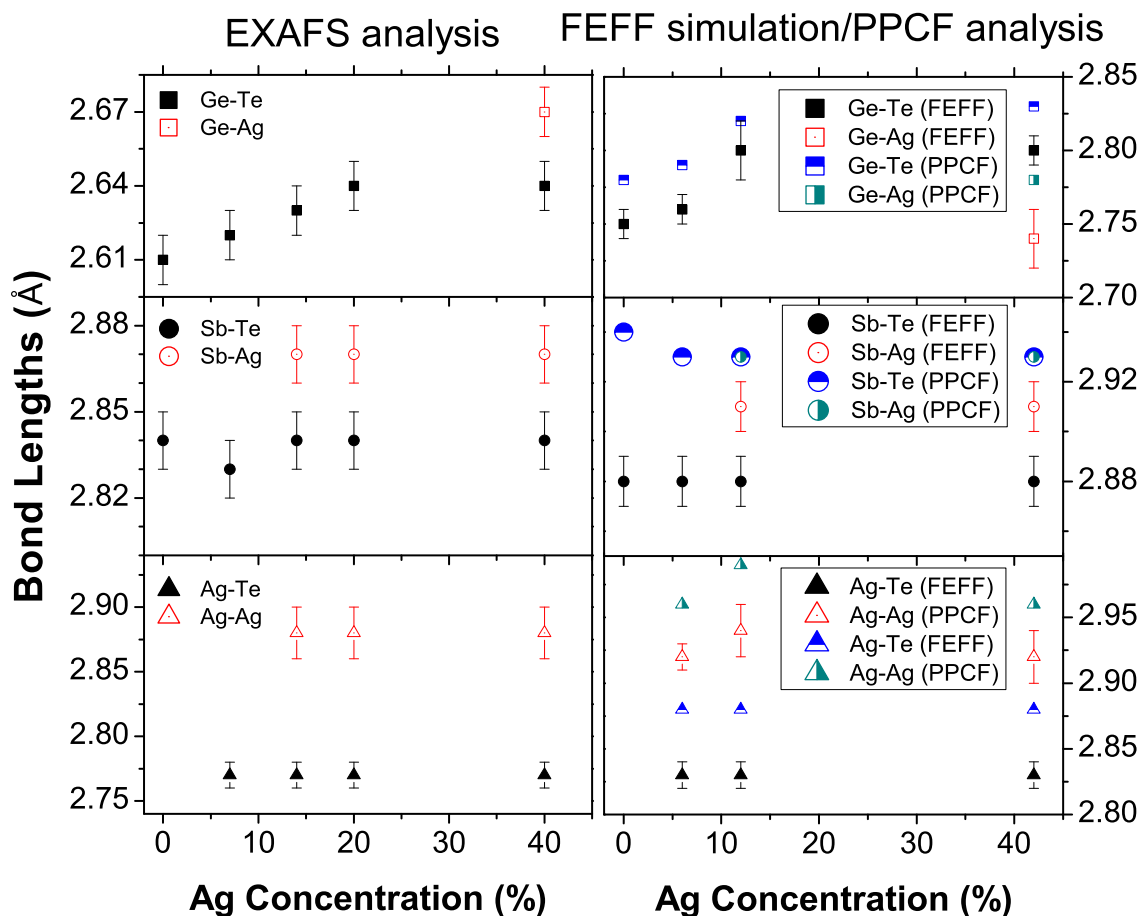
Figure 8.3: Comparison of bond lengths obtained from EXAFS analysis (left) and FEFF/MD simulations (right).

change in Ge-Te bond length can be linked to the change in the fraction of Ge in tetrahedral environment with shorter Ge-Te bond distribution. Ge has two environments (defective octahedral with longer Ge-Te average bond length and tetrahedral with shorter Ge-Te average bond length), as depicted in Ge-centered bond angle distribution(see Fig. 8.4(b) and Ref. [94]). When $Ag_{0.5}Ge_2Sb_2Te_5$ is doped with Ag, the Ge environment is significantly modified, so that the fraction of tetrahedrally bonded Ge is reduced as compared to the octahedral (distorted) Ge. The modification to Ge-Te bonding configuration is reflected in the Ge-centered angle distribution (Fig. 8.4(b)) where the

suppression of the peak near 110° can be observed. Furthermore, the significant variation in the bond angle distribution explains the rearrangement of Ge atoms that could otherwise occupy tetrahedral sites. The modification of the tetrahedral geometry can also be explained through the local order parameter [94, 108] q given by,

$$q = 1 - \frac{3}{8} \sum_i \sum_{k>i} \left(\frac{1}{3} + cos\theta_{ijk} \right)^2 \tag{8.1}$$

in which the sum runs over the nearest neighbors of the central atom j. Figure 8.5(a) presents the distribution of q for Ge atoms. q = 1 represents the ideal tetrahedral geometry whereas q=0 represents the perfect octahedral site. It is also clear from the figure that the fraction of tetrahedral Ge is reduced in consistent with the bond angle distributions. The increase in the fraction of Ge atoms in the distorted octahedral sites relative to that in tetrahedral sites explains the increase in average Ge-Te bond length. This increase could yield the faster crystallization when the GST alloy is doped with Ag, as the octahedral Ge is believed to be one of the members of square rings which are known as ``seeds´´of crystallization[86]. Faster crystallization induced by Ag doping of GST was previously reported experimentally by Song *et al.* [101].

(a)   (b)
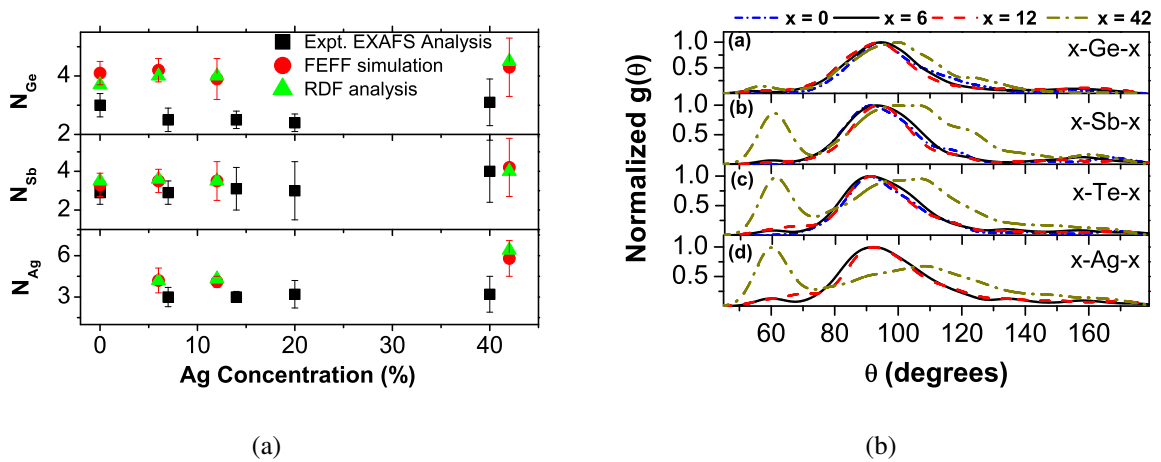
Figure 8.4: a) Coordination numbers and b) Normalized Bond angle distributions in a-$(Ge_1Sb_2Te_4)_{\frac{100-x}{7}}Ag_x$ samples and models.

(a)   (b)
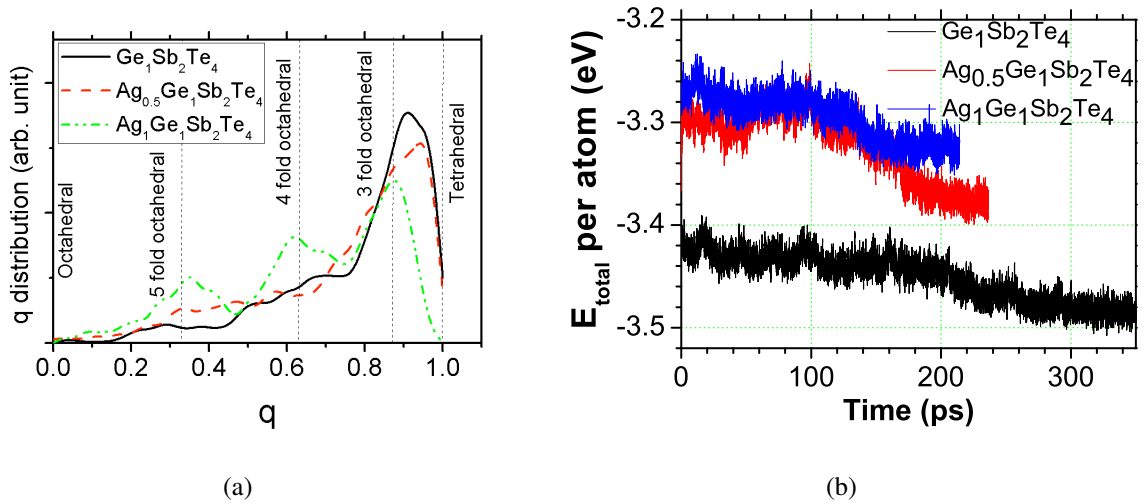
Figure 8.5:   a) Distribution of the local order parameter q for Ge in $Ag_{0.5}Ge_2Sb_2Te_5$, $Ag_{0.5}Ag_{0.5}Ge_2Sb_2Te_5$ and $Ag_1Ag_{0.5}Ge_2Sb_2Te_5$. A cut-off distance of 3.2Å was chosen. b) Time evolution of the total energy of Ag doped $Ag_{0.5}Ge_2Sb_2Te_5$ at 650K, showing a transition from the amorphous to crystalline state.

The speed of crystallization of Ag doped a-$Ag_{0.5}Ge_2Sb_2Te_5$ was analyzed from AIMD simulations. Fig.9.8 shows the time evolution of the total energy of Ag doped and undoped $Ag_{0.5}Ge_2Sb_2Te_5$ (up to 12%) at 650K. An abrupt reduction in the total energy is observed, which is associated with the amorphous-crystalline transition. The time associated with the transition is inversely proportional to the speed of the transition. The time associated with the transition is inversely proportional to the speed of the transition. The estimated crystallization time in the three models with Ag concentrations of 0%, 6%, and 12% are 330, 220, and 160 ps respectively. It is clear that Ag doping increases the speed of the phase transition. The faster crystallization of Ag-doped $Ge_2Sb_2Te_5$ is also reported by Prasai *et al.* from AIMD simulations[23].

We computed mean squared displacements (MSDs) for Ag atoms throughout the crystallization process of Ag-doped $Ag_{0.5}Ge_2Sb_2Te_5$ and present the results in Figure 8.6. The MSDs of transition metals such as Zn in $Ge_2Sb_2Te_5$ have been reported by Skelton et al.[109], where they observed large fluctuation in the MSDs even after crystallization

however only a single Zn dopant was studied. Figure 8.6 clearly shows contrast MSDs among individual Ag atoms. We observe the local geometry of Ag atoms with the least, intermediate, and the highest diffusion as shown in Figure 8.6 a-c. As one might suppose, the highest diffusion is observed for the Ag with low coordination numbers whereas the least diffusion correspond to the Ag with octahedral geometry. As seen in Figure 8.6a-c, after achieving the octahedral geometry Ag becomes less diffusive.

In the case of Sb environment, there is almost no change in the Sb-centered bond angle distributions (up to 12% of Ag) confirming that the doping of Ag does not modify the Sb environment significantly. The experimental and the theoretical analysis of the coordination numbers of Ge (N_{Ge}) and Sb (N_{Sb}) show that they are almost unchanged except for the sample doped with a very high Ag concentration of 42% (Fig. 8.4(a)).

Table 8.1: Ag coordination numbers obtained by integrating Ag PPCF in simulated Ag doped $Ag_{0.5}Ge_2Sb_2Te_5$ models. A cut off minimum of 3.2 Å was used.

x (in%)	Ag-Ge	Ag-Sb	Ag-Te	Ag-Ag
6	–	0.6	3.6	0.4
12	0.1	0.4	3.2	0.7
42	0.3	1.0	2.4	3.0

Both the EXAFS and PPCF analysis confirmed that Ag is mainly bonded to Te rather than Ge and Sb. From the coordination analysis (see Table 8.1) of Ag, we found that the Ag-Te bonds (ignoring Ag-Ag bonds) count for 86%, 86% and 65% of the total bonds for Ag concentration of 6%, 12% and 42% respectively. Ag although prefers bonding with Te, the fraction of Ag-Te is observed to decrease as more Ag is added to the glass network due to reduced fraction of Te atoms. At the highest Ag concentration, Ag-Ag bonds start to dominate Ag-X (X=Ge,Sb and Te) bonds.

The coordination numbers show noticeable change for all species when the Ag concentration in $Ag_{0.5}Ge_2Sb_2Te_5$ is high (42%). These high coordination numbers for all the species cause significant modifications in the bond angle distributions as observed in Fig. 8.4(b). The appearance of a peak at 60° is mainly due to the species bonded with Ag. The Ge-Ag, Sb-Ag, Te-Ag and Ag-Ag coordination numbers all increase significantly for high concentration Ag doped samples whereas Ge-Te and Sb-Te coordination number are found to decrease. The Ag coordination number of 6.7 and bond angle distribution explains the formation of Ag cluster when Ag content is very high in $Ag_{0.5}Ge_2Sb_2Te_5$.

8.4   Conclusion

In conclusion, both experimental and theoretical studies of Ag doped $Ag_{0.5}Ge_2Sb_2Te_5$ have revealed that the average Ge-Te bond length increases with Ag concentration, whereas the Sb-Te and Ag-Te bond lengths remain unchanged. The increase in the fraction of distorted octahedral Ge sites explains the net increase in Ge-Te bond lengths, and appears to be responsible for the faster crystallization of Ge-Sb-Te alloys caused by doping as confirmed by our AIMD simulations. Furthermore, the high fraction of (N_{Ag-Te}) as compared to (N_{Ag-Ge}) and (N_{Ag-Sb}) suggests that Ag prefers bonding with Te to Ge and Sb. Our study sheds light on the atomistic mechanism of rapid crystallization of GST alloys enhanced by Ag doping.
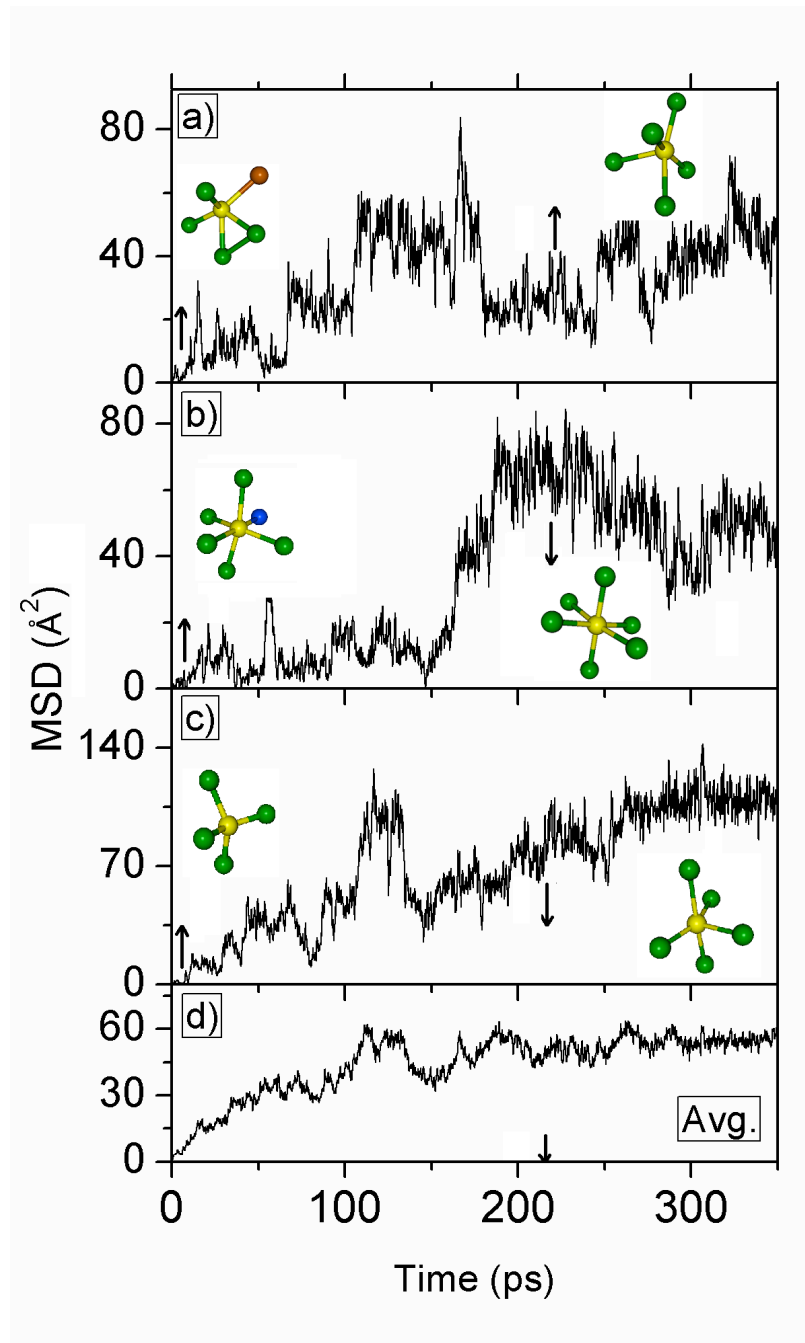
Figure 8.6: Dynamics of Ag atoms in $Ag_{0.5}Ag_{0.5}Ge_2Sb_2Te_5$ before and after crystallization. Ag atoms display significant variation in MSDs depending on the local geometry. Hopping of Ag atoms is observed for low coordinated Ag (c). In contrast, Ag with octahedral geometry does not show significant movement. The vertical arrow in (d) represents the point after complete crystalliza-tion. In (a-c) the structures correspond to the configurations at times shown by the vertical arrows. Similar Ag MSDs were observed in $Ag_1Ag_{0.5}Ge_2Sb_2Te_5$ and are not presented here.

9 TRANSITION METAL DOPED-$Ge_2Sb_2Te_5$: *Ab-initio* MOLECULAR DYNAMICS STUDY

9.1 Introduction

Phase change materials (PCMs) are becoming one of the leading contenders for use in next generation non-volatile memory technology [19, 88]. Ultrafast reversible switching [110] between amorphous and crystalline states with significantly contrast electrical properties[2, 79], high write endurance [111], low power consumption [111] etc. in PCMs makes them serious candidates for the potential application in phase change random-access memory (PCRAM).

As explained in Section 8.1, GST alloys near the pseudobinary GeTe-Sb_2Te_3 tie line [20] are widely accepted phase-change memory materials (PCMM) for application in optical and electronic memories because of their outstanding switching performance, and efforts have been devoted to improve material properties such as switching speed, phase transition temperature, and thermal stability. Improvement of the material properties by doping or alloying with other elements has been emphasized in Section 8.1 [24]

In this chapter, we extend our exploration of column 11 transition metals (Cu, Ag, and Au) to investigate the effect on the properties of $Ge_2Sb_2Te_5$ due to doping with this metals.

9.2 Methods

Ab-initio molecular dynamic (AIMD) simulations were implemented to study the atomistic origin of ultrafast crystallization of $Ge_2Sb_2Te_5$ in the presence of dopants. The AIMD calculations were performed using Vienna *Ab-initio* Simulation Package (VASP)[45–47] to generate models of $Ge_2Sb_2Te_5$ and $X_{0.17}Ge_2Sb_2Te_5$. Each of the

models was created in a cubic supercell with 108(24 Ge atoms, 24 Sb atoms and 60 Te atoms) host atoms and two dopant atoms.

The final models were prepared by using the ``Melt and Quench´´ method[51] starting with a random configuration at 3000 K. After mixing the random configurations at 3000 K for 25 ps, each model was cooled to 1200 K in 10 ps and equilibrated for 60 ps in the liquid state at 1200 K. A cooling rate of 12 K/ps was adopted to obtain the amorphous models from the melt at 1200 K to 300 K and followed by equilibration at 300 K for another 50 ps. Each of these models was then annealed at 650 K up to 450 ps to observe the crystallization. The density 6.05 g/cm^3, that is intermediate between the amorphous and crystalline densities was chosen for undoped Ge$_2$Sb$_2$Te$_5$ while due to lack of experimental values, same lattice was chosen for doped Ge$_2$Sb$_2$Te$_5$ with the hope that dopants would take the vacancy sites. The density of each system is shown in Table 9.1, and was fixed during the MD runs while a time step of 5 ps was used.

Table 9.1: Density (in gm cm^{-3}) used in different models. The used densities are compared to the amorphous and crystalline densities that correspond to the densities of fully relaxed models.

Systems	Used	Amorphous	Crystalline
Ge$_2$Sb$_2$Te$_5$	6.05	5.70	6.12
Cu-Ge$_2$Sb$_2$Te$_5$	6.11	5.82	6.20
Ag-Ge$_2$Sb$_2$Te$_5$	6.20	5.94	6.21
Au-Ge$_2$Sb$_2$Te$_5$	6.24	5.88	6.23

To compute the ground state properties, such as electronic densities of states, the models were fully relaxed to a local minimum at 0 pressure allowing the cell shape and volume to vary. The final relaxed densities are illustrated in Table 9.1. Three independent

models were generated for each of the structures to check the consistency of the

simulation results.

The calculations were performed by using the projector augmented-wave

(PAW)[89, 90] method to describe electron-ion interactions. The Perdew-Burke-Ernzerhof

(PBE)[91] exchange correlation functional was used throughout. Molecular-dynamics

(MD) simulations were performed in a cubic supercell using periodic boundary conditions

at constant volume for annealing, equilibrating and cooling, whereas, zero pressure

conjugate gradient (CG) simulations were performed for relaxation. Unless stated

otherwise, both the MD and CG simulations were performed by using the Γ point to

sample the Brillouin zone.

9.3   Structural Properties

There have been a number of reports explaining how a dopant may place itself in the

GST host network [112]. It is therefore interesting to see how these dopants (Cu, Ag, Au)

adapt to the local structure. The atomic structure of a material is studied through a set of

pair correlation functions. As described in section 1.3.1.2 a pair correlation function is a

position distribution function based on the probability of finding atoms at some distance $\vec{r}$

from a central atom.

The pair correlation functions (PCFs) provide local structural information of central

interest for amorphous materials. The peaks in these distribution functions describe the

average distance of the neighboring atoms from a central atom. Since amorphous

materials do not possess long range order, $g(r) \rightarrow 1$ as $r \rightarrow \infty$. For crystalline structures,

g(r) is a sum of delta functions, with each term coming from a coordination shell. The pair

function which can provide results of diffraction experiments via Fourier transformation,

yield crucial information about the short-range order and the nature of chemical bonding.

For systems with more than one species, the structural correlations are usually investigated through partial pair correlation functions. In addition to local bonding, integration of the PCF up to the first minimum provides information on averaged coordination numbers. Coordination statistics shed light on the local topology for an atomic type. Coordination number analysis is particularly interesting in these materials since the number changes from six in the crystalline phase (rocksalt structure) to about four in the amorphous phase. Is should also be pointed out that the information obtained from the PCF alone may not sufficient enough to describe the local structure and hence require an introduction of other distribution functions like bond angle distributions (BADs). BAD would lead relevant insight in order to study the local environment of each of impurity atoms and network structure of doped phase change materials.

Since crystalline $Ge_2Sb_2Te_5$ contains 20% vacant octahedral sites, these vacant sites would seem to be an ideal place for the dopant atoms to occupy. However, as there is no well known definition of vacancy (vacancies may cluster to form voids) in the amorphous phase, the local structure of the dopant atoms in the amorphous phase is even more interesting to investigate. The local structures of the dopants are presented in Fig. 9.1. Fig. 9.1(a-f) represent the local structures of the dopants in amorphous phase while the bottom half (Fig.9.1(g-l)) represent the structures in crystalline phase. The bonding information is investigated through partial pair correlations function (PPCFs). Fig. 9.2 presents a set of PPCFs corresponding to different dopant atoms. At about 2% of dopants (impurities), there is no major change in pair correlation functions in both amorphous and crystalline phases. As the position of first maximum in the PPCF reflects the average bond lengths, we were able to estimate the average bond lengths and present them in Table 9.2. We observed no dopant-induced change in Ge-Te and Sb-Te average bond lengths in the amorphous phase whereas the change in Ge-Te and Sb-Te average bond lengths in crystalline phase is also negligible being within the uncertainty of ~ 0.01 Å. On the other

hand, Cu-Te average bond length is observed to be the shortest while Ag-Te average bond length is the longest among the three dopants (Cu, Ag, and Au). To further understand the local topology of the dopants we computed the bond angle distribution (BAD) centered on the dopants and illustrate the results in Fig. 9.3, which clearly shows a large distortion of the BADs in the amorphous phase while the BADs in the crystalline phase illustrate the tendency of the dopants to adopt an octahedral geometry as the host atoms. Among three dopants, Cu is least likely to adopt octahedral geometry as compared to Ag and Au since no peak at around 180° is observed for Cu BAD. The reason could be the shorter Cu-Te bond lengths as compared to Ag-Te and Au-Te bond lengths or the variation of valency of Cu.

| (a) | (b) | (c) | (d) | (e) | (f) |

| (g) | (h) | (i) | (j) | (k) | (l) |
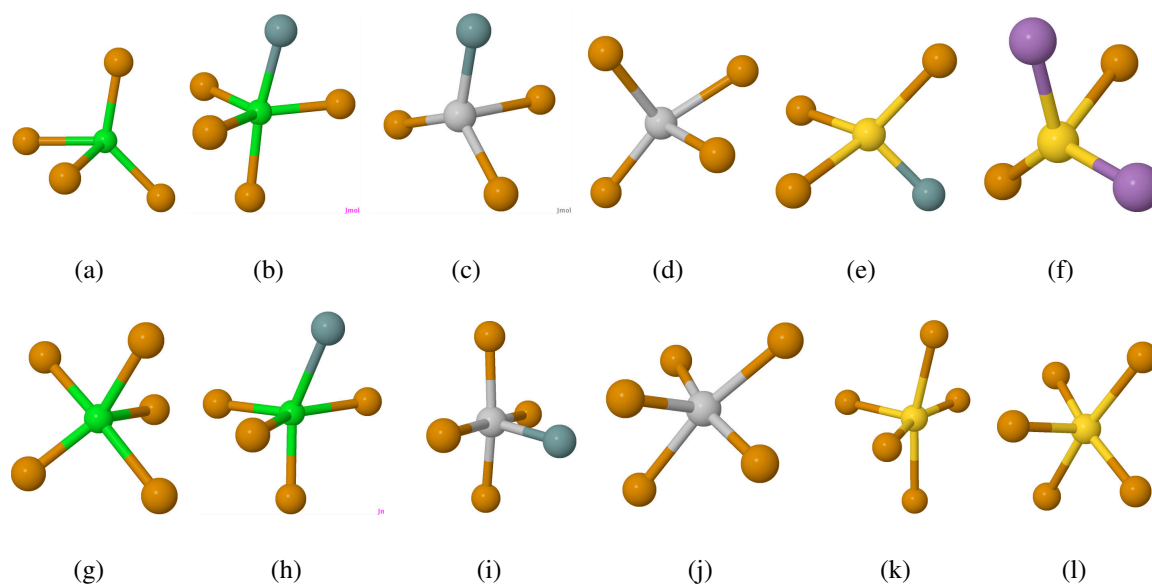
Figure 9.1: Local atomic structures surrounding the dopants. (a,b) Cu, (c,d) Ag, and (e,f) Au local geometries in amorphous phases (top images). The bottom images correspond to structures around the dopants in crystalline phases. Color code: Orange-Te, Blue-Ge, Purple-Sb, Green-Cu, Silver-Ag, Yellow-Au.

One of the interesting features of the GST structure is the coordination number, that ranges from around 4 in the amorphous phase to around 6 in the crystalline phase. To

investigate the dopant effect on these numbers, we computed coordination numbers by integrating the PPCFs up to the first minima and presented in Table 9.3. Among the three dopants, Cu has the highest coordination number relative to Ag and Au. Furthermore, the coordination number of Cu does not change significantly from the amorphous to crystalline phase. Beside this, the coordination numbers of the host species (Ge/Sb/Te) also does not increase significantly as in pure GST or doped with Ag or Au, suggesting that the presence of Cu in the GST might suppress the phase transition reducing the crystallization speed. Au on the other hand tends to show an unusual behaviour with a significant fraction of Ge/Sb atoms as neighbors although Te is the most anionic species, and no Ge/Sb neighbors observed in the crystalline phase. Unlike Cu, the coordination numbers of Au as well as the host species in Au-doped GST increase significantly. Ag also shows some Ag-Ge and Ag-Sb ($< 10\%$) bonds, which persist even to the crystalline phase of Ag-doped GST however, Ag does not suppress the increase in the coordination numbers like Cu. The coordination analysis reveals that the majority of the dopant atoms bond to Te rather than Ge and Sb (see Table 9.3). Cu, Ag, and Au respectively have 88, 90, and 56% of nearest neighbor at Te. Au seems noticeably different that Cu or Ag with only 56% Te as neighbor, with high fraction Ge and Sb as nearest neighbors. This contrast is interesting, since all three elements lie on the same column of the periodic table and might be expected to have similar coordination. To further explore the coordination, we computed the average atomic charge on the dopant atoms using a Bader charge analysis [113–115] and present results in Table 9.4. We observe similar atomic charges for Cu and Ag whereas we obtain a negative charge for Au. The negative charge on Au makes it anionic in nature as a consequence of which a large fraction of Ge and Sb are bonded to Au. The atomic charge on Au becomes significantly less negative in the crystalline phase and consequently the fraction of Ge and Sb as neighbors drops. We further analyze the average atomic charge on Au during the crystallization of Au-doped $Ge_2Sb_2Te_5$. Fig. 9.4

presents the time evolution of the average atomic charge on Au along with the nearest neighbors of Au within the first coordination shell. The fraction of Ge/Sb neighbors decreases while increasing the fraction of Te neighbors as the charge on Au decreases.

Beside Ge-Te, Sb-Te and X-Te (X=Cu, Ag, and Au) bonds, there exists a significant number of other bond pairs such as homopolar bonds, Ge-Sb, Ge-X, and Sb-X bonds which are also termed as "wrong bonds" (Fig.9.2(e and j)). About 14% of the total bond pairs corresponds to the wrong bonds (WB) in the amorphous phase whereas about 5% of wrong bonds persist in the crystalline phase.

Table 9.2: Average bond lengths in amorphous and crystalline phases of pure and doped $Ge_2Sb_2Te_5$.

Bonds	Dopant	Amorphous	Crystalline
Ge-Te	–	2.78	2.92
	Cu	2.78	2.91
	Ag	2.78	2.92
	Au	2.78	2.92
Sb-Te	–	2.96	3.02
	Cu	2.96	3.00
	Ag	2.96	3.02
	Au	2.96	3.02
Cu-Te	Cu	2.59	2.62
Ag-Te	Ag	2.82	2.88
Au-Te	Au	2.72	2.78

Table 9.3: Comparison of coordination numbers in amorphous and crystalline phases of pure and doped $Ge_2Sb_2Te_5$. A cut off distance of 3.2Å was chosen for the integration of the first peak of PPCF.

Species	Dopant	Amorphous					Crystalline				
		Ge	Sb	Te	X	Total	Ge	Sb	Te	X	Total
Ge	–	0.4	0.3	3.5	-	4.2	-	0.1	5.4	-	5.5
	Cu	0.2	0.3	3.8	-	4.3	-	0.1	4.6	-	4.7
	Ag	0.1	0.5	3.2	-	3.8	0.1	0.2	5.1	-	5.4
	Au	0.4	0.2	3.6	-	4.2	0.1	-	5.0	-	5.1
Sb	–	0.3	0.5	2.8	-	3.6	0.1	0.3	5.2	-	5.6
	Cu	0.3	0.7	2.7	-	3.7	0.1	0.5	4.2	-	4.8
	Ag	0.5	0.6	2.6	-	3.7	0.2	0.1	4.9	-	5.2
	Au	0.2	0.5	2.9	0.1	3.7	-	0.3	4.7	-	5.0
Te	–	1.4	1.1	0.2	-	2.7	2.2	2.1	0.2	-	4.5
	Cu	1.5	1.1	0.4	0.1	3.1	1.8	1.7	0.2	0.1	3.8
	Ag	1.3	1.0	0.4	0.1	2.8	2.0	2.0	0.2	0.2	4.4
	Au	1.5	1.1	0.3	0.1	3.0	1.8	1.7	0.2	0.1	3.8
Cu	Cu	0.6	-	4.2	-	4.8	0.5	-	4.5	-	5.0
Ag	Ag	0.3	0.1	3.5	-	3.9	0.3	0.2	4.5	-	5.0
Au	Au	0.5	1.0	1.9	-	3.4	-	-	5.2	-	5.2

9.4 Electronic and Optical Properties

Practical utilization of GST materials depends upon a substantial optical or electrical contrast between the amorphous and crystalline phases. As both the resistivity and optical absorption depend upon the electronic structures of materials, it is necessary to investigate the influence of dopants on the electronic structure of the host network.

Table 9.4: Computed average atomic charges on the dopant atoms in relaxed amorphous and crystalline phases of Cu, Ag, and Au doped $Ge_2Sb_2Te_5$. The charges are in the unit of e.

Dopants	Amorphous	Crystalline	Change
Cu	0.16	0.12	25%
Ag	0.14	0.08	43%
Au	-0.44	-0.28	36%

The electronic structure is usually described by analyzing the electronic density of states (EDOS), projected density of states (PDOS), and/or inverse participation ratio (IPR) of each individual site.

To investigate the effect of dopants on the electronic properties we computed both the species projected and orbital projected partial density of states (PDOS) and present these in Fig. 9.5(a-e). At ~ 2% dopant level, we were not able to observe significant difference in the total density of states except for slight modificaition at energy range of -5 eV to -1eV below the fermi level. This small change mainly corresponds to the d states of the dopants (Fig. 9.5(d and e)). Among the dopants, Cu d states lie closer to band gap and therefore the presence of Cu may significantly affect the electrical and optical properties. The present calculations were not able to reproduce an experimental band gaps and could be attributed to the fact that DFT is well known to underestimate bandgaps [116].

Furthermore, to observe the influence of dopants on the optical properties of $Ge_2Sb_2Te_5$, we computed the dielectric functions of the pure and doped $Ge_2Sb_2Te_5$. Fig.9.6 presents the imaginary and the real part of the dielectric functions of pure and doped $Ge_2Sb_2Te_5$ in both the amorphous and the crystalline phases. Fig. 9.6 confirms that the addition of Ag or Au does not affect the optical properties by much, still preserving the optical contrast in the visible regions (1 - 3 eV) whereas the addition of Cu does not look

too promising in terms of optical contrast. Table 9.5 presents the optical dielectric

constant, *i.e.*, the lower energy-limit of the real part of the dielectric function ($\omega \to 0$).

The reduction in optical contrast on adding Cu can be attributed the structure of Cu in the

host network. We observe almost no change in the Cu-Te bond lengths as well as the Cu

coordination numbers during the phase transition suggesting Cu very immobile in the host

network. As discussed by Shportko *et al.* [95], the contrast in the optical properties in

PCMM is attributed to a large electronic polarizability in the crystalline phase due to the

resonant (electron deficient) p-bonding. Unlike Ag and Au, Cu is unable to integrated

itself fully into the crystalline structure with octahedral structure (see Fig. 9.1) introducing

a significant structural disorder and hence reducing the contribution to the resonant

bonding. This reduction would cause the decrease in the optical contrast. This inability of

Cu to integrate into the crystalline structure is also reflected in the electronic properties

where we observed Cu d-states much closer to the band gap.

Table 9.5: Comparison of the optical dielectric constant between the two phases of pure
and doped $Ge_2Sb_2Te_5$.

Dopants	Amorphous	Crystalline	Increase %
–	25.9	53.0	105
Cu	26.0	31.7	22
Ag	26.1	54.3	108
Au	28.1	57.7	105

9.5 Crystallization Dynamics

The dopant centered bond angle distributions (Fig.9.3) illustrate the modification of

local geometry of dopants from wide distortion to somehow more ordered octahedral

structures. This makes it possible to observe the atomic motions of dopants during and

after the crystallization of the host network is completed. There have been a few studies on the dynamics of dopants in $Ge_2Sb_2Te_5$ during crystallization [24, 112]. In the simulations with the first row dopants (Sc-Zn), Skelton *et al.* have reported wide a range of atomic motion even after crystallizations [112]; however only one dopant was investigated. In their recent work, Prasai *et al.* investigated the dynamics of Ag in $Ge_2Sb_2Te_5$ with up to 12% of Ag and reported mixed diffusion of Ag ranging from least diffusive to most diffusive. One could expect similar kind of atomic motions for Cu, Ag, and Au dopants studied in this work. We indeed observe similar atomic motion during and after crystallization of host network in the present work as presented in Fig. 9.7. A thorough investigation of atomic diffusion reveals the fact that the dopant atoms becomes less diffusive whenever the atom is close to an octahedral geometry. Fig. 9.7 shows mean squared displacements of each of the dopant atoms during the whole crystallization process. Either Ag or Au atoms show no hopping after the crystallization whereas Cu_{109} shows hopping even after the crystallizations had occurred. The local geometries of the dopant atoms are shown in the Fig. 9.1(a-l). The dopant atom that achieves the octahedral geometry shows no hopping events after the crystallization. The Cu_{109} (one of two Cu atoms) showed the hopping after the crystallization, did not achieve the octahedral geometry. Cu_{109} is represented by Fig. 9.1(a) and 9.1(g) in amorphous and crystalline phases respectively. This can further be verified from the absence of peak around 180° in Fig.9.3.

The speed of crystallization was investigated by observing the time evolution of the total energy of the system(Fig. 9.8). Each of the models was annealed at 650K until crystallized. Based on the evolution of energy, the total crystallization process can be divided into three regions as also explained by Lee *et al.*[96]. In Region I (incubation period), although the total energy does not change, the number of four fold (squared) rings keep increasing forming cubes or planes with random orientations due to thermal

fluctuations [23, 96]. Region II, in which the total energy shows a monotonous decrease, is the main part where the cubes or planes starts arranging themselves in more ordered structures. By the end of this period the energy goes to a minimum and remains constant thereafter reaching Region III where the crystallization is believed to be complete. The duration of Regions I and II shows large fluctuations for three independent models for same structure resulting in significant uncertainty for estimation of crystallization time. These fluctuations are mainly associated with the fraction of wrong bonds present in the amorphous phase as well as the random orientations of the squared rings due to the thermal fluctuations. Table 9.6 presents the average wrong bonds and the crystallization time from three different models of each composition. Although the crystallization periods show large variation, the time of about 400 ps was enough for each of the model to complete crystallization. We may not be able to predict the exact modification on the crystallization speed at this level but it is confirmed that the crystallization speed of the host network is still preserved.

Table 9.6: Computation of wrong bonds and the estimation of the crystallization time in doped ($\sim 2\%$) and undoped $Ge_2Sb_2Te_5$.

Dopant	Wrong bonds in fraction	Incubation period (ps)	Crystallization period ps	Total ps
–	0.13±0.03	150±50	120±40	270±90
Cu	0.14±0.03	180±30	120±45	300±75
Ag	0.15±0.04	130±40	100±20	230±60
Au	0.14±0.04	170±50	120±30	290±80

9.6 Conclusion

We used plane wave molecular dynamic simulations to study the crystallization behavior of Ge-Sb-Te phase change alloys in presence of transitions metals (Cu, Ag, and Au) as impurities. We were successfully able to simulate the ultrafast phase transitions from amorphous to crystalline phase through the MD simulations. At ~ 2% of impurities, we did not observe any significant dopant-induced structural change in Ge-Te or Sb-Te average bond lengths. Meanwhile the Bader charge analysis confirmed similar positive charge for Cu and Ag whereas negative charge for Au as a consequence Au was observed to have significant amount of Ge/Sb as neighbors. The estimation of dielectric constant in amorphous and crystalline phase implies that the optical contrast is preserved in Ag or Au doped $Ge_2Sb_2Te_5$ while Cu doped $(Ge_1Sb_2Te_4)_{\frac{100-x}{7}}Ag_x$ did not look too promising in terms of optical contrast. We were also able to estimate the crystallization time for the transition metal doped $(Ge_1Sb_2Te_4)_{\frac{100-x}{7}}Ag_x$ however with large variations which may be attributed to the presence of WB in the system.
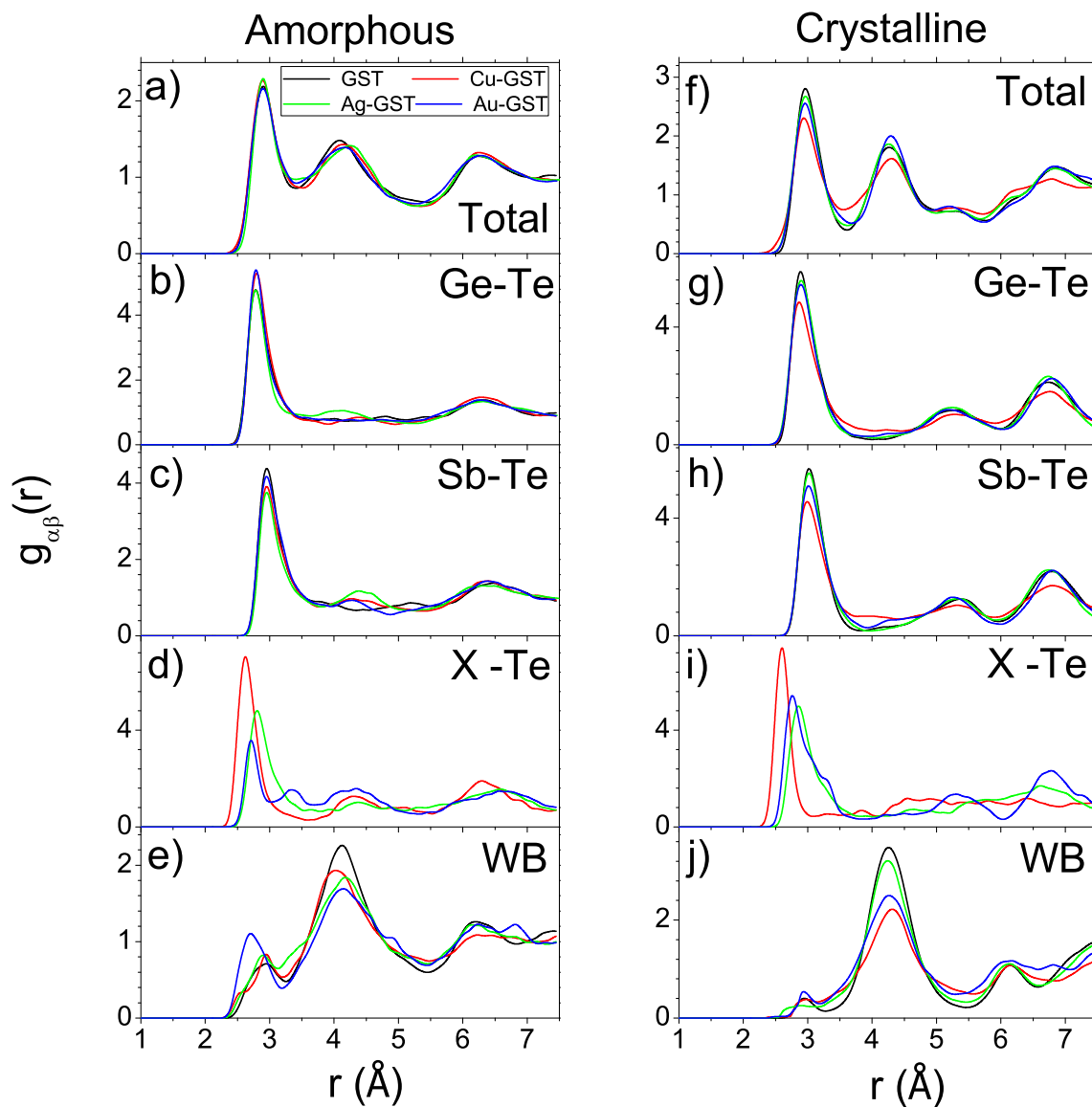
Figure 9.2: Pair correlation functions at 300K for pure and doped $Ge_2Sb_2Te_5$. Partial pair correlation functions for amorphous structures are on the left (a-e) and for crystalline structures are on the right (f-j).
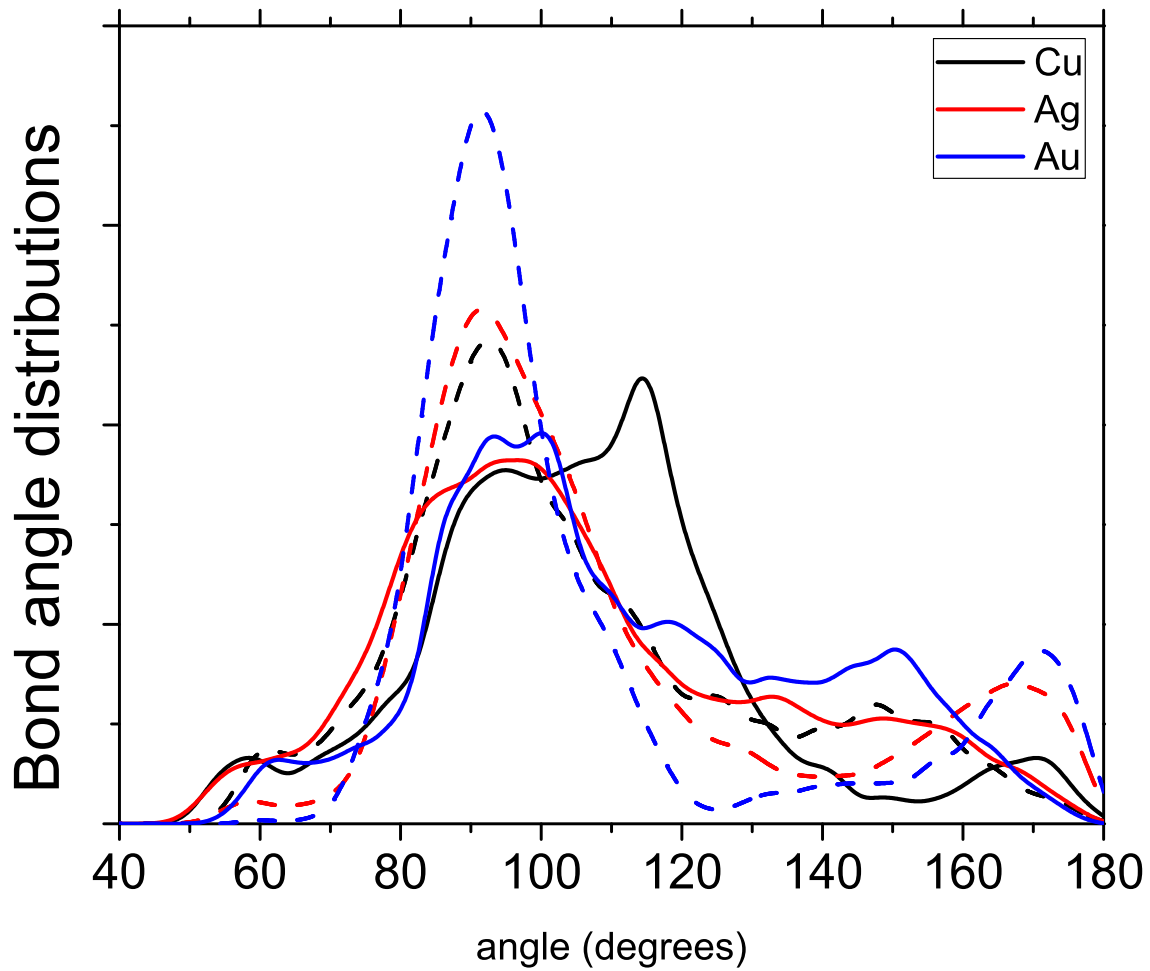
Figure 9.3: Bond angle distributions around the dopants at 300K for doped $Ge_2Sb_2Te_5$.
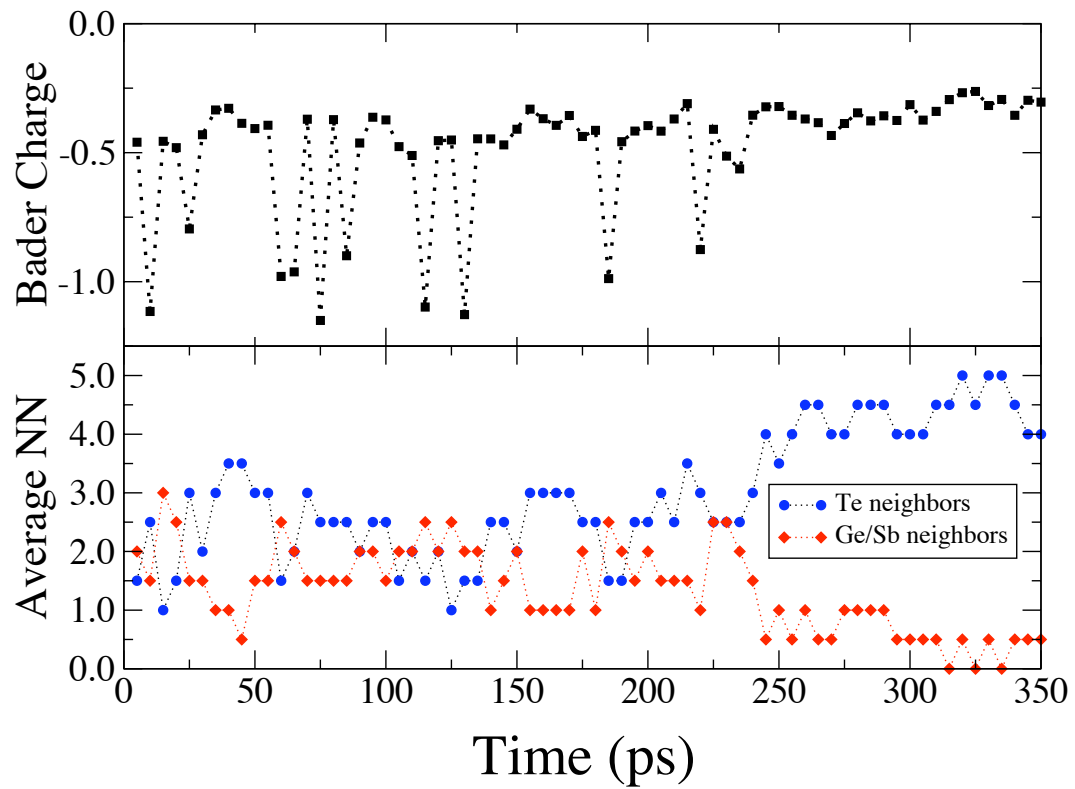
Figure 9.4: Evolution of the average charge on Au during crystallization of Au-doped $Ge_2Sb_2Te_5$. The number of nearest neighbors in the first coordination shell is presented for comparison.
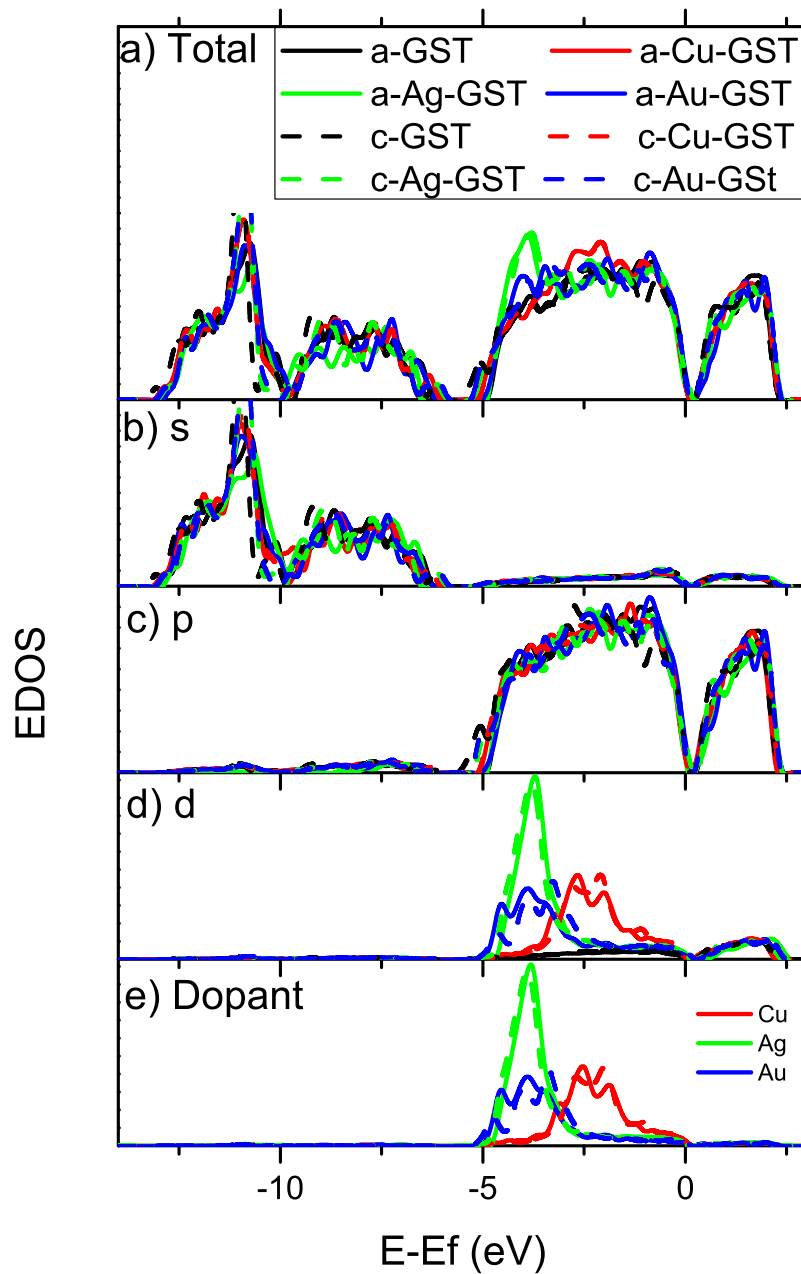
Figure 9.5: Comparison of partial density of states (PDOS) for different dopants in Ge$_2$Sb$_2$Te$_5$. The Fermi level is set to 0 eV.
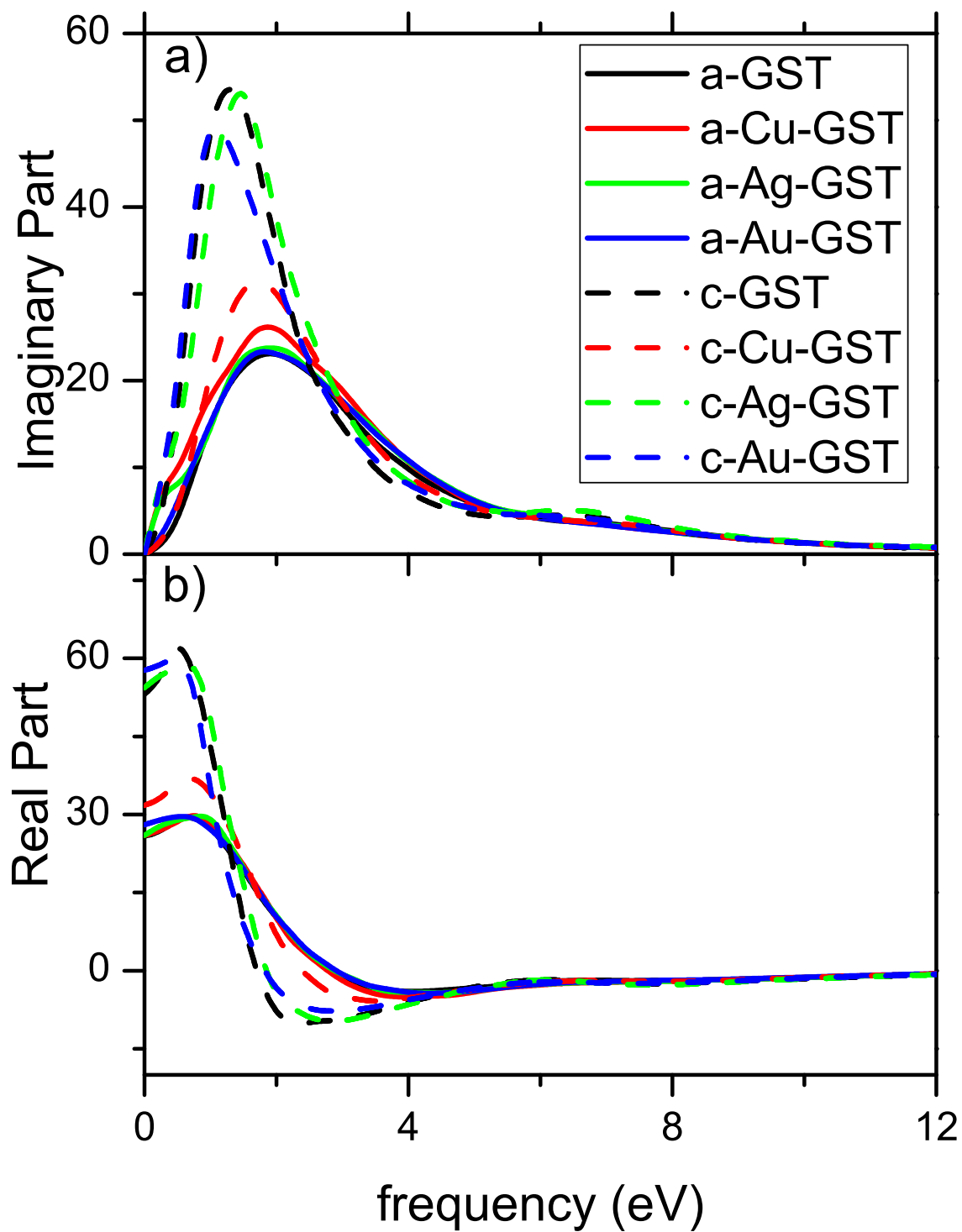
Figure 9.6: Comparison of optical contrast in Cu, Ag, and Au doped $Ge_2Sb_2Te_5$.
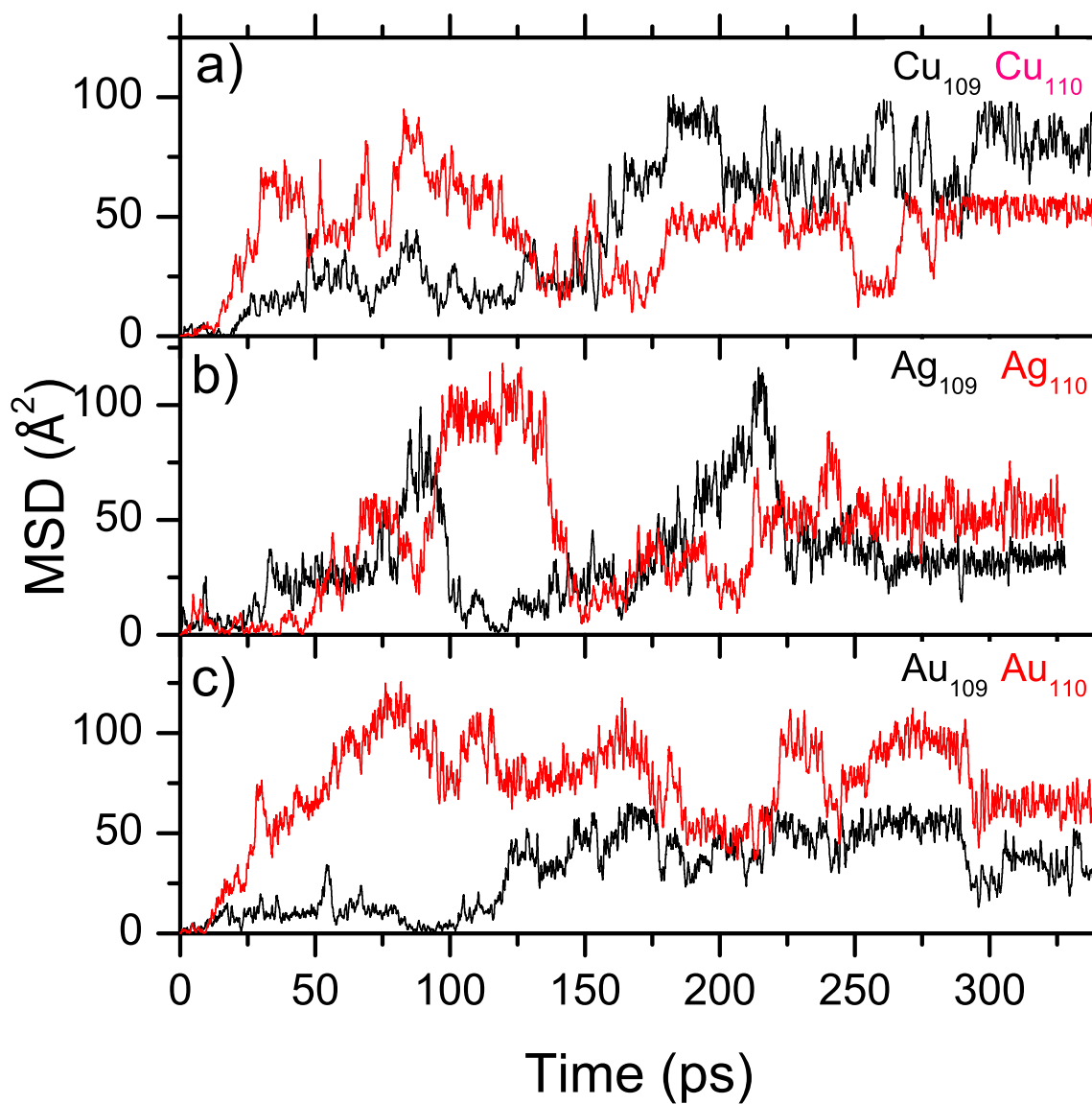
Figure 9.7: Mean squared displacements (MSD) of dopants during the crystallization process.
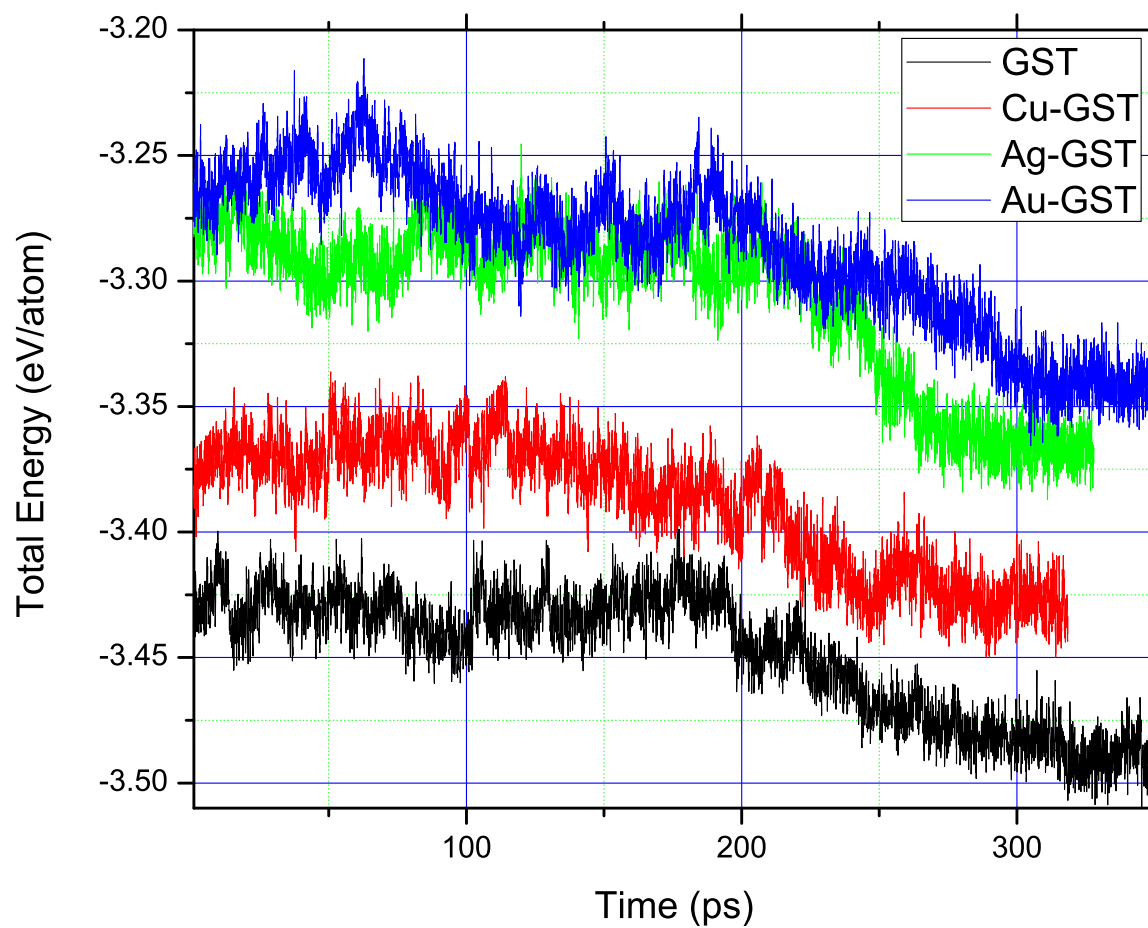
Figure 9.8: Evolution of total energy in pure and doped Ge$_2$Sb$_2$Te$_5$ annealed at 650K. The drop in the total energy represents the crystallization.

10   Concluding Remarks and Future Considerations

10.1   Conlusion

In this work, we have successfully presented study of extensive properties of chalcogenide materials using a large scale computer simulations and x-ray absorption spectroscopy. We were able to produce realistic models of Ge-Se-Ag/Cu glasses, TiO_2, Ge-Sb-Te alloys,and transition metal doped Ge-Sb-Te alloys using a method of melt and quench. A detailed computational analysis on Ge-Se-Ag/Cu glasses confirmed the high ionic conductivity of Ag in Ge-Se glasses whereas Cu is observed to have relatively lower conductivity with Cu mostly trapped. Computational models of amorphous and crystalline TiO_2 showed that amorphous TiO_2 resembles anatase TiO_2 in many respects. Computer simulations of ultrafast phase transition of Ge-Sb-Te were successfully observed. Both the experimental and theoretical study of Ag-doped Ge-Sb-Te alloys revealed that Ag enhances the crystallization speed in Ge-Sb-Te host. On the other hand, in comparison among the dopants Cu, Ag and Au, Cu and Au causes the crystallization relatively slower as compared to Ag.

10.2   Future consideration

Because of high ionic conduction, Ag doped Ge-Se electrolyte glasses are potential candidates for fast operating devices like conductive bridge memory devices. However, one of the drawbacks of the devices formed from these materials is the lack of ability to tolerate processing condition much beyond 200^oC. One of the solutions for this is to replace Se by S since sulfide based solid electrolyte materials have excellent thermal stability and are able to withstand the elevated temperatures[1]. Given that there are many similarities between S and Se glasses we would expect similar ionic conduction in both S and Se base glasses. However, it is known that the conductivity of GeSeAg and GeSAg materials are very different. This difference with sulfides having a conductivity two-three

orders of magnitude lower than the selenides is a difficult and interesting problem to understand.

GST based PCMM are already in use as non-volatile memory materials making them an excellent alternative to the current flash memory technology. The next goal is to use GST in high-density memory chips that requires the down-sizing of these particles into nanostructure. It is necessary to study the structures and properties (e.g. optical and electrical properties) of these nanostructured PCMM.

11 PUBLICATIONS

11.1 Peer Reviewed Journals

1. **B. Prasai** and D. A. Drabold (2011), *Ab initio simulation of solid electrolyte materials in liquid and glassy phases*, Phy. Rev. B, **83**, 094202 (2011).

2. **B. Prasai**, B Cai, M. Kylee Underwood, James P. Lewis, and D. A. Drabold (2011). *Ab-initio Calculation of Structural and Electrical Properties of Amorphous TiO2*, Proceedings: Glass and Optical Materials, MS&T Publications Department.

3. **B. Prasai**, B Cai, M. Kylee Underwood, James P. Lewis, and D. A. Drabold (2012) *Properties of amorphous and crystalline titanium dioxide from first principles*, Journal of Materials Science, **47**, 7515-7521(2012).

4. **B. Prasai**, G. Chen, and D. A. Drabold (2013). *Direct ab-initio molecular dynamic study of ultrafast phase change in Ag-alloyed Ge2Sb2Te5*, Applied Physics Letters, **102**, 041907 (2013).

5. **B. Prasai**, M.E. Kordesch, D. A. Drabold, and G. Chen (2013) *Atomistic origin of doping-enhanced rapid crystallization in Ag-doped Ge-Sb-Te alloys: a joint experimental and theoretical study*. Phy. Status Solidi B, 1-6 (2013).

11.2 Book Chapters

1. B. Cai, **B. Prasai**, and D.A. Drabold (2011) *Atomistic Simulations of Flash Memory Materials Based on Chalcogenide Glasses.*, Flash Memories, Prof. Igor Stievano (Ed.), (pp. 241-263). ISBN: 978-953-307-272-2, InTech.

REFERENCES

[1] M Mitkova and M.N Kozicki. Silver incorporation in *Ge–Se* glasses used in programmable metallization cell devices. *Journal of Non-Crystalline Solids*, 299–302, Part 2(0):1023 – 1027, 2002. 19th International Conference on Amorphous and Microcrystalline Semiconductors.

[2] S. R. Ovshinsky. Non-crystalline materials for optoelectronics. *edited by G. Lucovsky and M. Popescu*, 2004.

[3] M Mitkova. Amorphous semiconductors and insulators. *edited by P. Boolchand.*, page 813, 2000.

[4] E. A. Stern. *X-ray Absorption, Principles, Applications, Techniques of EXAFS, SEXAFS and XANES. edited by D.C Koningsberger and R. Prins*, pages 3–17, 1988.

[5] B. K. Teo. *EXAFS*: Basic principles and data analysis. *Inorganic Chemistry Concepts*, 9, 1986.

[6] B. Ravel and M. Newville. *ATHENA, ARTEMIS, HEPHAESTUS*: data analysis for *X*-ray absorption spectroscopy using *IFEFFIT*. *J. Synchrotron Rad.*, 12:537–541, 2005.

[7] A. L. Ankudinov, B. Ravel, J. J. Rehr, and S. D. Conradson. Real-space multiple-scattering calculation and interpretation of x-ray-absorption near-edge structure. *Phys. Rev. B*, 58:7565–7576, Sep 1998.

[8] N. E. Cusack. The physics of structurally disordered matter: An introduction. *edited by Douglas F. Brewer and D. Phil*, pages 30–36, 1987.

[9] Raymond Atta-Fynn, Parthapratim Biswas, and D. A. Drabold. Electron–phonon coupling is large for localized states. *Phys. Rev. B*, 69:245204, Jun 2004.

[10] David Chandler. in introduction to modern statistical mechanics. *Oxford University Press, New York*, pages 249–250, 1987.

[11] R. Azoulay, H. Thibierge, and A. Brenac. Devitrification characteristics of Ge_xSe_{1-x} glasses. *Journal of Non-Crystalline Solids*, 18(1):33 – 53, 1975.

[12] M.F. Thorpe, D.J. Jacobs, M.V. Chubynsky, and J.C. Phillips. Self-organization in network glasses. *Journal of Non-Crystalline Solids*, 266-269:859–866, 2000.

[13] P. Boolchand, D. G. Georgiev, and B. Goodman. Discovery of the intermediate phase in chalcogenide glasses. *J. Optoelectron. Adv. Mater.*, 3:703, 2001.

[14] Andrea Piarristeguy, Marcela Mirandou, Marcelo Fontana, and Bibiana Arcondo. X-ray analysis of *GeSeAg* glasses. *Journal of Non-Crystalline Solids*, 273(1–3):30 – 35, 2000.

[15] Roger J. Dejus, Sherman Susman, Kenneth J. Volin, Daniel G. Montague, and David L. Price. Structure of vitreous *AgGeSe*. *Journal of Non-Crystalline Solids*, 143(0):162 – 180, 1992.

[16] G.J. Cuello, A.A. Piarristeguy, A. Fernandez-Martinez, M. Fontana, and A. Pradel. Structure of chalcogenide glasses by neutron diffraction. *Journal of Non-Crystalline Solids*, 353(8–10):729 – 732, 2007.

[17] B. Prasai and D. A. Drabold. *Ab initio* simulation of solid electrolyte materials in liquid and glassy phases. *Phys. Rev. B*, 83:094202, Mar 2011.

[18] De Nyago Tafen, D. A. Drabold, and M. Mitkova. Silver transport in $Ge_xSe_{1-x} : Ag$ materials: *Ab initio* simulation of a solid electrolyte. *Phys. Rev. B*, 72:054206, Aug 2005.

[19] Matthias Wuttig and Noboru Yamada. Phase-change materials for rewriteable data storage. *Nature Mater.*, 6:824–832, 2007.

[20] Noboru Yamada, Eiji Ohno, Kenichi Nishiuchi, Nobuo Akahira, and Masatoshi Takao. Rapid-phase transitions of $GeTe - Sb_2Te_3$ pseudobinary amorphous thin films for an optical disk memory. *J. Appl. Phys.*, 69:2849, 1991.

[21] J. M. van Eijk. Structural analysis of phase-change materials using x-ray absorption measurements (dissertation). *RWTH Aachen University*, 2010.

[22] B. Prasai, B. Cai, M. K. Underwood, J. P. Lewis, and A. D. Drabold. Properties of amorphous and crystalline titanium dioxide from first principles. *J. Phys. Cond. Matter.*, 47:7515–7521, 2012.

[23] B. Prasai, G. Chen, and D. A. Drabold. Direct *ab-initio* molecular dynamic study of ultrafast phase change in Ag-alloyed $Ge_2Sb_2Te_5$. *Appl. Phys. Lett.*, 102, 2013.

[24] B. Prasai, M. E. Kordesch, D. A. Drabold, and G. Chen. Atomistic origin of rapid crystallization of *Ag*-doped *Ge-Sb-Te* alloys: A joint experimental and theoretical study. *Phys. Stat. Sol. b.*, 102:1–6, 2013.

[25] P. Hohenberg and W. Kohn. Inhomogeneous electron gas. *Phys. Rev.*, 136:B864–B871, Nov 1964.

[26] W. Kohn and L. J. Sham. Self-consistent equations including exchange and correlation effects. *Phys. Rev.*, 140:A1133–A1138, Nov 1965.

[27] R. Car and M. Parrinello. Unified approach for molecular dynamics and density-functional theory. *Phys. Rev. Lett.*, 55:2471–2474, Nov 1985.

[28] Otto F. Sankey and David J. Niklewski. *Ab initio* multicenter tight-binding model for molecular-dynamics simulations and other applications in covalent systems. *Phys. Rev. B*, 40:3979–3995, Aug 1989.

[29] Peter Schwerdtfeger. The pseudopotential approximation in electronic structure theory. *ChemPhysChem*, 12:3143–3155, December 2011.

[30] Akira Fujishima and Kenichi Honda. Electrochemical photolysis of water at a semiconductor electrode. *Nature*, 238:37–38, April 1972.

[31] Xiaobo Chen and Samuel S. Mao. Titanium dioxide nanomaterials: Synthesis, properties, modifications, and applications. *Chem. Rev.*, 107:2891–2959, June 2007.

[32] Hengbo Yin, Yuji Wada, Takayuki Kitamura, Shingo Kambe, Sadao Murasawa, Hirotaro Mori, Takao Sakata, and Shozo Yanagida. Hydrothermal synthesis of nanosized anatase and rutile TiO_2 using amorphous phase TiO_2. *J. Mater. Chem.*, 11:1694–1703, 2001.

[33] V Petkov, G Holzhüter, U Tröge, Th Gerber, and B Himmel. Atomic-scale structure of amorphous TiO_2 by electron, x-ray diffraction and reverse monte carlo simulations. *Journal of Non-Crystalline Solids*, 231(1–2):17 – 30, 1998.

[34] Hengzhong Zhang and Jillian F. Banfield. Kinetics of crystallization and crystal growth of nanocrystalline anatase in nanometer-sized amorphous titania. *Chemistry of Materials*, 14(10):4145–4154, 2002.

[35] Vo Van Hoang. Structural properties of simulated liquid and amorphous TiO_2. *physica status solidi (b)*, 244(4):1280–1287, 2007.

[36] V. V. Hoang, H. Zung, and N. H.B. Trong. Structural properties of amorphous TiO_2 nanoparticles. *The European Physical Journal D*, 44:515–524, 2007.

[37] Hengzhong Zhang, Bin Chen, Jillian F. Banfield, and Glenn A. Waychunas. Atomic structure of nanometer-sized amorphous TiO_2. *Phys. Rev. B*, 78:214106, Dec 2008.

[38] Vo Van Hoang. The glass transition and thermodynammics of liquid and amorphous TiO_2 nanoparticles. *Nanotechnology*, 19(10):105706, 2008.

[39] Jian Zou, Jiacheng Gao, and Fengyu Xie. An amorphous TiO_2 sol sensitized with H_2O_2 with the enhancement of photocatalytic activity. *Journal of Alloys and Compounds*, 497(1–2):420 – 427, 2010.

[40] C Randorn, J. T. S. Irvine, and P. Robertson. Synthesis of visible-light-activated yellow amorphous TiO_2 photocatalyst. *Int. J. Photoenergy*, page 426872, 2008.

[41] Miki Kanna, Sumpun Wongnawa, Supat Buddee, Ketsarin Dilokkhunakul, and Peerathat Pinpithak. Amorphous titanium dioxide: a recyclable dye remover for water treatment. *Journal of Sol-Gel Science and Technology*, 53:162–170, 2010.

[42] Hu Young Jeong, Jeong Yong Lee, and Sung-Yool Choi. Interface-engineered amorphous TiO_2-based resistive memory devices. *Advanced Functional Materials*, 20(22):3912–3917, 2010.

[43] G.A. Battiston, R. Gerbasi, A. Gregori, M. Porchia, S. Cattarin, and G.A. Rizzi. Pecvd of amorphous TiO_2 thin films: effect of growth temperature and plasma gas composition. *Thin Solid Films*, 371(1–2):126 – 131, 2000.

[44] Zhiwei Zhao, Beng Kang Tay, and Guoqing Yu. Room-temperature deposition of amorphous titanium dioxide thin film with high refractive index by a filtered cathodic vacuum arc technique. *Appl. Opt.*, 43(6):1281–1285, Feb 2004.

[45] G. Kresse and J. Furthmller. Efficiency of ab-initio total energy calculations for metals and semiconductors using a plane-wave basis set. *Computational Materials Science*, 6(1):15 – 50, 1996.

[46] G. Kresse and J. Furthmüller. Efficient iterative schemes for *ab initio* total-energy calculations using a plane-wave basis set. *Phys. Rev. B*, 54:11169–11186, Oct 1996.

[47] G. Kresse and J. Hafner. *Ab initio* molecular dynamics for liquid metals. *Phys. Rev. B*, 47:558–561, Jan 1993.

[48] David Vanderbilt. Soft self-consistent pseudopotentials in a generalized eigenvalue formalism. *Phys. Rev. B*, 41:7892–7895, Apr 1990.

[49] John P. Perdew, Kieron Burke, and Yue Wang. Generalized gradient approximation for the exchange-correlation hole of a many-electron system. *Phys. Rev. B*, 54:16533–16539, Dec 1996.

[50] B. Prasai, B. Cai, M.K. Underwood, J.P. Lewis, and D.A. Drabold. Ab initio calculation of structural and electrical properties of amorphous TiO_2. *Mat. Sc. and Tech. Conf. Proceedings*, pages 12–20, 2011.

[51] D. A. Drabold. Topics in the theory of amorphous materials. *The European Physical Journal B*, 68:1–21, 2009.

[52] Crc handbook of chemistry and physics. *77th ed., edited by David R. Lide*, 1997.

[53] Hendrik J. Monkhorst and James D. Pack. Special points for brillouin-zone integrations. *Phys. Rev. B*, 1354:5188–519216533–16539, JunDec 1979.

[54] Raphael Shirley, Markus Kraft, and Oliver R. Inderwildi. Electronic and optical properties of aluminium-doped anatase and rutile TiO_2 from *ab initio* calculations. *Phys. Rev. B*, 81:075111, Feb 2010.

[55] Mazharul M. Islam, Thomas Bredow, and Andrea Gerson. Electronic properties of oxygen-deficient and aluminum-doped rutile TiO_2 from first principles. *Phys. Rev. B*, 76:045217, Jul 2007.

[56] Adil Fahmi, Christian Minot, Bernard Silvi, and Mauro Causá. Theoretical analysis of the structures of titanium dioxide crystals. *Phys. Rev. B*, 47:11717–11724, May 1993.

[57] D.T. Cromer and K. Herrington. The structures of anatase and rutile. *J. Am. Chem. Soc.*, 77:4708–4709, 1955.

[58] C.J. Howard, T. M. Sabine, and F. Dickson. Structural and thermal parameters for rutile and anatase. *Acta Cryst.*, 47:462–468, 1992.

[59] Shang-Di Mo and W. Y. Ching. Electronic and optical properties of three phases of titanium dioxide: Rutile, anatase, and brookite. *Phys. Rev. B*, 51:13023–13032, May 1995.

[60] A. Amtout and R. Leonelli. Optical properties of rutile near its fundamental band gap. *Phys. Rev. B*, 51:6842–6851, Mar 1995.

[61] H. Tang, H. Berger, P.E. Schmid, F. Lvy, and G. Burri. Photoluminescence in TiO_2 anatase single crystals. *Solid State Communications*, 87(9):847 – 850, 1993.

[62] S. Valencia, J. M. Marín, and G. Restrepo. Study of the bandgap of synthesized titanium dioxide nanoparticles using the sol-gel method and a hydrothemral treatment. *Open Mat. Sc. J.*, 4:9–14, 2010.

[63] Raymond Atta-Fynn, Parthapratim Biswas, Pablo Ordejon, and D. A. Drabold. Systematic study of electron localization in an amorphous semiconductor. *Phys. Rev. B*, 69:085207, Feb 2004.

[64] B. Cai and D. A. Drabold. Properties of amorphous gan from first-principles simulations. *Phys. Rev. B*, 84:075216, Aug 2011.

[65] M.L. Cohen and J.R. Chelikowsky. Electronic structure and optical properties of semiconductors. *2nd ed., edited by M.Cardona*, 1989.

[66] D. Weaire. Existence of a gap in the electronic density of states of a tetrahedrally bonded solid of arbitrary structure. *Phys. Rev. Lett.*, 26:1541–1543, Jun 1971.

[67] I. Chaudhuri, F. Inam, and D. A. Drabold. *Ab initio* determination of ion traps and the dynamics of silver in silver-doped chalcogenide glass. *Phys. Rev. B*, 79:100201, Mar 2009.

[68] J.M. Merino, S. Diaz-Moreno, G. Subias, and M. Leon. A comparative study of *CuSe* and *InSe* bond length distributions in $CuInSe_2$ with related in-rich compounds. *Thin Solid Films*, 480–481(0):295 – 300, 2005.

[69] M. Mitkova, Yu Wang, and P. Boolchand. Dual chemical role of *Ag* as an additive in chalcogenide glasses. *Phys. Rev. Lett.*, 83:3848–3851, Nov 1999.

[70] A. Piarristeguy, M. Fontana, and B. Arcondo. Structural considerations about the $(Ge_{0.25}Se_{0.75})_{100-x}Ag_x$ glasses. *Journal of Non-Crystalline Solids*, 332(1–3):1 – 10, 2003.

[71] Mark Cobb, D. A. Drabold, and R. L. Cappelletti. *Ab-initio* molecular-dynamics study of the structural, vibrational, and electronic properties of glassy $GeSe_2$. *Phys. Rev. B*, 54:12162–12171, Nov 1996.

[72] S. I. Simdyankin, S. R. Elliott, Z. Hajnal, T. A. Niehaus, and Th. Frauenheim. Simulation of physical properties of the chalcogenide glass As_2S_3 using a density-functional-based tight-binding method. *Phys. Rev. B*, 69:144202, Apr 2004.

[73] M. Aniya and F. Shimojo. Atomic structure and bonding properties in amorphous $Cu_x(As_2S_3)_{1-x}$ by *ab-initio* molecular-dynamics simulations. *Journal of Non-Crystalline Solids*, 352(9–20):1510 – 1513, 2006.

[74] B. Arcondo, M.A. Urena, A. Piarristeguy, A. Pradel, and M. Fontana. Homogeneous–inhomogeneous models of $Ag_x(Ge_{0.25}Se_{0.75})_{100-x}$ bulk glasses. *Physica B: Condensed Matter*, 389(1):77 – 82, 2007.

[75] A.S. Kraemer and G.G. Naumis. Use of the cage formation probability for obtaining approximate phase diagrams. *J. Chem. Phys.*, 128:134516, 2008.

[76] A. Lindsay Greer and Neil Mathur. Materials science: Changing face of the chameleon. *Nature*, 437:1246–1247, 2005.

[77] R. E. Simpson, M. Krbal, P. Fons, A. Kolobov, J. Tominaga, T. Uruga, and H. Tanida. Toward the ultimate limit of phase change in $Ge_2Sb_2Te_5$. *Nano letters*, 10:414–419, 2010.

[78] P. Fons. in phase change materials, science and application. *edited by S. Raoux and M. Wuttig*, page 154, 2009.

[79] Stanford R. Ovshinsky. Reversible electrical switching phenomena in disordered structures. *Phys. Rev. Lett.*, 21:1450–1453, Nov 1968.

[80] Noboru Yamada and Toshiyuki Matsunaga. Structure of laser-crystallized $Ge_2Sb_{2+x}Te_5$ sputtered thin films for use in optical memory. *J. Appl. Phys.*, 88:7020, 2000.

[81] Alexander V. Kolobov, Paul Fons, Anatoly I. Frenkel, Alexei L. Ankudinov, Junji Tominaga, and Tomoya Uruga. Understanding the phase-change mechanism of rewritable optical media. *Nat Mater*, 3:703–708, 2004.

[82] D. A. Baker, M. A. Paesler, G. Lucovsky, and P. C. Taylor. Exafs study of amorphous $Ge_2Sb_2Te_5$. *Journal of Non-crystalline Solids*, 352:1621–1623, 2006.

[83] Shinji Kohara, Kenichi Kato, Shigeru Kimura, Hitoshi Tanaka, Takeshi Usuki, Kentaro Suzuya, Hiroshi Tanaka, Yutaka Moritomo, Toshiyuki Matsunaga, Noboru Yamada, Yoshihito Tanaka, Hiroyoshi Suematsu, and Masaki Takata. Structural basis for the fast phase change of $Ge_2Sb_2Te_5$: Ring statistics analogy between the crystal and amorphous states. *Appl. Phys. Lett.*, 89:201901, 2006.

[84] P. Jovari, I. Kaban, J. Steiner, B. Beuneu, A. Schops, and M. A. Webb. Local order in amorphous $Ge_2Sb_2Te_5$ and $Ge_1Sb_2Te_4$. *Phys. Rev. B*, 77:035202, Jan 2008.

[85] J. Akola and R. O. Jones. Structural phase transitions on the nanoscale: The crucial pattern in the phase-change materials $Ge_2Sb_2Te_5$ and *GeTe*. *Phys. Rev. B*, 76:235201, Dec 2007.

[86] J Hegedus and S. R. Elliott. Microscopic origin of the fast crystallization ability of *Ge-Sb-Te* phase-change memory materials. *Nat Mater*, 7:399–405, 2008.

[87] B. Cai, D. A. Drabold, and S. R. Elliott. Structural fingerprints of electronic change in the phase-change-material: $Ge_2Sb_2Te_5$. *Appl. Phys. Lett.*, 97, 2010.

[88] T. Siegrist, P. Jost, H. Volker, M. Woda1, P. Merkelbach, C. Schlockermann, and M. Wuttig. Disorder-induced localization in crystalline phase-change materials. *Nature Mater.*, 10:202–208, 2011.

[89] P. E. Blöchl. Projector augmented-wave method. *Phys. Rev. B*, 50:17953–17979, Dec 1994.

[90] G. Kresse and D. Joubert. From ultrasoft pseudopotentials to the projector augmented-wave method. *Phys. Rev. B*, 59:1758–1775, Jan 1999.

[91] G. Kresse and D. Joubert. From ultrasoft pseudopotentials to the projector augmented-wave method. *Phys. Rev. B*, 59:1758–1775, Jan 1999.

[92] J. Akola and R. O. Jones. Density functional study of amorphous, liquid and crystalline $Ge_2Sb_2Te_5$: homopolar bonds and/or *AB* alternation? *J. Phys.: Condens. Matter*, 20:465103, 2008.

[93] Jean-Yves Raty, C. Otjacques, Jean-Pierre Gaspard, and Christophe Bichara. Amorphous structure and electronic properties of the $Ge_1Sb_2Te_4$ phase change material. *Solid State Sciences*, 12(2):193 – 198, 2010.

[94] S. Caravati, M. Bernasconi, T. D. Khne, M. Krack, and M. Parrinello. Coexistence of tetrahedral- and octahedral-like sites in amorphous phase change materials. *Appl. Phys. Lett.*, 91:171906, 2007.

[95] Kostiantyn Shportko, Stephan Kremers, Michael Woda, Dominic Lencer, John Robertson, and Matthias Wuttig. Resonant bonding in crystalline phase-change materials. *Nature Materials*, 7:653–658, 2008.

[96] T. H. Lee and S. R. Elliott. *Ab-Initio* computer simulation of the early stages of crystallization: Application to $Ge_2Sb_2Te_5$ phase-change materials. *Phys. Rev. Lett.*, 107:145702, Sep 2011.

[97] M Stuchlik, P. Krecmer, and S.R. Elliott. Opto-mechanical effect in chalcogenide glasses. *J OPTOELECTRON ADV M*, 3:361–366, 2001.

[98] Xilin Zhou, Liangcai Wu, Zhitang Song, Feng Rao, Min Zhu, Cheng Peng, Dongning Yao, Sannian Song, Bo Liu, and Songlin Feng. Carbon-doped $Ge_2Sb_2Te_5$ phase change material: A candidate for high-density phase change memory application. *App. Phys. Lett.*, 101:142104, 2012.

[99] Yu-Jen Huang, Yen-Chou Chen, and Tsung-Eong Hsieh. Phase transition behaviors of mo- and nitrogen-doped $Ge_2Sb_2Te_5$ thin films investigated by in situ electrical measurements. *J. Appl. Phys.*, 106:034916, 2009.

[100] Guoxiang Wang, Qiuhua Nie, Xiang Shen, R. P. Wang, Liangcai Wu, Jing Fu, Tiefeng Xu, and Shixun Dai. Phase change behaviors of zn-doped $Ge_2Sb_2Te_5$ films. *App. Phys. Lett.*, 101:051906, 2012.

[101] Ki-Ho Song, Sung-Won Kim, Jae-Hee Seo, and Hyun-Yong Lee. Characteristics of amorphous $Ag_{0.1}(Ge_2Sb_2Te_5)_{0.9}$0.9 thin film and its ultrafast crystallization. *J. Appl. Phys.*, 104:103516, 2008.

[102] K. Wang, D. Wamwangi, S. Ziegler, C. Steimer, M. J. Kang, S. Y. Choi, and M. Wuttig. Influence of sn doping upon the phase change characteristics of $Ge_2Sb_2Te_5$. *Phys. Status Solidi A*, 201:3087–3095, 2004.

[103] K. Wang, D. Wamwangi, S. Ziegler, C. Steimer, and M. Wuttig. Influence of bi doping upon the phase change characteristics of $Ge_2Sb_2Te_5$. *J. Appl. Phys.*, 96:5557, 2004.

[104] Eunae Cho, Yong Youn, and Seungwu Han. Enhanced amorphous stability of carbon-doped $Ge_2Sb_2Te_5$: *Ab Initio* investigation. *Appl. Phys. Lett.*, 99:183501, 2011.

[105] Eunae Cho, Seungwu Han, Hideki Kim, Dohyung Horii, and Ho-Seok Nam. Ab initio study on influence of dopants on crystalline and amorphous $Ge_2Sb_2Te_5$. *J. Appl. Phys.*, 109:043705, 2011.

[106] S. Caravati, D. Colleoni, R. Mazzarello, T. D. Khne, M. Krack, M. Bernasconi, and M. Parrinello. First-principles study of nitrogen doping in cubic and amorphous $Ge_2Sb_2Te_5$. *J. Phys.: Condens. Matter*, 23:265801, 2011.

[107] S Caravati, M. Bernasconi, T. D. Khne, M. Krack, and M. Parrinello. First-principles study of crystalline and amorphous $Ge_2Sb_2Te_5$ and the effects of stoichiometric defects. *J. Phys. Condens. Matter, 255501 (2009).*, 21, 2009.

[108] Jeffrey R. Errington and Pablo G. Debenedetti. Relationship between structural order and the anomalies of liquid water. *Nature*, 409:318, 2001.

[109] J. M. Skelton, T. H. Lee, and S. R. Elliott. Structural, dynamical, and electronic properties of transition metal-doped ge2sb2te5 phase-change materials simulated by *ab initio* molecular dynamics. *Appl. Phys. Lett.*, 101:024106, 2012.

[110] W. J. Wang, L. P. Shi, R Zhao, K. G. Lim, H. K. Lee, T. C. Chong, and Y. H. Wu. Fast phase transitions induced by picosecond electrical pulses on phase change memory cells. *App. Phys. Lett.*, 93:043121, 2008.

[111] T. C. Chong, L. P. Shi, R. Zhao, Tan P. K., J. M. Li, H. K. Lee, X. S. Miao, A. Y. Du, and C. H. Tung. Phase change random access memory cell with superlattice-like structure. *App. Phys. Lett.*, 88:122114, 2006.

[112] J. M. Skelton and S. R. Elliott. *In silico* optimisation of phase-change materials for digital memories: a survey of first-row transition-metal dopants for $Ge_2Sb_2Te_5$. *J. Phys. Condens. Matter*, 25:205801, 2013.

[113] W. Tang, E. Sanville, and G. Henkelman. A grid-based bader analysis algorithm without lattice bias. *J. Phys. Condens. Matter*, 21:084204, 2009.

[114] E. Sanville, S. D. Kenny, R. Smith, and G. Henkelman. An improved grid-based algorithm for bader charge allocation. *J. Comp. Chem.*, 28:899–908, 2007.

[115] G. Henkelman, A. Arnaldsson, and H. Jonsson. A fast and robust algorithm for bader decomposition of charge density. *Comput. Mater. Sci.*, 36:254–360, 2006.

[116] A. Seidl, A. Gorling, P. Vogl, J. A. Majewski, and M. Levy. Generalized kohn-sham schemes and the band-gap problem. *Phy. Rev. B.*, 53:3764–74, 1996.

Thesis and Dissertation Services